

## LIBRARY Michigan State University

This is to certify that the dissertation entitled

## TRANSITION RATES BEYOND <sup>48</sup>Ca: EFFECTIVE CHARGE IN THE *pf* SHELL

presented by

JONATHAN MICHAEL COOK

has been accepted towards fulfillment of the requirements for the

Ph.D.	degree inPhysics and Astronomy	
	T. / Imale	
	Major Professor's Signature	
	01/08/2009	
	Date	

MSU is an Affirmative Action/Equal Opportunity Employer

## **PLACE IN RETURN BOX** to remove this checkout from your record. **TO AVOID FINES** return on or before date due. **MAY BE RECALLED** with earlier due date if requested.

DATE DUE	DATE DUE	DATE DUE
·		

5/08 K:/Proj/Acc&Pres/CIRC/DateDue.indd

## TRANSITION RATES BEYOND $^{48}$ Ca: EFFECTIVE CHARGE IN THE pf SHELL

Ву

Jonathan Michael Cook

#### A DISSERTATION

Submitted to
Michigan State University
in partial fulfillment of the requirements
for the degree of

### DOCTOR OF PHILOSOPHY

Physics and Astronomy

2009

#### **ABSTRACT**

## TRANSITION RATES BEYOND <sup>48</sup>Ca: EFFECTIVE CHARGE IN THE *pf* SHELL

#### $\mathbf{B}\mathbf{y}$

#### Jonathan Michael Cook

The well-known magic numbers of stable nuclei can vanish and new ones appear in the neutron-rich nuclei far from stability. The GXPF1 effective interaction predicts the appearance of an N=32 subshell gap and an N=34 shell closure in Ti and Ca. The investigation of these shell gaps developed into a question of the appropriate effective charge in the pf shell. The trend of the measured transition matrix elements in the neutron-rich Ti isotopes is reproduced with effective charges derived from an analysis of isospin analogue states in  $^{51}$ Fe and  $^{51}$ Mn,  $e_p \approx 1.15$  and  $e_n \approx 0.8$ , that differ from the standard effective charges,  $e_p = 1.5$  and  $e_n = 0.5$ . The proton and neutron effective charges are mixed in the case of Ti, and to separate the two components the neutron effective charge is determined via the intermediate-energy Coulomb excitation of  $^{50}$ Ca. To reduce the uncertainty in the measurement a model is developed to simulate in-beam response functions for a position sensitive NaI(Tl)  $\gamma$ -ray detector. The effective charge is found to be  $e_n = 0.77(13)$ , indicating that the enhanced neutron effective charge derived in the upper pf shell is applicable in the lower pf shell.

#### ACKNOWLEDGMENT

I would like to express my thanks to my advisor, Thomas Glasmacher, and to Alexandra Gade for the large amount of time she spent guiding me during the creation of this dissertation. I entered graduate school with a great group of guys in my class: Matthew Amthor, Ivan Brida, Andy Rogers, Terrence Strother, and Wes Hitt. I have gained much from knowing my research group and others: Ania Kwiatkowski, Przemek Adrich, Matt Bowen, Chris Campbell, Christian Diget, Cristian Dinca, Andrew Ratkiewicz, Kyle Siwek, Russ Terry, Dirk Weisshaar, Heather Zwahlen. Finally, this dissertation was made possible by the outstanding staff of the National Superconducting Cyclotron Laboratory.

## TABLE OF CONTENTS

	List	of Tables	i
	List	of Figures vi	i
1	Intr	oduction	1
2	The	nuclear shell model and transition strength measurements.	5
	2.1	The beginnings	5
	2.2	The nuclear landscape	6
	2.3	The nuclear shell model	8
			8
		2.3.2 Effective interactions	O
		2.3.3 Effective charge	2
		2.3.4 The <i>pf</i> shell	7
	2.4	Transition-rate measurement techniques	1
		2.4.1 Transition rates	1
		2.4.2 Intermediate-energy Coulomb excitation	6
		2.4.3 The accuracy of intermediate-energy Coulomb excitation ex-	
		periments	3
3	Ext	erimental apparatus	2
	3.1	Isotope production	2
	3.2	The S800 Particle Spectrograph and the APEX NaI(Tl) Scintillator	
		Array	4
		3.2.1 The S800 Particle Spectrograph	5
	3.3	The APEX NaI(Tl) Scintillator Array	7
		3.3.1 The detector	7
		3.3.2 Electronics	2
		3.3.3 Calibrations	5
		3.3.4 Efficiency	6
4	Sim	ulation	1
	4.1	Detector Geometry	
	4.2	$\gamma$ -ray generator	2
	4.3	Interaction physics	
	4.4	Detector and electronics modeling 6	

5	Dat	a analysis and experimental results	69
	5.1	<sup>52</sup> Ti $B(E2; 0_1^+ \rightarrow \hat{2}_1^+)$ measurement	70
		5.1.1 Particle identification	71
		5.1.2 $\gamma$ -ray spectrum	75
		5.1.3 Cross section	79
		5.1.4 In-beam efficiency	82
	5.2		84
		5.2.1 Particle identification	84
		5.2.2 Cross section and $B(E2; 0_1^+ \rightarrow 2_1^+)$	85
	5.3	Effective charge in the pf shell	89
	5.4	Conclusion	91
A	Sim	ulated response functions of APEX	93
	A.1	GEANT4	93
		A.1.1 Input files	93
		A.1.2 Detector construction	
		A.1.3 $\gamma$ -ray generator	
		A.1.4 Angular distribution	
		A.1.5 Event action	
		A.1.6 Double-sided scintillator model	
	Bib	liography	155

## LIST OF TABLES

2.1	The properties of <sup>50</sup> Ca	20
2.2	The dominant $\gamma$ -ray multipolarities for a $ J_i - J_f $ transition with parity change $\Delta \pi$	23
3.1	The resolution of APEX compared to that typical of a 3"x3" NaI(Tl) crystal	43
5.1	The cross section and $B(E2; 0_1^+ \rightarrow 2_1^+)$ of <sup>52</sup> Ti used to determine the in-beam efficiency of APEX	84
5.2	The measured <sup>50</sup> Ca cross section leading to the final transition rate value.	88

## LIST OF FIGURES

1.1	The measured energy levels of neutron-rich Ti isotopes compared to shell-model calculations	3
1.2	The measured transition strengths of neutron-rich Ti isotopes compared to shell-model calculations with the standard and suggested effective charges	4
2.1	The Chart of the Nuclides	7
2.2	Diagram of the energy levels of the shell model	11
2.3	The spin arrangement of the $T_z = 0$ and $T_z = 1$ two-nucleon states.	15
2.4	The systematics of the first excited states in even-even, neutron-rich pf-shell nuclei	18
2.5	Experimental $B(E2; 0_1^+ \to 2_1^+)$ transition rates for neutron-rich Ti isotopes compared to shell-model calculations with the standard and modified effective charges	19
2.6	The neutron effective charges derived from the Ca isotopes	21
2.7	Schematic of Coulomb excitation of a nucleus from an initial state $ i\rangle$ to a final bound state $ f\rangle$ and the ensuing $\gamma$ decay	25
2.8	Schematic of a projectile nucleus scattering in the electromagnetic field of an infinitely heavy target nucleus	27
2.9	The percent differences between adopted and measured $B(E2; 0_1^+ \rightarrow 2_1^+$ transition rates for published test cases in intermediate-energy Coulomb excitation measurements	
3.1	The Coupled Cyclotron Facility	33

3.2	The S800 Particle Spectrograph	37
3.3	The laboratory-frame energy of a 1 MeV $\gamma$ ray produced in a frame moving at $\beta=0.3.$	38
3.4	A photo of the APEX Array	39
3.5	The scintillation process	40
3.6	The energy spectrum of an $^{88}\mathrm{Y}$ $\gamma\text{-ray}$ source produced by APEX	42
3.7	A schematic of the APEX electronics	44
3.8	The fit of the 898 keV $\gamma$ -ray energy peak in one slice of detector 2 for the energy calibration	46
3.9	The position response of APEX for an $^{88}\mathrm{Y}$ $\gamma\text{-ray source.}$	48
3.10	A simulated position-energy matrix for a double-sided scintillator bar with a high-resolution signal input into the discriminator	49
3.11	A simulated position-energy matrix of a double-sided scintillator bar with a low-resolution signal input into the discriminator	50
4.1	The APEX detector geometry constructed in Geant4	53
4.2	An isotropic angular distribution (solid line) is compared to the $E2$ distribution produced by the Coulomb excitation of $^{52}{\rm Ti.}$	55
4.3	The simulated $\gamma$ -ray emission position along the beam line	56
4.4	A kinematic diagram of a $\gamma$ ray Compton scattering on an electron.	59
4.5	The idealized detector response to 2 MeV $\gamma$ rays	60
4.6	The relationship between the angle of incidence $\psi$ to the crystal surface and the angle of emission $\theta$ from the scintillation point	62
4.7	The position response of APEX for an $^{88}\mathrm{Y}$ $\gamma\text{-ray source.}$	65
4.8	The energy response of APEX for an $^{88}$ Y $\gamma$ -ray source	66
4.9	The Coulomb excitation energy spectrum of <sup>76</sup> Ge	67

4.10	The position response of the <sup>76</sup> Ge photopeak	68
5.1	The particle identification spectrum with $^{52}\mathrm{Ti}$ indicated	72
5.2	The correlation between the position at CRDC1 in the S800 focal plane and the time of flight	73
5.3	The correlation between the angle in the S800 focal plane and the time of flight	74
5.4	A histogram showing the dependence of the ion chamber on the dispersive position	75
5.5	The corrected particle identification spectrum with $^{52}\mathrm{Ti}$ indicated $% \left( 1\right) =\left( 1\right) \left( 1\right)$	76
5.6	The time spectrum of a single APEX PMT	78
5.7	The scattering angle of $^{52}$ Ti nuclei with the maximum and minimum scattering angles indicated	79
5.8	The $\gamma$ -ray energy spectrum for $^{52}{ m Ti.}$	80
5.9	Fit of the response function plus continuum background to the $^{52}{\rm Ti}$ $\gamma$ -ray spectrum	83
5.10	The particle identification spectrum with $^{50}\mathrm{Ca}$ indicated	85
5.11	The corrected particle identification spectrum with $^{50}\mathrm{Ca}$ indicated.	86
5.12	The lower-lying states of $^{50}$ Ca	88
5.13	The difference in the angular distribution of $^{50}\mathrm{Ca}$ from that of $^{52}\mathrm{Ti}$ .	89
5.14	The fit of the response function plus continuum to the $^{50}$ Ca $\gamma$ -ray energy spectrum	90
Imag	ges in this thesis/dissertation are presented in color.	

## Chapter 1

## Introduction

The well-investigated energy-level spacing of stable nuclei may be altered in exotic nuclei with the magic numbers of the stable isotopes disappearing and new magic numbers arising. The GXPF1 interaction was developed as a unified effective interaction for the pf shell, and a N=32 subshell gap and a N=34 shell closure were predicted to appear for neutron-rich Ti and Ca isotopes. The measurement of the energy levels of the neutron-rich Ti isotopes confirmed the N=32 subshell closure but did not find evidence for the N=34 shell closure. The energy-level measurement was used to refine the GXPF1 into the GXPF1A effective interaction. The measurement of the transition rates of the neutron-rich Ti isotopes provides additional evidence for the N=32 subshell closure but again a N=34 shell closure is not apparent. The GXPF1A interaction fails to reproduce the transition rate systematics with the standard effective charges. New effective charges for the pf shell were suggested from a measurement of transition rates in isospin analogue states in <sup>51</sup>Fe and <sup>51</sup>Mn. The suggested effective charges reproduce the trend of the transition rates but not the amplitudes. A measure of the effective charge for nucleons in similar orbits to those of the neutron-rich Ti isotopes is proposed.

The GXPF1 interaction was developed for shell-model calculations in the full

 $\it pf$  shell, which permits the investigation of excitations across the N and Z=28shell gap[1]. By fitting the model parameters to emperical binding energies and energy levels, calculations with the GXPF1 interaction reproduces experimental excitation energies of the first excitated states  $E(2_1^+)$  in the Ca and Ti and predicted an N=32 subshell gap and an N=34 shell closure. The energy gap arises from an attractive proton-neutron interaction, with the  $\nu f_{5/2}$  orbit increasing in energy as the occupation of the  $\pi f_{7/2}$  orbit decreases to create a gap between the  $u p_{1/2}$  and the  $u f_{5/2}$  orbits. The experimental energy levels of the neutron-rich Ti isotopes measured via  $\beta$  decay and deep inelastic reactions [2, 3, 4, 5] are compared to shell-model calculations in Figure 1.1. The high  $E(2_1^+)$  at N=32, near that of the well-known N=28 magic number, indicates a subshell closure. The experimental  $E(2_1^+)$  for N=34 lies 300 keV lower than the energy calculated with the GXPF1 interaction. The GXPF1 interaction was developed using data from mostly stable nuclei, and the energy levels of the neutron-rich Ti isotopes were included to develop a modified effective interaction referred to as GXPF1A[6] that places the  $E(2_1^+)$  within 23 keV of the measured value. The difference between the two interactions lies primarily in the  $p_{1/2}$  and  $f_{5/2}$  matrix elements. The  $E(2_1^+)$ of  $^{56}\mathrm{Ti}$  sits near those of the non-magic N=28,30 nuclei, and no evidence is provided for a shell closure at N=34. Additionally, a two-proton knockout reaction was used to find  $E(2_1^+) = 2562$  keV for  $^{52}$ Ca; the high excitation energy relative to the nearby non-magic nuclei,  $\approx 1$  MeV, suggests an N=32 subshell closure [7].

To further examine the predicted shell closures, the transition strengths of the neutron-rich Ti isotopes were measured (Figure 1.2a). The transition strength at N=32 approaches that of the magic N=28, confirming a subshell gap, and the transition strength at N=34 is sufficiently increased that no evidence is provided for a shell closure. The shell-model calculation using the standard effective charges,  $e_p=1.5$  and  $e_n=0.5$ , to parameterize the averaged effects

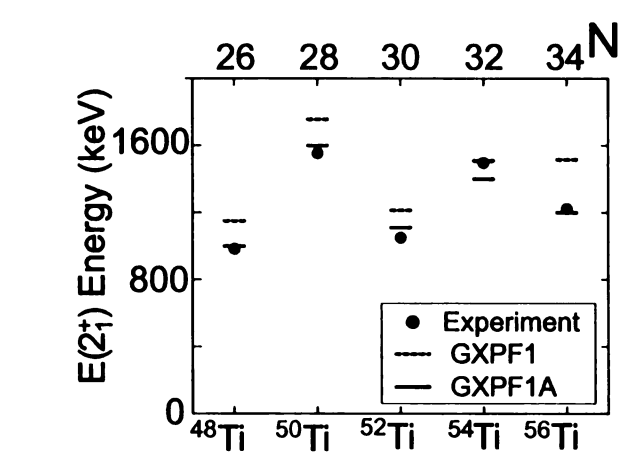


Figure 1.1: The measured energy levels of neutron-rich Ti isotopes compared to shell-model calculations with the GXPF1 and GXPF1A interactions.

of states outside of the truncated shell-model space fails to reproduce the data. Using the effective charges  $e_p \approx 1.15$  and  $e_n \approx 0.8$  derived in a study of  $T_z = \pm \frac{1}{2}$ , A = 51 states, the trend is reproduced although the amplitudes are not (Figure 1.2b). The structure in the calculated transition strengths is due to the enhanced neutron effective charge, suggesting that a measurement of the neutron effective charge would help to illuminate the underlying nuclear structure. The GXPF1A interaction utilizes a  $^{40}$ Ca core, and  $^{50}$ Ca is configured with 10 valence neutrons, two of which lie above the N = 28 shell gap. The goal of this thesis is the measurement of the transition strength of  $^{50}$ Ca to determine the neutron effective charge near the proposed N = 32,34 shell gaps.

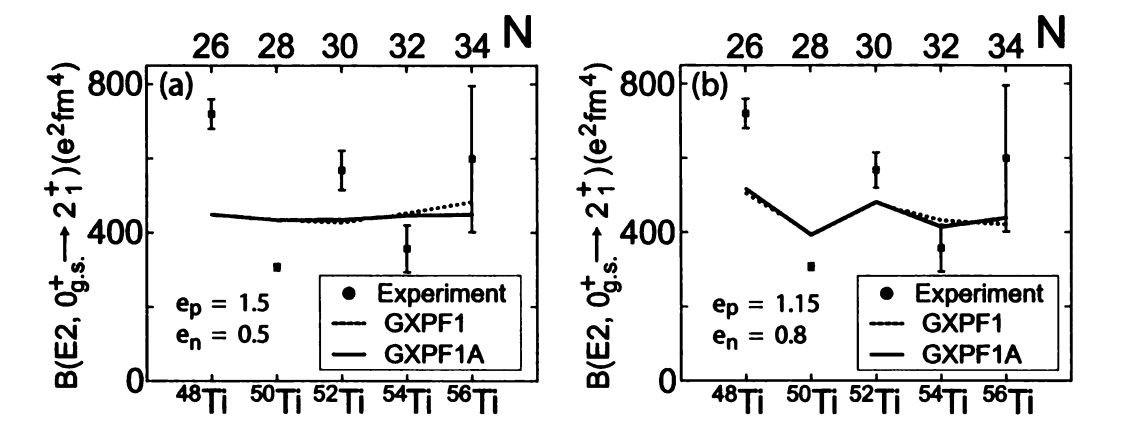


Figure 1.2: The measured transition strengths of neutron-rich Ti isotopes compared to shell-model calculations with (a) the standard effective charges,  $e_p = 1.0$  and  $e_n = 0.5$ , and (b) the suggested effective charges,  $e_p \approx 1.15$  and  $e_n \approx 0.8$ .

## Chapter 2

# The nuclear shell model and transition strength measurements

## 2.1 The beginnings

The field of nuclear physics was born with Henri Becquerel's discovery of radioactivity. Following work by Ernest Rutherford and Pierre and Marie Curie, James Chadwick discovered the neutron in 1932[8]. Now certain that the nucleus contained positively charged protons and chargeless neutrons, physicists began to probe the internal structure of the nucleus. Subsequent discoveries showed that the chemical properties of the nucleus depended on the number of protons, and the nucleus can contain varying number of neutrons to form isotopes. The protons and neutrons, collectively referred to as nucleons, were found to interact through three forces: the weak nuclear force, the strong nuclear force, and the Coulomb force. The weak nuclear force is the means by which neutrons become protons and vice versa. The strong nuclear force is produced by the short-range attractive potential of each nucleon. The Coulomb force causes a repulsion between protons. In contrast to the easily-studied and well-known Coulomb force, the strong nuclear

force, taking place on the femtometer scale of the nucleus, is not well understood. Theoretical models constructed to explain and to predict the interactions within the nucleus are broadly classified into two groups: collective and single-particle models.

Collective models picture the nucleus as a group of nucleons in concerted action. Vibrations in the shape of the nuclear matter effect energy levels characteristic of the harmonic oscillator, and rotation of a static deformation produces the energy levels of a rotor. Collective models have had great success examining the structure of the nucleus as a whole at the cost of losing sight of individual nucleons.

In contrast, single-particle models approach the nucleus as a group of individual nucleons. The interactions between the nucleons determines the attributes of the nucleus; for example, an excitation of the nucleus involves the movement of one or more nucleons from one specific configuration to another. The single-particle models elucidate the fundamental interactions governing the nucleus but become increasingly cumbersome as the number of nucleons increases. The advancement of single-particle models into heavier nuclei remains at the forefront of nuclear physics research as we continue to better understand the more exotic nuclei produced by continually improving facilities.

## 2.2 The nuclear landscape

In analogy to the chemical table of elements, the isotopes can be arranged to form the Chart of the Nuclides, shown in Figure 2.1. The nuclear neutron number N increases moving to the right of the chart, and the proton number Z increases moving upward. Each block on the chart is an isotope of mass number A = N + Z. The isotopes in black are stable—they do not spontaneously decay into another isotope. The stable isotopes form a "valley of stability," which follows N = Z for

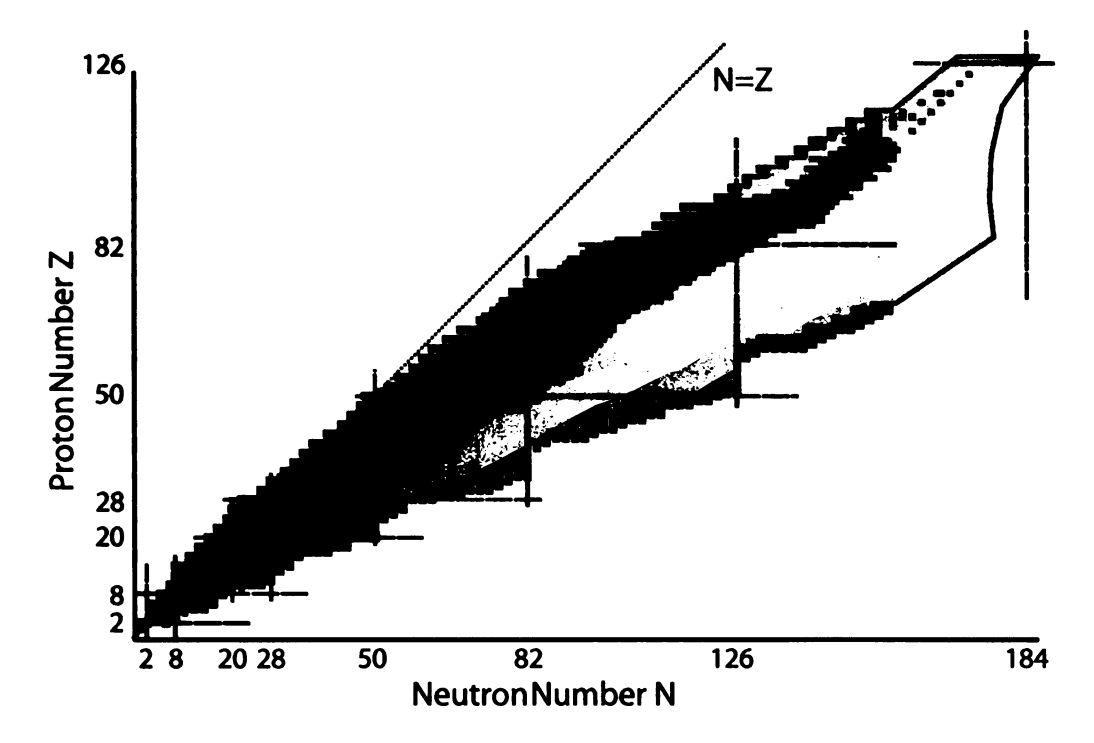


Figure 2.1: The Chart of the Nuclides with neutron number increasing to the right and proton number increasing towards the top. The stable nuclei are drawn in black, the known unstable nuclei in dark grey, and predicted nuclei in light grey. The magic numbers are indicated on the axes.

lighter isotopes and veers toward a neutron excess for higher mass nuclei. The known unstable nuclei are shown in dark grey and predicted nuclei in light grey. The unstable isotopes undergo spontaneous  $\beta$  decay or  $\alpha$  emission, transforming them into another isotope. The right edge of the nuclei shown in the chart is the neutron drip line—the point beyond which a neutron added to the nucleus will not form a bound system. Similarly, the proton drip line is found on the left edge.

Many systematic features of nuclei can be seen on this chart. The proton and neutron numbers labeled on the axes are called magic numbers. These magic numbers, 2, 8, 20, 28, 50, 82, and 126, correspond to particularly stable nuclear configurations as indicated by a high first excited state and a low probability of transition to that state. Several other physical observables indicate the existence of the magic numbers. Nuclear binding energies, for example, display major dis-

continuities at the magic numbers, as do neutron and proton separation energies,

The nuclear magic numbers are analogous to features found in the atom. In particular, the neutron and proton separation energies corresponds to the atomic ionization energy. The ionization energies have a discontinuity at the noble gases, Z=2, 10, 18, 36, 54, and 86 elements that are particularly stable and that for a long time were thought inert. The electron configurations of the noble gases have their electrons placed in closed shells, i.e. one configuration of electrons has been filled and the next electron must be added to a configuration with a different angular momentum or radius. Between the major shell closures with correspondingly major changes in properties there may be smaller subshells with smaller changes in properties, such as may be seen between the Group 2 and Group 3 elements. The recognition of the similarity between the nuclear and the atomic properties led to the development of a theoretical model of the nucleus inspired by shell structure.

## 2.3 The nuclear shell model

#### 2.3.1 Form of the shell model

The investigation of the shell-like effects of the nucleus culminated in the development of the nuclear shell model by Maria Goeppert-Mayer and J. Hans D. Jensen, for which they were awarded the 1963 Nobel Prize in Physics[9]. The shell model is a single-particle model consisting of a central potential  $V_c$  and a spin-orbit potential  $V_{l.s}$ . The natural appearance of shell structure can be seen even in the simple case of a square well potential with N, Z >> 1 non-interacting nucleons, where filling the square well according to Fermi statistics results in nucleons lying in successively higher energy levels. The last level filled in this Fermi gas model corresponds to an energy and momentum referred to as the Fermi surface. The

Fermi gas model, however, does not present a means of calculating wavefunctions that a more sophisticated model is capable of providing.

The shell model is based on the simplification that each nucleon moves in a potential that represents the sum effect of the interactions with the remaining A-1 nucleons. The strong nuclear force is known to have a short range, and the central potential is correspondingly expressed over a finite distance. Nonetheless, for computational simplicity the central potential is commonly represented as a harmonic oscillator potential, which despite extending to infinity is often sufficient. The harmonic oscillator potential is

$$V_c(r) = \frac{1}{2}m\omega^2 r^2 \tag{2.1}$$

where m is mass and  $\omega$  is chosen to reproduce the nuclear mean square radius,  $\hbar\omega\approx 40A^{-1/3}$  MeV. The harmonic oscillator potential has quantum numbers  $n_x$ ,  $n_y$ ,  $n_z$ , and  $m_s$  with energy levels lying at

$$n_{tot} = n_x + n_y + n_z (2.2)$$

$$E = (n + \frac{3}{2})\hbar\omega. \tag{2.3}$$

The  $m_s$  quantum number is the spin orientation of the nucleons, which are spin-1/2 fermions and can therefore take the values of  $\pm \frac{1}{2}$ . Employing the Pauli Exclusion Principle, which states that two identical fermions may not occupy the same quantum state simultaneously, it can be seen that the magic numbers of the harmonic oscillator occur at  $n_{tot} = 1$  with occupancy 2,  $n_{tot} = 2$  with total occupancy 8, and so on with shell closures at 20, 40, 70, and 112. While the initial nuclear magic numbers of the nucleus are reproduced, the higher lying ones are not.

Mayer's and Jensens' breakthrough was the realization that a strong spin-orbit

potential leads to the correct magic numbers. The spin-orbit potential  $V_{l\cdot s}$  represents the splitting of energy levels of total angular momentum  $\vec{j} = \vec{l} + \vec{s}$  and originates in the exchange of vector mesons[10]. The observed shell closings are obtained when the sign of the potential lowers the j = l + 1/2 levels. Altogether, the central potential takes the form

$$V(r) = V_c(r) - V_{ls}(r)l \cdot s. \tag{2.4}$$

This potential reproduces the nuclear magic numbers of the single-particle shell structure diagramed in Figure 2.2. The states are labeled using  $nl_j$  notation, with n as the radial quantum number that increments for each repetition of l. The spin-orbit potential can be seen in the splitting of the j degeneracy so that  $1p_{3/2}$  lies lower than the  $1p_{1/2}$  and in the formation of large energy gaps as occupancy reaches the magic numbers. The Pauli Exclusion Principle gives rise to a 2j+1 occupancy for each shell. The shells created between the magic number occupancies are termed the p shell for the  $1p_{3/2}$  and  $1p_{1/2}$  states, the sd shell for the  $1d_{5/2}$  through the  $1d_{3/2}$  states, and pf shell for the  $1f_{7/2}$  through the  $1f_{5/2}$  states.

#### 2.3.2 Effective interactions

The actual interaction between nucleons is considerably more complex than represented thus far. To approximate the true nuclear potential for a single nucleon, a Hamiltonian is formed from a mean potential and the two-body interaction. The mean potential is chosen such that the off-diagonal matrix elements of the Hamiltonian are minimized and provides a means of calculating the single-particle states. Diagonalizing the full Hamiltonian determines a basis in which the Hamiltonian is solved. The resulting basis states consist of mixtures of the single-particle states, a situation referred to as configuration mixing. In this manner, a large part of the

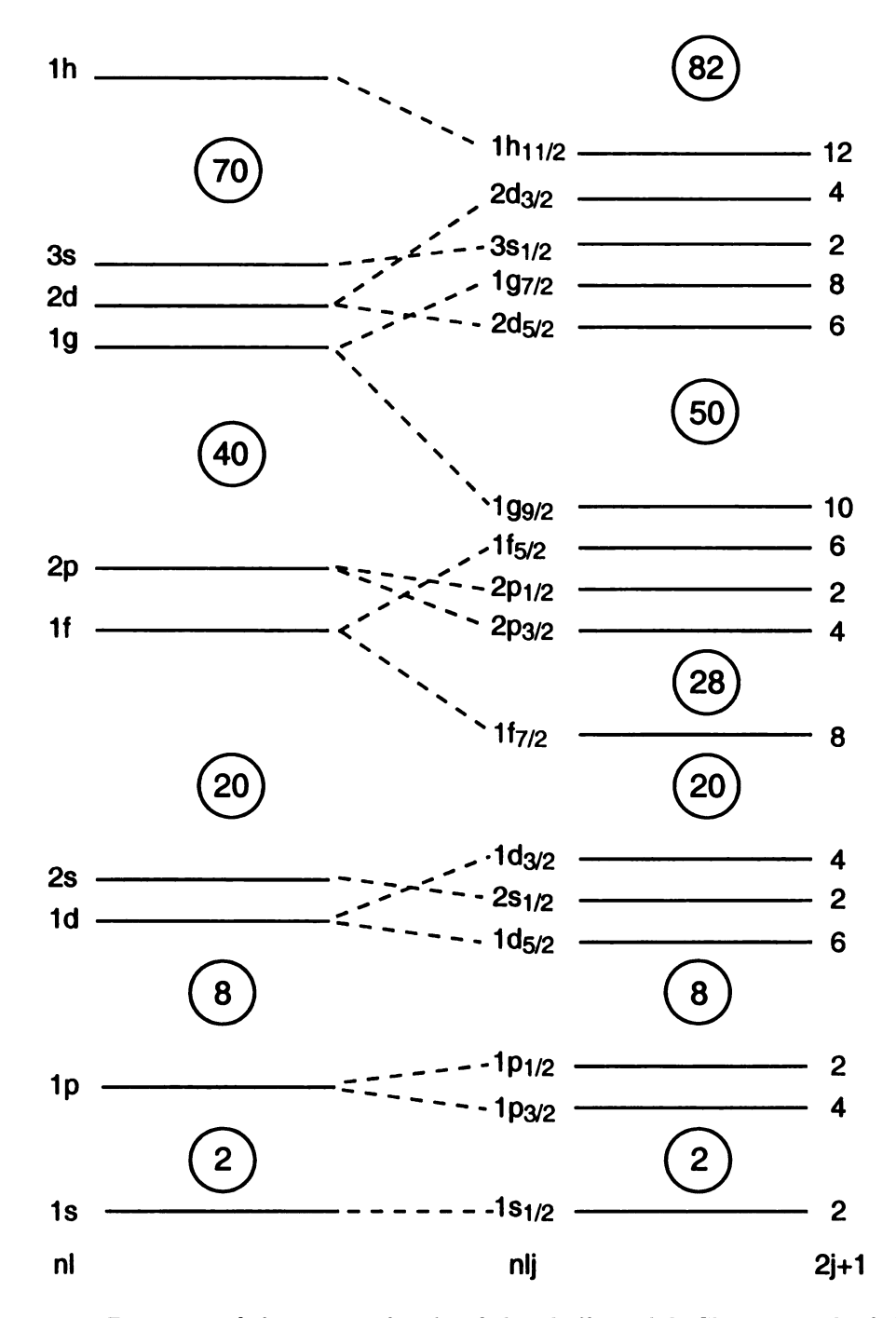


Figure 2.2: Diagram of the energy levels of the shell model. Shown on the left are the energy levels of an isotropic harmonic oscillator potential. On the right are the single-particle levels of the harmonic oscillator with a spin-orbit interaction. n is the radial quantum number that increases with the orbital angular momentum l.  $j = l \pm s$  is the total angular momentum, and each orbital can be occupied by a maximum of 2j + 1 neutrons or protons. Large shell gaps lead to the occurrence of magic numbers as indicated.

nucleon-nucleon interaction has been replaced by a mean field, and the residual interaction remaining may be reduced to the point that the infinite-dimensional Hamiltonian can be solved in a small subset of the original space. This procedure of determining the effective interaction in a shell-model subspace is referred to as renormalization.

There are natural subsets of states over which the Hamiltonian is renormalized. Since low-energy states are of interest, the excitation of only nucleons just below the Fermi surface is considered. These valence nucleons lie above a large number of states with very low likelihood of excitation, which can be considered an inert core. The states lying far above the Fermi surface have similarly very little contribution to the excitation and may be ignored. The full shell model has then been reduced to no more than a few states containing the valence nucleons and their low-lying excited states. A nearby doubly-magic nucleus is typically used for the core. With a chosen core and valence space, an effective interaction can be developed from fits to empirical data to include the averaged effects of the interaction between valence nucleons and nucleons outside of the model space. Two effective interactions accepted as standard are the Cohen-Kurath in the valence p shell and the USD in the valence sd shell[11, 12].

## 2.3.3 Effective charge

The Cohen-Kurath and USD interactions have had considerable success in modeling the features of relevant nuclei. Theory agrees satisfactorily with experiment on energy levels, beta-decay, and magnetic moments. In addition, the off-diagonal matrix elements reproduce the magnetic dipole transition rates, providing additional confirmation of the wavefunctions. However, the wavefunctions derived from the effective interactions fail to produce correct electric quadrupole transition rates. The failure can be seen clearly in the case of <sup>17</sup>O, which has a <sup>16</sup>O core with a

valence neutron excited into the  $2s_{1/2}$  state. The electric quadrupole operator is not expected to act strongly on a chargeless neutron, and the predicted lifetime for decay to the  $1d_{5/2}$  orbit is long. Empirically, the lifetime is quite short, as if the excited nucleon were a proton.

This discrepancy may be resolved by considering that when the valence neutron moves through the core it must disturb the inert core nucleons. The disturbance leads to a polarization of the core protons, which is the underlying mechanism causing the electric quadrupole transition of a neutron. The polarization of the core protons may be parameterized in the original scheme of a core plus a valence nucleon by adding an effective charge to the neutron,  $e_n = \delta_n$ , in units of elementary charge. Equivalently, valence protons carry an effective charge  $e_p = (1 + \delta_p)$ . The factors  $\delta_n$  and  $\delta_p$  are referred to as the polarization charges and, at first glance, are expected to be equal due to the charge independence of the strong force. In the effective charge scenario, level schemes, beta-decay, and magnetic moments (heavy nuclei may require an analogous effective q factor) are computed with the derived wavefunctions; electric quadrupole matrix elements are calculated with the addition of polarization charges. Since accurate wavefunctions are prerequisite to the derivation of the effective charge, the polarization charges were first determined from simple configurations, such as one or two nucleons outside of the  $^{16}\mathrm{O}$  core. Experimentally, it has been found that  $\delta_p = \delta_n = 0.5$  is adequate to reproduce electric quadrupole transition rates for these nuclei [13], and this value of polarization charge has come to be accepted as the standard value.

The electric quadrupole, or E2, transition rates are typically expressed in terms of the reduced transition rate B(E2). The  $B(E2; 0_1^+ \rightarrow 2_1^+)$  for an even-even nucleus is related to theory and effective charge by

$$B(E2; 0_1^+ \to 2_1^+) = (e_n A_n + e_p A_p)^2 \tag{2.5}$$

where  $A_n$  and  $A_p$  are the neutron and proton transition matrix elements. The scaling of the effective charge on the transition rate is apparent. The B(E2) is discussed further in Section 2.4.1.

In examining the mechanism underlying the initial assumption of the equivalence of the proton and neutron polarization charge, it is useful to introduce isospin. The formulation of isospin neglects the Coulomb force and treats the proton and neutron as a single type of particle, the nucleon. Isospin algebra is that of a spinor, and the nucleon has two states,

$$t_{zn} = +1/2 \tag{2.6}$$

$$t_{zp} = -1/2$$

where  $t_z$  is the z component of the isospin  $\vec{t}$ . A nucleus is then characterized by a total isospin and z component of

$$\vec{T} = \sum_{i=1}^{A} \vec{t_i}.$$

$$T_z = \frac{N-Z}{2}$$
(2.7)

For the simplest case of a two-nucleon interaction, the n-n system has the properties of  $T_z = +\frac{1}{2} + \frac{1}{2} = +1$  and T = 1. Similarly, for the p-p system  $T_z = -1$  and T = 1. The p-n system has the properties of  $T_z = 0$  and T = 1 or 0. The significance of the result can be visualized by considering the two-nucleon state with l = 0. As shown in Figure 2.3, the  $T_z = +1$  and  $T_z = -1$  states have antiparallel spin as required by the Pauli principle, and the T = 1 p-n state is similarly antisymmetric. Since the strong force is charge independent, all  $T_z = 1$  configurations have the same energy. The p-p and n-n states, and hence the antisymmetric p-n state, are unbound. In contrast, the symmetric  $T_z = 0$  state is the bound deuteron.

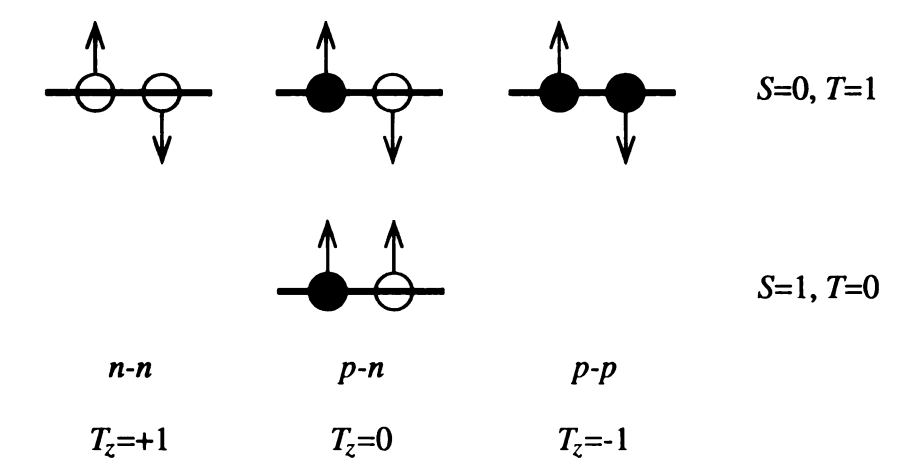


Figure 2.3: The spin arrangement of the  $T_z = 0$  and  $T_z = 1$  two-nucleon states. The  $T_z = 1$  isospin triplet states on the top are unbound. The antisymmetrized  $T_z = 0$  p-n singlet state is bound, signaling that a stronger interaction is possible for p-n than for n-n or p-p.

The conclusion is that a divergence in the polarization charges of the proton and neutron would lead to an enhancement of the neutron polarization charge relative to that of the proton.

The meaning of effective charge is illustrated by models where the effective charge is not required. In the case of  $^6\mathrm{Li}$ , a no-core shell model, in which all nucleons are active in a  $6\hbar\omega$  model space, was developed by Navrátil et~al.[14]. In this model, the E2 transition matrix elements can be calculated directly without resorting to effective charges. Since the full-space eigenvectors are known, a two-body E2 operator renormalized over a  $0\hbar\omega$  subspace can be calculated explicitly. Operating on the renormalized wavefunctions reproduces the full-space transition matrix elements. On the other hand, introducing effective charges of  $e_p=1.527$  and  $e_n=0.364$  to the full-space E2 operator acting on the truncated model space also replicates the full-space matrix elements. Therefore, the model-space truncation is capable of causing operator renormalization that is characterized by effective charges similar to the standard effective charges,  $e_p=1.5$  and  $e_n=0.5$ . The polarization of the core is due to a coupling of the valence nucleons with the giant

quadrupole resonance of the core protons. For the no-core shell model, the calculation of the full-space eigenvectors is unfortunately intractable for all but small A systems due to the rapidly increasing number of possible configurations in higher mass nuclei, a region where the parameterization of core polarization offered by effective charge allows calculations to be performed.

The giant quadrupole resonance arises in the collective model of the nucleus. Treating the nucleus as a harmonic oscillator, the quadrupole resonances take the form a  $\Delta n=2$  excitation, that is, excitations to  $E=2\hbar\omega$  states. The isoscalar component of the effective charge,  $e_{IS} = \frac{1}{2}(e_p + e_n)$ , is coupled to the isoscalar component of the resonance, a quadrupole-shaped oscillation of the nuclear matter. The isovector component of the effective charge,  $e_{IV} = \frac{1}{2}(e_n - e_p)$ , instead couples to a resonance of neutrons and protons moving with a phase shift of  $\pi$ . In the nocore shell model of <sup>6</sup>Li, the difference in the renormalization of the isoscalar and isovector parts of the operator results in the formation of neutron effective charge. The significance of the giant quadrupole resonance to the effective charge was studied by comparing a microscopic model of the excitations to the macroscopic, collective model [15]. The microscopic model is formed by explicitly adding  $\Delta n =$ 2 excited states to the shell-model space with a delta-function for the effective interaction. For  $^{42}\mathrm{Ca},$  the microscopic model calculates  $\delta_p=0.06(07)$  and  $\delta_n=0.06(07)$ 0.57(03). In contrast, the macroscopic model is found to be much more sensitive to the isovector component of the resonance, and polarization charges of  $e_p=0.19$ and  $e_n = 0.90$  are calculated.

As shown above, each core has a unique internal configuration and because each isotope has a unique arrangement of valence nucleons, and the polarization charges are not fixed across the entire nuclear landscape. Polarization charges of  $\delta_p = 0.2$  and  $\delta_n = 0.5$  were derived for the full sd shell[16] and e.g. were recently applied with success to transition rates in  $^{36,38}$ Si[17]. As mentioned in the following

section, polarization charges of  $e_p \approx 1.15$  and  $e_n \approx 0.80$  have been suggested for the pf shell.

## 2.3.4 The pf shell

The pursuit of unified effective interactions beyond the p and sd shells led to the development of the GXPF1A effective interaction for the pf shell[6]. The GXPF1A effective interaction was developed from the G matrix and was fit to 700 experimental energy levels in 87 mostly stable nuclei. The GXPF1A interaction was then used to predict energy levels and transition rates in exotic nuclei. Nuclei further away from the valley of stability are of particular interest since the well-known magic numbers of stable nuclei may grow less prominent or vanish and new shell gaps may appear[18]. The existence of shell gaps is of great importance because the placement and ordering of the orbitals is the root of the shell model.

The GXPF1A interaction successfully reproduces the energy levels of nuclei in the lower pf shell. The systematics of even-even nuclei are interesting due to their regular structure: a  $0^+$  ground state with a  $2^+$  first excited state using  $J^{\pi}$  notation. The systematics of the  $2_1^+$  state in neutron-rich Ca and Ti isotopes are plotted in Figure 2.4 and compared to the excitation energies calculated with three effective interactions, the GXPF1A, the older GXPF1, and the KB3G[19]. The high  $E(2_1^+)$  characteristic of a shell gap is clear at N=28, and a subshell closure is indicated at N=32.

In the investigation of the shell structure of pf-shell nuclei, the  $B(E2; 0_1^+ \to 2_1^+)$  of neutron-rich Ti isotopes were measured by Dinca  $et\ al.[20]$ . The  $B(E2; 0_1^+ \to 2_1^+)$  is sensitive to the overlap of the initial and final state wavefunctions rather than being an eigenvalue of the system. The characteristic low transition probability is seen at the magic N=28 in Figure 2.5a, and a similar rate is seen for the subshell closure at N=32 while the other isotopes are found to have transition

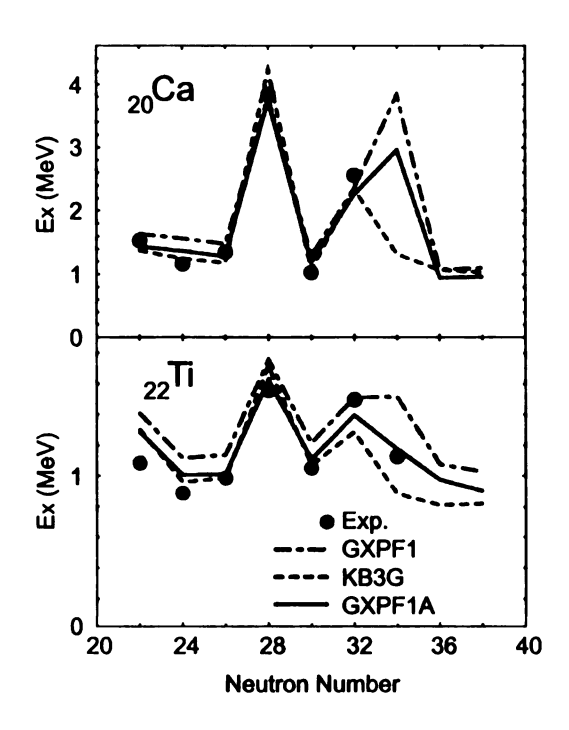


Figure 2.4: The systematics of the first excited states in even-even, neutron-rich pf-shell nuclei. The experimental results in dots is compared to the results of calculation with three effective interactions, the GXPF1 (dot-dashed), the KB3 (dashed), and the GXPF1A (solid). Figure from Reference [6].

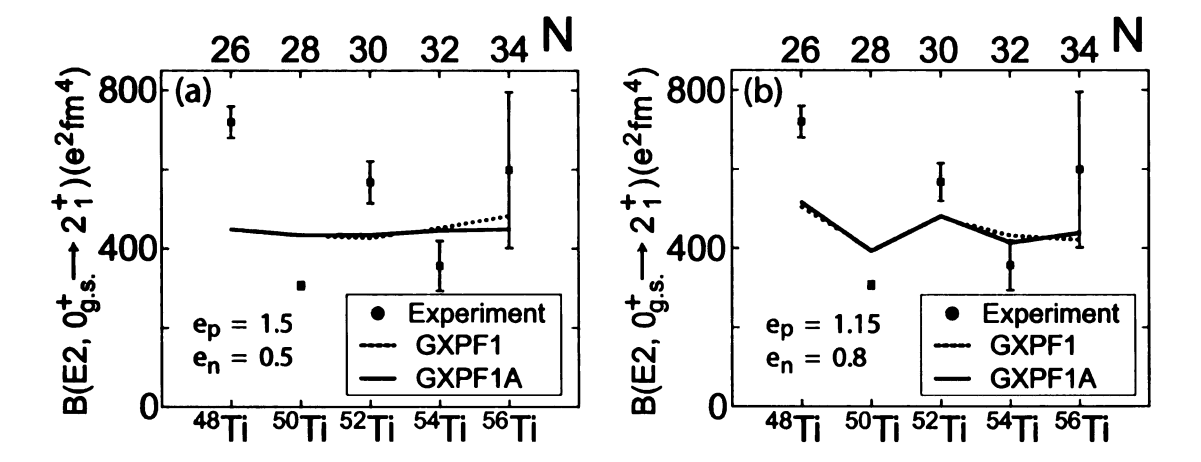


Figure 2.5: Experimental  $B(E2; 0_1^+ \to 2_1^+)$  transition rates for neutron-rich Ti isotopes compared to shell-model calculations using the GXPF1A interaction with (a) standard effective charges and (b) modified effective charges suggested by du Rietz *et al.*[21]. Figure from Dinca *et al.*[20].

rates roughly twice as high. Intriguingly, the transition rates calculated with the GXPF1A interaction do not reproduce the data. However, it is instructive to separate the contribution to the transition rate of active states, the theoretical transition amplitudes, and the effects from states outside of the active subspace, effective charge.

Effective charge has previously been studied in the upper pf shell by du Rietz et~al.[21]. By measuring the lifetime of analogue states in the  $T_z=\pm 1/2$  mirror nuclei  $^{51}$ Fe and  $^{51}$ Mn, it was possible to isolate the effective charge. When compared with shell-model calculations, the ideal effective charges were found to be  $e_n\approx 0.80$  and  $e_p\approx 1.15$ . Recall that an enhanced neutron effective charge is suggested by antisymmetry. The result of using these polarization charges to calculate transition rates in neutron-rich Ti isotopes is shown in Figure 2.5b. The trend of the transition rates is reproduced if the amplitudes are not.

Because of the infeasibility of calculating the interaction in the entire configuration space of a pf-shell nucleus, effective charge forms a key measure of the interaction of the valence nucleons with the core. The standard effective charges

$T_{1/2}$	13.9 (6)	s
$S_{n}^{'}$	6353 (9)	MeV
$S_{p}$	$1.228 \times 10^4$ (4)	MeV
$\dot{Q}_{eta^-}$	4966 (17)	MeV
$E(2_1^+)$	1026 (1)	keV

Table 2.1: The half-life, neutron separation energy, proton separation energy, Q value of  $\beta$  decay, and energy of the first  $2^+$  level of  $^{50}$ Ca. Data taken from Reference [22].

have been shown to be insufficient for both A=51,  $T_z=\pm 1/2$  mirror nuclei and the neutron-rich Ti isotopes. The effective charges deduced in the upper pf shell reproduce the trend but not the amplitude of transition rates measured in the lower pf shell. The question remains: what effective charges properly parameterize the core polarization in the pf shell?

The Ti isotopes discussed here have both proton and neutron valence nucleons; thus the individual contribution to the core polarization is disguised. An ideal measurement of effective charge would isolate the effective charge of the proton and neutron individually. Using a  $^{40}$ Ca core, the Ca isotopes are modeled with valence neutrons alone. The E2 transition is solely due to the polarization of the core protons by the valence neutrons and therefore provides a means of measuring the neutron effective charge alone. The neutron effective charge of N > 40 Ca isotopes derived using experimental  $B(E2; 0_1^+ \rightarrow 2_1^+)$  values and GXPF1A shell-model calculation are shown in Figure 2.6. The core polarization is enhanced near  $^{40}$ Ca as described in Reference [15] and decreases as the neutron number increases. However, all of the experiment data in the figure is from isotopes below the N=28 shell gap.  $^{50}$ Ca, with two neutrons in the  $2p_{3/2}$  orbit, is more similarly configured to the N=32,34 Ti isotopes where the shell closures have been predicted. It is for this reason that the E2 transition rate of  $^{50}$ Ca is presented here.

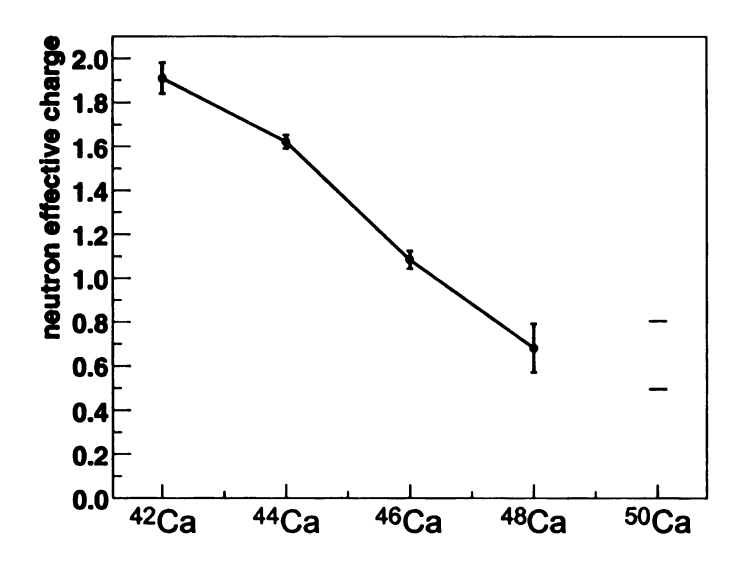


Figure 2.6: The neutron effective charge derived from the Ca isotopes' experimental transition strengths and amplitudes calculated with the GXPF1A interaction. For <sup>50</sup>Ca the standard effective charge and that suggested by du Rietz *et al.* are indicated with dashes. Data from References [23, 24]

## 2.4 Transition-rate measurement techniques

#### 2.4.1 Transition rates

Portions of the following section have been adopted from Reference [25], which was written by the author of this dissertation. Transition rates are typically expressed in terms of the reduced transition rate matrix element. The  $B(\sigma\lambda)$  of a general transition from state  $J_i$  to state  $J_f$  is defined as

$$B(\sigma\lambda; J_i \to J_f) = \frac{1}{2J_i + 1} |\langle J_f || \mathcal{M}_{\sigma\lambda} || J_i \rangle|^2$$
 (2.8)

where  $\sigma$  signifies either an electric or magnetic transition,  $\lambda$  is the orbital angular momentum of the transition, and  $J_{i,f}$  is the total angular momentum of the initial and final states. The matrix element on the right is a reduced matrix element, i.e. the Wigner-Eckart Theorem has been used to separate the  $M_s$  dependence, leaving

the matrix element dependent on J only. The magnetic substates are normally not observed separately, and the initial states have been averaged and the final states summed. The multipolarity of the emitted  $\gamma$  ray is determined by selection rules that follow from the conservation of angular momentum,

$$|J_i - J_f| \le \lambda \le J_i + J_f, \tag{2.9}$$

and from the conservation of parity,

$$\Delta \pi = \begin{cases} (-1)^{\lambda} & E_{\lambda} \text{ radiation} \\ (-1)^{\lambda+1} & M_{\lambda} \text{ radiation} \end{cases}$$
 (2.10)

For photons with wavelengths much greater than the nucleus (the nucleus is characterized by a length scale of  $\sim 10$  fm and the wavelength of a 1 MeV photon is  $\sim 10^3$  fm), the probability of a transition decreases rapidly with higher multipolarity. The lowest allowed multipolarities for  $\Delta J = |J_i - J_f|$  transitions, with the next highest allowed multipole in parenthesis to indicate that it is usually not significant, are listed in Table 2.2[26]. In this investigation of effective charge, the E2 excitation from the  $0_1^+$  ground state to the  $2_1^+$  first excited state in even-even nuclei is analyzed, and the quantity of interest is

$$B(E2; 0_1^+ \to 2_1^+) = |\langle 2_1^+ || Q_2 || 0_1^+ \rangle|^2$$
 (2.11)

with  $Q_2$  as the electric quadrupole operator. The lifetime of the state  $\tau$  is related to the reduced transition excitation rate by

$$\tau = \frac{4.081 \times 10^3}{E_x^5 B(E2; 0_1^+ \to 2_1^+)},\tag{2.12}$$

Parity change	Change of angular momentum $ J_i - J_f $				
$\Delta\pi$	0 or 1	2	3	4	5
No	M1(E2)	E2(M3)	M3(E4)	E4(M5)	M5(E6)
Yes	E1(M2)	M2(E3)	E3(M4)	M4(E5)	E5(M6)

Table 2.2: The dominant  $\gamma$ -ray multipolarities for a  $|J_i - J_f|$  transition with parity change  $\Delta \pi$ . The lowest multipolarity is indicated, and the second is shown in parenthesis to indicate that it is usually not significant. The condition  $\lambda \leq J_i + J_f$  is assumed to be satisfied, and the  $J_i = J_f = 0$  transition is not allowed[26].

with  $\tau$  in ps, the transition energy  $E_x$  in MeV, and B(E2) in  $e^2 \text{fm}^4$ .

Transition matrix elements are experimentally found by measuring the lifetimes of excited states or the electromagnetic cross sections to the excited states provided the excitation mechanism is understood. Lifetime measurements such as the Doppler-Shift Attenuation Method (DSAM) and the Recoil Distance Doppler Shift (RDDS) method are based on the analysis of Doppler-shifted  $\gamma$ -ray peak shapes. In DSAM, nuclei are excited following fusion-evaporation reactions, Coulomb excitation, or inelastic scattering and, when the stopping power of the nuclei in the material is known, the Doppler shifts of the  $\gamma$  rays emitted by the recoiling reaction residues determine the points in time at which decay occurred and hence the lifetime of the excited state (suitable for  $\tau < 1$  ps)[27]. The RDDS method similarly uses the Doppler shift of  $\gamma$  rays emitted by an excited, recoiling nucleus to determine the lifetime of the state. A stopper is placed downstream of the target and the intensity ratio of  $\gamma$  rays emitted in-flight and stopped for different target-stopper distances provides a measure of the lifetime in the range  $10^{-12}$  s  $< \tau < 10^{-9}$  s[28]. The lifetime measurement methods have been recently extended to in-flight measurements of fast beams. In one method, the  $\gamma$  decay of a  $\tau \approx 1$  ns state in a reaction fragment moving at  $\beta \approx 0.4c$  produced a photopeak with low-energy tail due to a Doppler reconstruction that assumes  $\gamma$ -ray emission from the target location. The lifetime was extracted from the Doppler-shifted peak shape [29]. Another method similar to RDDS has the stopper replaced by a degrader to slow rather than stop the beam. The  $\gamma$  rays emitted before and after the degrader are Doppler shifted into separate photopeaks; the intensity ratio between the photopeaks for different target-degrader distances provides a measure of lifetimes over the range of 5–500 ps[30].

Nuclear resonance fluorescence (NRF), electron scattering, and Coulomb excitation determine transition rates through the measurement of cross sections. In a typical NRF experiment, a continuous photon spectrum (bremsstrahlung) irradiates a target of stable nuclei. The target nuclei are excited by the radiation and de-excitation  $\gamma$  rays are subsequently emitted with an angular distribution indicative of the transition multipolarity. The energy-integrated cross section of the scattered  $\gamma$  rays is inversely proportional to the lifetime of the excited state[31]. Electron scattering utilizes a simplified form of low-energy Coulomb excitation where the form factor in the Born approximation is related to the multipolarity of the transition. The transition rate can be extracted from the value of the form factor[32]. Due to the well-understood nature of the interaction and the ease of producing a large projectile flux, electron scattering is one of the most accurate methods of determining transition probabilities.

In Coulomb excitation, the interaction of the electromagnetic fields of the target nuclei and projectile nuclei leads to excitations with subsequent  $\gamma$ -ray emissions. The number of photons  $N_{\gamma,f\to i}$  observed in an inverse-kinematics Coulomb excitation experiment with  $\gamma$ -ray tagging is related to the excitation cross section by

$$\sigma_{i \to f} = \frac{N_{\gamma, f \to i}}{N_T N_B \epsilon} \tag{2.13}$$

where  $N_T$  is the number of target nuclei (in units of cm<sup>-2</sup>),  $N_B$  is the number of beam nuclei, and  $\epsilon$  is the efficiency of the experimental setup.  $N_B$  can be determined prior to interaction with the target, and  $N_T$  is given by the target

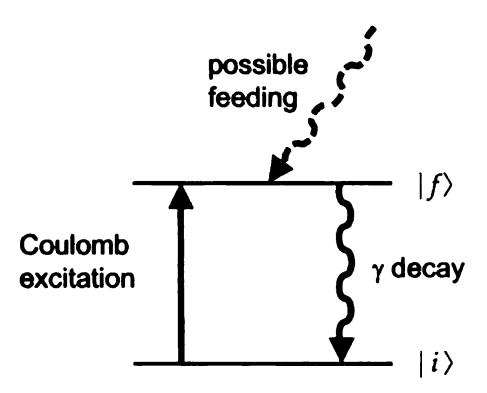


Figure 2.7: Schematic of Coulomb excitation of a nucleus from an initial state  $|i\rangle$  to a final bound state  $|f\rangle$  and the ensuing  $\gamma$  decay with a possible feeding transition from a higher state shown.

thickness. The efficiency accounts for the intrinsic and geometric efficiencies of all detector systems involved. Equation 2.13 assumes only one excited state; if more states than one are excited, possible feeding from higher excited states must be considered (see Figure 2.7).

The excitation cross section can be related to the reduced transition probability through various approaches. Coulomb excitation has long been employed at energies below the Coulomb barrier of the projectile-target system, where a Rutherford trajectory is assumed[33], and was proposed 30 years ago for higher energies[34]. Measurements of projectile Coulomb-excitation cross sections at beam energies well above the Coulomb barrier[35, 36] are ideal for rare-isotope experiments with low beam rates, which can be offset by reaction targets that are about 100–1000 times thicker than for below-barrier energies. Post-target particle identification permits inverse-kinematic reconstruction of each projectile-target interaction. Experiments at intermediate beam energies also allow for the unambiguous isotopic identification of incoming beam particles on an event-by-event basis, which is not generally possible at contemporary low-energy ISOL facilities. For this intermediate-energy Coulomb excitation work, the relativistic theory developed by Winther and Alder, which involves a semiclassical approach with first-order perturbation theory, has

been utilized[34]. Distorted-wave Born approximation calculations have also been used to determine transition rates from cross sections[35] and are in agreement with the excitation theory developed by Winther and Alder.

#### 2.4.2 Intermediate-energy Coulomb excitation

The most important difference between low- and intermediate-energy Coulomb excitation is possibility of nuclear interactions occurring above the Coulomb barrier. However, the inclusion of nuclear contributions to the measurement of electromagnetic transition rate can be prevented in heavy-ion reactions by considering only those projectiles scattered within a maximum scattering angle representing a "safe" minimum impact parameter  $b_{min}$  (see Figure 2.8). The radius  $R_{int}$  beyond which the Coulomb interaction dominates defines the minimum impact parameter to be allowed in the experiment. Wilcke  $et\ al$  use elastic scattering data to predict  $R_{int}$  for interactions between various nuclei[37]. For <sup>46</sup>Ar it has been shown that varying  $b_{min}$  where  $b_{min} \geq R_{int}$  has little effect on the measured transition rate value[38]. The minimum impact parameter is related to the maximum scattering angle in the center-of-mass system  $\theta_{cm}^{max}$  by

$$b_{min} = \frac{a}{\gamma} \cot(\theta_{cm}^{max}/2)$$

$$a = \frac{Z_{proj} Z_{tar} e^2}{m_0 c^2 \beta^2}$$
(2.14)

where  $\beta = v/c$  and  $\gamma = 1/\sqrt{1-\beta^2}$  are the velocity and Lorentz factor of the beam, and  $m_0$  is the reduced mass of the two nuclei.

The adiabatic cutoff of the Coulomb excitation process leads to reduced excitation probability beyond a maximum excitation energy

$$E_x^{max} \approx \frac{\gamma \hbar c \beta}{b} \tag{2.15}$$

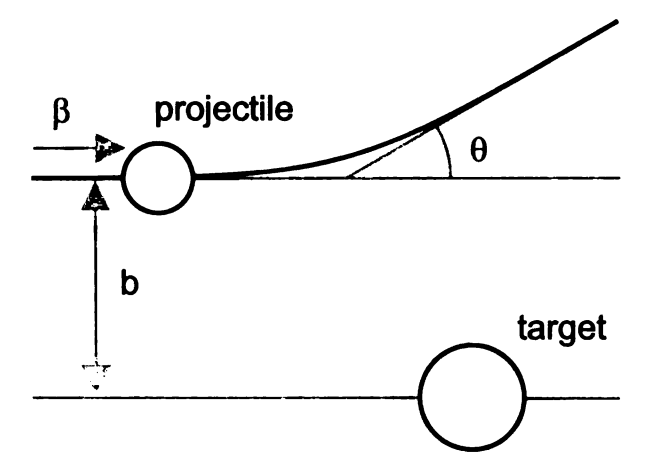


Figure 2.8: Schematic of a projectile nucleus scattering in the electromagnetic field of an infinitely heavy target nucleus. For a fixed beam velocity  $\beta = v/c$ , the scattering angle  $\theta$  depends on the impact parameter b. A maximum scattering angle is chosen in the experiment to restrict the minimum impact parameter.

where b is the impact parameter, and intermediate-energy beams can excite states at higher excitation energies compared to low-energy beams. For example, <sup>26</sup>Mg impinging on a  $^{209}$ Bi target with a beam velocity of  $\beta = 0.36$  has an adiabatic cutoff of  $E_x^{max} \approx 6$  MeV[39]. However, the possibility of feeding from excitations to states above the first 2+ state must be considered when calculating the excitation cross section[36]. Photons are used to identify the inelastic scattering process to bound excited states and hence target thickness is not constrained by the need to preserve momentum resolution to differentiate elastic and inelastic scattering. Higher energy beams allow for the use of thicker targets, and the number of scattering centers can be increased by as much as a factor of 1000 over low-energy experiments, permitting an equivalent decrease in the number of required proiectile nuclei. In typical intermediate-energy Coulomb excitation experiments, 1 beam particle in 10<sup>3</sup>-10<sup>4</sup> interacts with the target nuclei and multiple excitations are significant only to this small factor [36]. The wide range of scattering angles inherent in low-energy Coulomb scattering require large solid-angle detectors; a few degrees of acceptance suffices for intermediate-energy Coulomb excitation. At the NSCL, SeGA[40], an array of 18, 32-fold segmented, high-purity Ge  $\gamma$ -ray detectors, and APEX[41], 24 position-sensitive NaI(Tl) crystals, are used for Coulomb excitation measurements in conjunction with a phoswitch detector or the S800 spectrograph[42] for event-by-event particle identification. Similar setups are employed at GANIL[43], GSI[44], and RIKEN[35].

The angular distribution of the  $\gamma$  rays emitted depends on the multipolarity of the transition, electric quadrupole in this case, and on the minimum impact parameter. The magnetic substates in the final state are populated depending on the impact parameter of the interaction, which varies from  $b_{min}$  to infinity. The angular distribution can be calculated as described in Reference [45]. Although the angular distribution is symmetric with respect to the beam axis, the projectile is traveling at  $\beta \approx 0.3$ , and the Lorentz boost produces a forward-focused distribution in the laboratory frame.

# 2.4.3 The accuracy of intermediate-energy Coulomb excitation experiments

Several reports on initial results from low-energy Coulomb excitation measurements on <sup>30</sup>Mg[46, 47, 48] questioned the accuracy of the intermediate-energy approach and speculated that nuclear excitations are mixed with the Coulomb interaction regardless of the restriction to small scattering angles. The particular case of <sup>30</sup>Mg now seems resolved in that the previously reported discrepancy[49] has disappeared in the published low-energy result and is now in agreement with one intermediate-energy result[50], but not with another[51]. Responding to the general question raised, an examination of the accuracy of the intermediate-energy Coulomb excitation method was undertaken by comparing the "test cases" measured at intermediate beam energies at the National Superconducting Cyclotron

Laboratory at Michigan State University to adopted reduced transition matrix element values based on four or more independent measurements with complementary techniques that are available in the literature [25]. These test cases were measured over the past decade with the identical setups and during the same experiments used for measurements of unknown transition matrix elements. While these test cases have been individually reported previously in peer-reviewed journals together with the respective new measurements, their collective comparison to adopted values here reaffirms intermediate-energy Coulomb excitation as an accurate method relative to other transition rate measurement techniques.

The advantages of intermediate-energy Coulomb excitation are most pronounced when the method is applied to exotic nuclei with low production rates. Under these circumstances, the statistical uncertainty dominates. This difficulty is present irrespective of the method applied, and, therefore, only high statistics intermediate-energy Coulomb excitation measurements will be considered in determining the method's accuracy. A summary of intermediate-energy Coulomb excitation measurements of previously published transition rates along with their respective adopted values can be found in Figure 2.9(a). For these Coulomb excitation test cases, no feeding was observed. The adopted values are those compiled by Raman [52] where four or more independent transition rate measurements using any of the above techniques have been made for each nucleus. In the calculation of the adopted transition rate for <sup>40</sup>Ar, one of eight experimental values was measured using intermediate-energy Coulomb excitation, and for <sup>36</sup>Ar, two of eight. The error bars on the adopted values represent the relative uncertainties. The average difference from the adopted value is 6% and only one data point exceeds 10%. Note that all measurements are in agreement with their respective adopted values.

Figure 2.9(b) shows the relative differences between measured  $B(E2; 0_1^+ \rightarrow 2_1^+)$ 

transition rates and the adopted value[52] for  $^{26}$ Mg. The shaded area represents the uncertainty of the adopted value. The measurements were made using low-energy  $(x, x'\gamma)$  Coulomb excitation, NRF, DSAM, RDDS, and electron scattering. These traditional transition rate measurements have an average difference of 23% from the adopted value for  $^{26}$ Mg. The right-most data point, which deviates from the adopted value by 3%, was measured by Church et al.[39] using intermediate-energy Coulomb excitation at a beam energy of 66.8 MeV/nucleon. This specific measurement illustrates the more general point made in Figure 2.9(a) that intermediate-energy Coulomb excitation measurements that are not limited by statistics can readily measure transition rates with an accuracy of about 5% to a precision of about 10%.

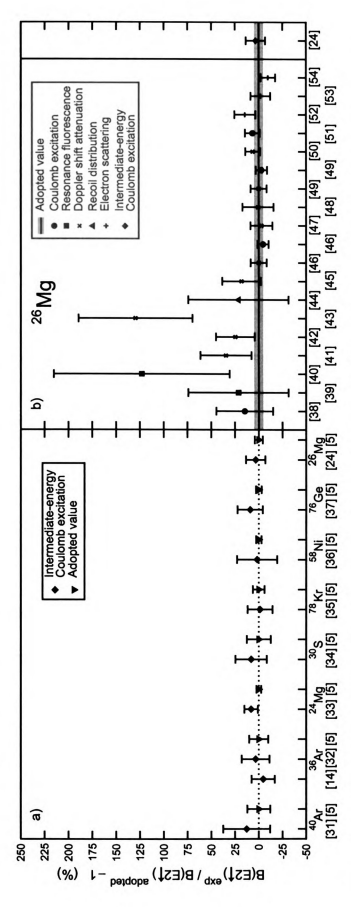


Figure 2.9: (a) The percent differences between adopted and measured  $B(E2;0_1^4 \to 2_1^4)$  transition rates for published test cases in intermediate-energy Coulomb excitation measurements. The average difference is 6%. (b) The percent differences between 19  $B(E2, 0_1^+ \to 2_1^+)$  transition rate measurements of  $^{26}$ Mg and the adopted value [52] (here [5]) compared to an intermediateenergy Coulomb excitation measurement (right-most)[39] of the same transition. The 3% difference of the intermediate-energy Coulomb excitation measurement compares favorably with the average absolute value of the difference of 23% for the other measurements. Adapted from Reference [25], where the citations may be found.

# Chapter 3

# Experimental apparatus

The experiment was performed using the Coupled Cyclotron Facility (CCF) at the National Superconducting Cyclotron Laboratory (NSCL) at Michigan State University. The three steps of radioactive ion beam production are primary beam production, fragmentation, and isotopic separation. At the CCF, a beam of stable ions is accelerated to approximately 0.5c and impinge upon a beryllium target. The fragmentation reaction produces a large number of different isotopes, and the isotopes of interest,  $^{50}$ Ca and  $^{52}$ Ti, are isolated by the A1900 Fragment Separator and transported to the experimental vault where intermediate-energy, inverse-kinematics Coulomb excitation with  $\gamma$ -ray tagging is performed using the S800 Particle Spectrograph and the APEX NaI(Tl)  $\gamma$ -ray detector.

## 3.1 Isotope production

The Coupled Cyclotron Facility at the NSCL consists of an electron cyclotron resonance ion source, two coupled cyclotron accelerators, and a fragment separator. In this experiment, a stable beam of <sup>76</sup>Ge was produced with a range of charge states by the ARTEMIS ion source. Since a cyclotron can only accelerate a single

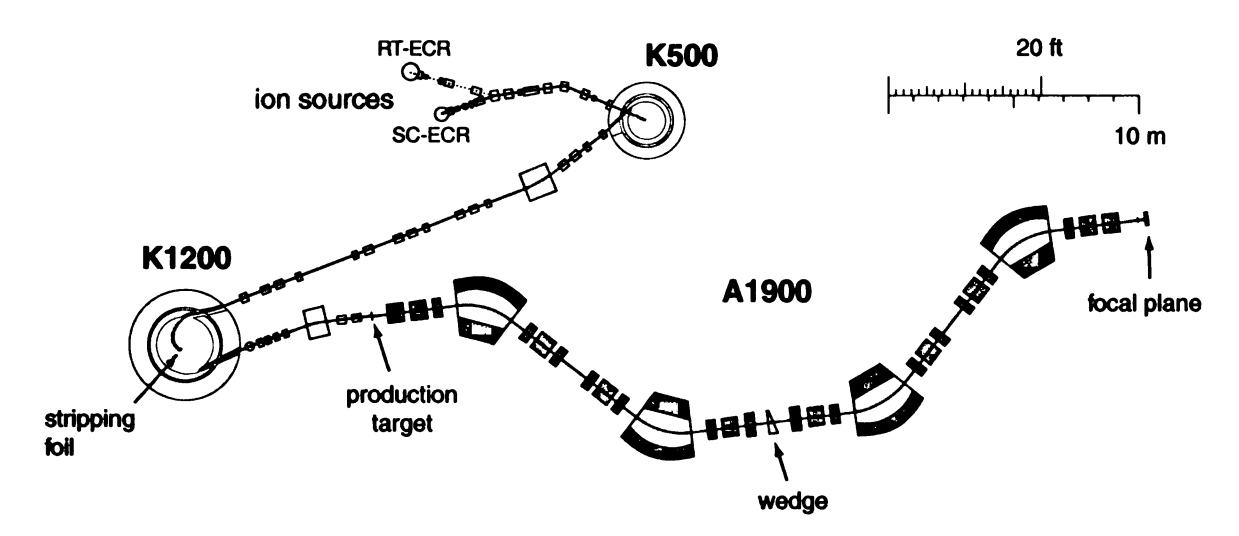


Figure 3.1: The Coupled Cyclotron Facility. A beam of <sup>76</sup>Ge is produced by the ion source, accelerated by the cyclotrons, and impinged on the production target. The fragments of interest are selected in-flight by the A1900 Fragment Separator and directed into the experimental vault.

charge state, one of the high intensity charge states,  $^{76}\text{Ge}^{+12}$ , was accelerated by the K500 cyclotron to 0.156c. The  $^{76}\text{Ge}$  nuclei are then stripped of electrons by passing through a 600  $\mu\text{g}/\text{cm}^2$  carbon foil, and the K1200 cyclotron accelerates the  $^{76}\text{Ge}^{+30}$  ions to 0.480c. The cyclotron operates at a frequency of 22.5 MHz (Figure 3.1).

The beam impinged on a 517 mg/cm<sup>2</sup> <sup>9</sup>Be production target, where a portion of the beam underwent fragmentation. In the first part of the two-step fragmentation process is a quick peripheral collision that produces a highly excited prefragment. The prefragment subsequently decays over a longer time scale through statistical nucleon emission, resulting in a broad distribution of stable and exotic nuclei[53]. The fragmentation reaction produces fast beams, allowing the study of short-lifetime isotopes, and it is independent of the chemical properties of the beam. The reaction does, however, generate a broad momentum distribution.

The beam fragments pass into the A1900 Fragment Separator[54], which uses a  $B\rho$ - $\Delta E$ - $B\rho$  selection to isolate the isotope of interest. Two dipole magnet bend the beam, selecting a magnetic rigidity  $B\rho = p/Z$ , where p = mv is the mo-

mentum of the fragments with relativistic mass m. The ions passed through an 369(1) mg/cm<sup>2</sup> achromatic aluminum wedge, introducing a Z-dependent energy loss described by the Bethe-Bloch equation. A second magnetic rigidity restriction on the wedge-induced isotopic momentum spread completes the isolation of the isotope of interest. Typically, the A1900 produces a cocktail beam consisting of the desired isotope and several other isotopes of similar A and Z. The  $^{50}$ Ca beam produced by the A1900 for this experiment consists primarily of  $^{50}_{20}$ Ca,  $^{51}_{21}$ Sc,  $^{53}_{22}$ Ti, and  $^{54}_{23}$ V, and the  $^{52}_{22}$ Ti beam contained significant proportions of  $^{50}_{21}$ Sc,  $^{53,54}_{23}$ V, and  $^{55}_{24}$ Cr. In this experiment, the momentum aperture at the wedge position limits the momentum spread to  $\Delta p/p = 3\%$  for  $^{50}$ Ca, and to  $\Delta p/p = 0.5\%$  for  $^{52}$ Ti. The difference in momentum spread is due to the production rate; higher rates permit greater selectivity.

At the exit of the A1900 is the extended focal plane, or XFP, where a scintillator is placed for time-of-flight measurements, which will be discussed in the following section. From the XFP, the ions are transported to the experimental vault. The beam reaches the S800 Particle Spectrograph with an efficiency of approximately 70%. For the case of <sup>50</sup>Ca, 10<sup>10</sup> particles/second (pps) of <sup>76</sup>Ge directed onto the production target produce 10<sup>2</sup> pps of <sup>50</sup>Ca at the focal plane of the S800.

# 3.2 The S800 Particle Spectrograph and the APEX NaI(Tl) Scintillator Array

The intermediate-energy Coulomb excitation measurement is performed using the S800's particle identification and tracking capabilities coupled with the APEX NaI(Tl) array to identify inelastically scattered beam projectiles. The  $\gamma$  rays produced by nuclei moving in intermediate-energy beams requires position-sensitive detectors for Doppler correction. One possible solution is diffusively-reflective scin-

tillator bars with photomultiplier tubes (PMTs) on both ends, and this method is utilized by the APEX NaI(Tl) scintillator array.

#### 3.2.1 The S800 Particle Spectrograph

The S800 Spectrograph is a high-resolution, high-acceptance particle spectrograph used for particle identification and tracking [42]. As can be seen in Figure 3.2, the beam from the A1900 is provided at the S800 Object, from which the analysis beam line directs the beam to the target position where a variety of radiation detectors may be stationed. In this experiment, the APEX NaI(Tl) array is stationed at the target position to tag inelastic scattering events. The beam continues into the spectrograph where dipole magnets spread the beam according to magnetic rigidity and finally into a detector package in the focal plane.

The S800 Focal Plane consists of an ion chamber for  $\Delta E$  measurements, two position-sensitive Cathode Readout Drift Chambers (CRDCs), and three scintillators for time-of-flight measurements (tof). The ion chamber and scintillators coupled with a scintillator at the exit of the A1900 allow for particle identification by plotting tof  $\propto p$  versus  $\Delta E \propto Z^2$ . The CRDCs are separated by a meter; the two position measurements determine the angle at which a particle passes through the focal plane. The transport of ions from one focal plane to another can be represented in general by a transport matrix T that describes the relationship between the positions x and y and angles from the beam axis  $a \approx \tan \alpha$  and  $b \approx \tan \beta$ .

$$\begin{pmatrix} x \\ y \\ a \\ b \end{pmatrix}_{target} = T \begin{pmatrix} x \\ y \\ a \\ b \end{pmatrix}_{FP}$$

$$(3.1)$$

The ion paths measured in the S800 Focal Plane can be mapped to the target focal plane by inverting T, which was determined by mapping the S800 dipole magnets. The scattering angle reconstruction has an uncertainty of  $0.05^{\circ}$ . The three focal plane scintillators are of 5, 10, and 15 cm thickness; only the first is required for heavy ions. The first scintillator is the source of the S800 particle trigger and can be used for time-of-flight measurements between the focal plane and the S800 Object or the A1900 XFP.

The S800 Spectrograph can run in two modes, dispersion matched and focused. In both modes, the beam provided by the A1900 is focused in space and dispersive in momentum at the S800 Object, where a timing scintillator is located. Since passing through the scintillator increases the angular dispersion of the beam, a focused position minimizes the total phase space of the beam. In focus mode, the analysis line is achromatic, and the beam is focused to a spot 1 cm FWHM at the at the target while remaining dispersed in momentum. The beam is then chromatic at the S800 Focal Plane, with the beam momentum width convoluted with the momentum loss in the target. The momentum acceptance of the S800 in focus mode is 4\%. The focal plane image is located at CRDC1, where the beam is focused in angle, and the dispersive position of the beam ion is dependent on momentum. In dispersion-matched mode, the entire system is achromatic, with the momentum spread of the beam at the object canceled at the focal plane. with the cost of a wide dispersion in momentum and space at the target. The momentum acceptance of the S800 in this mode is 1%, which corresponds to a beam width of 11 cm at the target. Since the intrinsic momentum of the beam is focused at the focal plane, this mode is provides a high resolution measurement of the momentum loss in the target. In this experiment, the higher acceptance of focus mode is needed to offset the low production rate of exotic nuclei. Moreover, identifying the Coulomb-excitation event with  $\gamma$ -ray tagging removed the need for

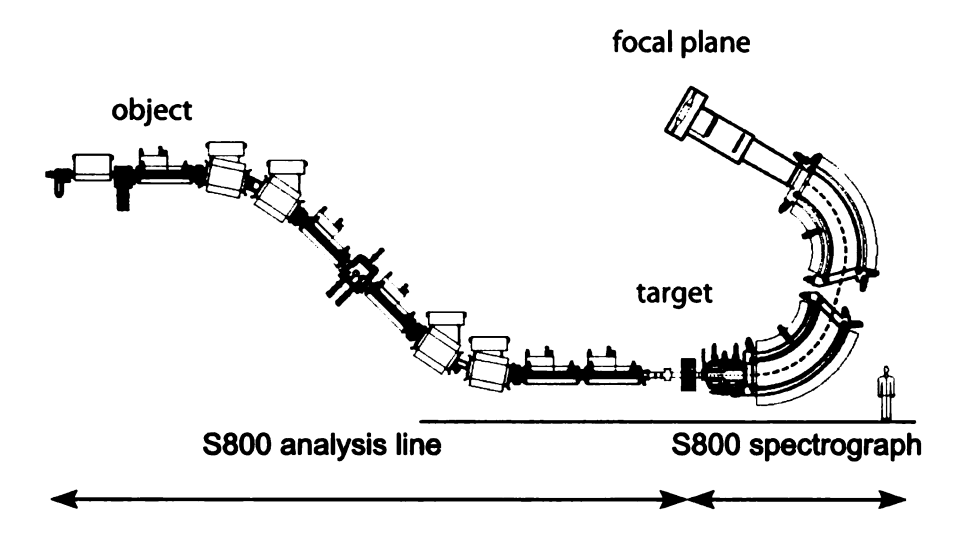


Figure 3.2: The S800 Particle Spectrograph. The beam enters from the left, passes through the target area where the  $\gamma$ -ray detector is located, and is transported into the focal plane for particle identification and tracking.

high momentum resolution.

## 3.3 The APEX NaI(Tl) Scintillator Array

#### 3.3.1 The detector

The identification of intermediate-energy Coulomb excitation events through the detection of emitted  $\gamma$  rays typically occurs with beam velocities of  $\beta=0.3$  at the NSCL. The transformation from the projectile to laboratory frame introduces a large Doppler shift as shown in Figure 3.3. The angular resolution may be achieved through segmentation of the detector, such as is done in the 18, 32-fold segmented, high-purity Ge detectors in the Segmented Ge Array (SeGA)[40] and the soon-to-be-completed CsI(Na) array CAESAR, or with a position-sensitive detector such as the APEX detector. The APEX detector was chosen for this experiment for its higher efficiency,  $\approx 7\%$  at 1 MeV compared to the  $\approx 2.5\%$  efficiency of SeGA. The detector was built as trigger detector for position annihilation radiation as

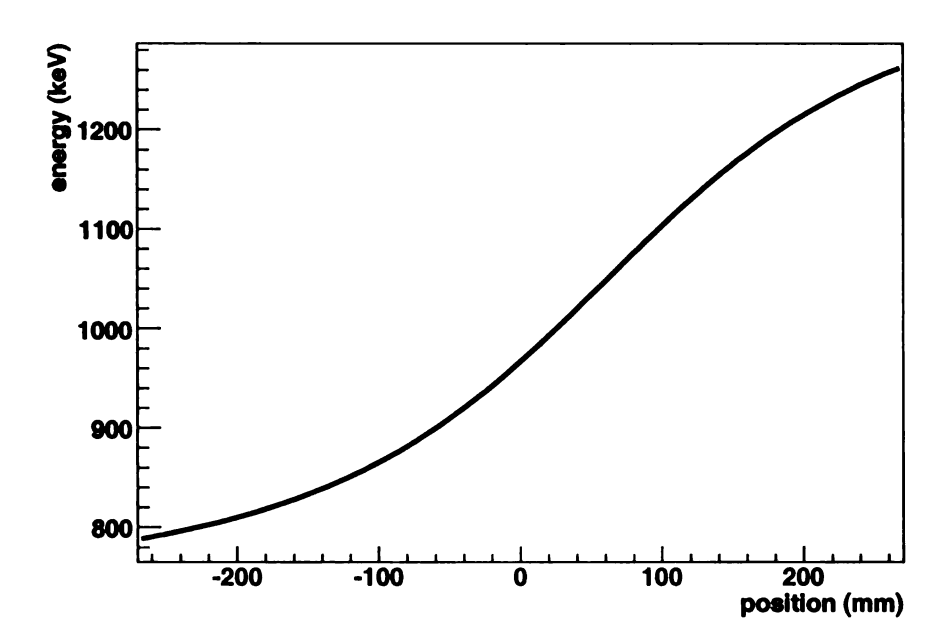


Figure 3.3: The laboratory-frame energy of a 1 MeV  $\gamma$  ray produced in a frame moving at  $\beta = 0.3$  as seen by the APEX detector. The energy is spread from 800 keV to 1.3 MeV.

part of the APEX experiment at the ATLAS accelerator at Argonne National Laboratory[55] and will be referred to by the shortened name "APEX" in the following discussion.

The APEX Array [56, 41] consists of 24 trapezoidal cylinders of NaI(Tl) arranged in a barrel configuration. Each detector bar is jacketed in 0.4 mm of steel with a 1.1 cm thick quartz window leading to a photomultiplier tube at both ends. The bars are 55.0 cm long and 6.0 cm thick, and they have inner and outer trapezoidal faces of 5.5 and 7.0 cm respectively. The barrel of detectors is surrounded by a 1.9 cm thick lead tube for background shielding, and the entire array is surrounded by and mounted on a 1.0 cm thick steel tube. The steel tube has wheels that allow the array to be mounted on rails. The shielding is a key component of the array; the large volume of NaI(Tl) is highly efficient, and without the shielding  $\gamma$ -ray source calibration measurements would have a large deadtime due to background radiation. The array is shown in Figure 3.4.



Figure 3.4: A photo of the APEX Array with twenty-four NaI(Tl) bars with PMTs at each end and a lead and steel shield.

Inorganic scintillators with activators such as NaI(TI) function by producing light when radiation falls on the crystal. The material must be transparent to the emitted light, and the luminescence decay time must be short. As is typical of the structure of insulators and semiconductors, the NaI crystal lattice permits electrons to lie in discrete energy bands, a lower valence band and a higher conduction band (Figure 3.5). Incident radiation deposits energy that boosts electrons from the valence band to the conduction band. Photon decay from the conduction band to the valence band is an inefficient process and produces light of the same energy as the band gap. This light may then boost another electron into the valence band, reducing the light output of the crystal. The introduction of an activator atom, thallium in this case, produces local energy levels in the forbidden band. The conduction-band electron quickly encounters an activator site, where it can recombine with a hole, leading to light emission. The reduced energy of the recombination transition leads to light in the visible region where the crystal is transparent.

During the experiment, APEX sits at the target position of the S800 flush against the beamline gate valve to the S800's entrance quadrupole magnet. APEX must sit close to the magnet because the projectile  $\gamma$  rays are forward focused but

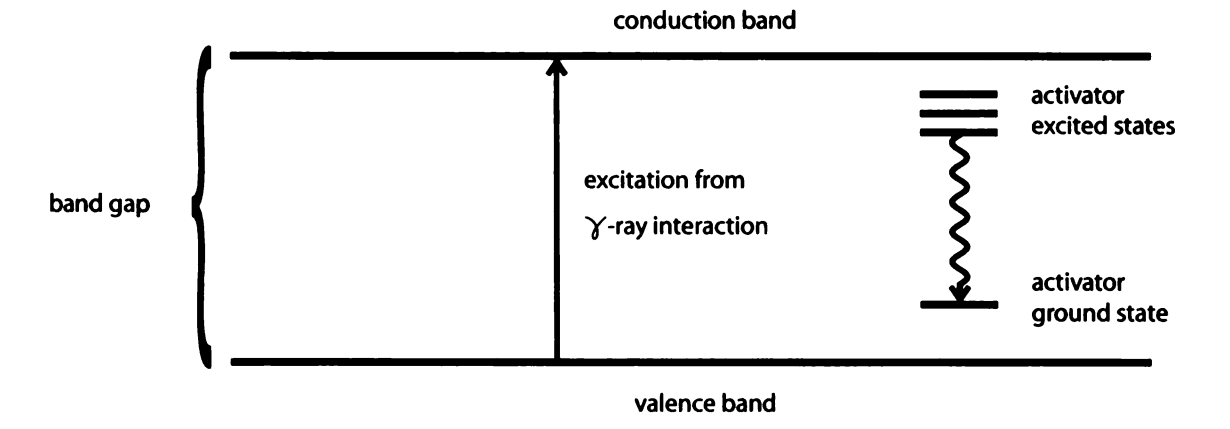


Figure 3.5: The scintillation process. The interaction of  $\gamma$  rays with the scintillator crystal excites electrons from the valence band to the conduction band. The electron drifts to an activator site where it decays to the valence band through a multi-step process including photon emission.

the array is large enough that center of the array is approximately 60 mm upstream from the target position of the S800. The large magnetic fields produced by the quadrupole magnet far exceed those in which a standard PMT can function; APEX uses the Hamamatsu H2611 PMT, whose closely-spaced fine mesh dynodes function in fields beyond 1 T. However, the trade-off for PMTs that function near the beamline magnet is a reduced pulse-height resolution relative to standard PMTs.

Position resolution is achieved by diffusively grinding the sides of the NaI(Tl) crystal bar, causing the incident light to reflect in a random direction. The cumulative effect is an exponential attenuation of scintillation photons  $N_{ph}$  as they move away from the scintillation position z as measured from the center of the bar of length L. In this case, the number of photoelectrons produced in the PMTs of quantum efficiency  $\epsilon_i$  is then

$$N_{PE,1} = \epsilon_1 \frac{N_{ph}}{2} e^{-\mu(L/2+z)}$$

$$N_{PE,2} = \epsilon_2 \frac{N_{ph}}{2} e^{-\mu(L/2-z)}$$
(3.2)

where  $\mu$  is the light attenuation coefficient per unit length. A value of  $\mu = 0.047/\text{cm}$  was chosen to achieve a position resolution of 3.0 cm FWHM. With the PMT and amplifier gains and analog-to-digital conversion collectively symbolized by a factor  $g_i$ , the recorded detector output is

$$A_1 = g_1 N_{PE,1}$$
 (3.3)  
 $A_2 = g_2 N_{PE,2}$ .

Solving this system of equations for z leads to

$$z_{rec} = \frac{1}{2\mu} \left( \ln \frac{A_2}{A_1} - \ln \frac{g_2 \epsilon_2}{g_1 \epsilon_1} \right). \tag{3.4}$$

The energy E of the  $\gamma$  ray is proportional to  $N_{ph}$ ,

$$E_{rec} = \sqrt{A_1 A_2} = \sqrt{\epsilon_1 \epsilon_2 g_1 g_2} \frac{N_{ph}}{2} e^{-\mu L}. \tag{3.5}$$

The end face of the crystal has an area of  $37.5~\rm cm^2$ . It is attached to a quartz window of area  $15.2~\rm cm^2$  that connects to a  $10.2~\rm cm^2$  active PMT face. The geometry of the detector reduces the number of scintillation photons reaching the photocathode by 73%, and optical transmission losses lead to a further reduction of around 25%. The exponential attenuation of the scintillation photons, their low transmission to the PMT, and the magnetic-field resistant PMTs, each one vital to the feasibility of the experiment, altogether lead to an energy resolution significantly degraded from the typical resolution of an NaI(Tl) detector as shown in Table 3.1. An energy spectrum from an  $^{88}$ Y  $\gamma$ -ray source detected by APEX is shown in Figure 3.6.

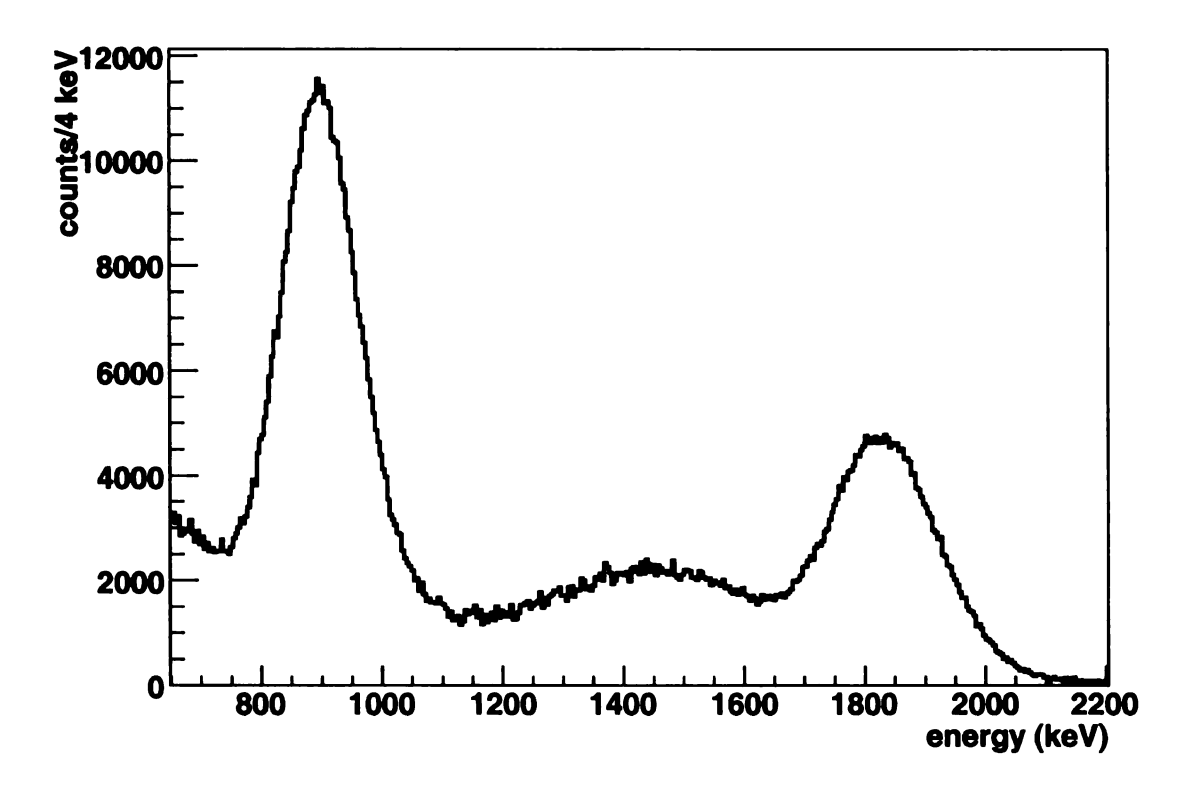


Figure 3.6: The energy spectrum of an  $^{88}$ Y  $\gamma$ -ray source produced by APEX.

#### 3.3.2 Electronics

The electronics for recording data from APEX were assembled specifically for this experiment and consist two parts: one that digitizes the electrical pulse and another to select those events that are coincident with a beam particle. The large mass of the array very efficiently absorbs background radiation, and the coincidence timing provides a means of rejecting all  $\gamma$ -ray data that is not time-correlated with a beam particle, reducing the room background to a very small part of the in-beam background.

A high-voltage power supply provides approximately 2 keV to each of the 48 PMTs. Signal cables carry the output of those 48 PMTs to CAEN N568B Spectroscopic Amplifiers. The N568B provides three outputs, a shaped and amplified signal, that same signal with a further 10x amplification (not used in this exper-

detector	energy	resolution
	(keV)	(% FWHM)
APEX	662	19
	898	16
	1836	11
typical NaI	662	7

Table 3.1: The resolution of APEX compared to that typical of a 3"x3" NaI(Tl) crystal.

iment), and a fast, fixed-amplification signal for timing. The PMT voltage and amplification were chosen as described in the following section. The shaping time of 1  $\mu$ s was chosen to maximize resolution while minimizing deadtime. The shaped and amplified signals are then digitized by CAEN V785 ADCs.

The timing signal travels from the amplifier fast output into a LeCroy 3420 Constant Fraction Discriminator. Signals that exceed the threshold for a given channel are passed through to a CAEN C469 Gate and Delay Generator and are multiplexed into a single signal, the APEX trigger. The multiplexed signal is passed to the S800 trigger logic, where it is combined with the S800 trigger. Two types of triggers are accepted, a downscaled S800 particle trigger to measure the number of beam projectiles and an APEX-S800 coincidence trigger to record projectile-correlated  $\gamma$  rays. The master trigger is then returned to the APEX electronics, where it is split by a gate generator. The trigger gate generator produces a short logic pulse that starts a CAEN V775 TDC that is later stopped by the now-delayed signal for each channel coming from the gate and delay generator. The trigger gate generator also produces a long gate that opens the CAEN V785 ADC to accept the shaped signal from the amplifier. In this manner, the energy of particle-coincident  $\gamma$  rays and the time difference between particle and  $\gamma$ -ray detection is recorded. A schematic of the electronics is shown in Figure 3.7.

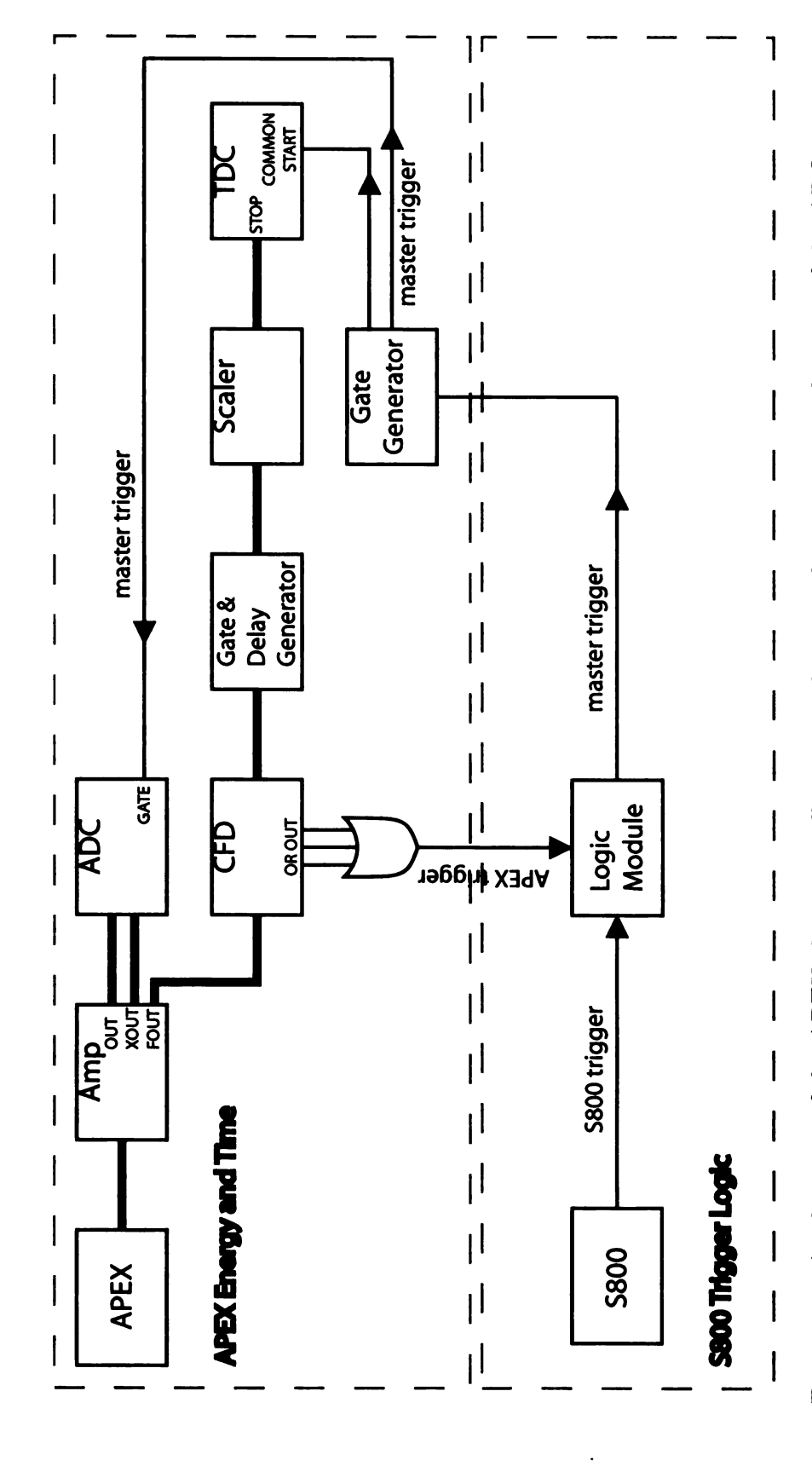


Figure 3.7: A schematic of the APEX electronics illustrating the coincidence timing and gating of the ADC.

#### 3.3.3 Calibrations

APEX must be calibrated for energy and position, and the calibration consists of an approximate hardware calibration and a precise software calibration. A planar-collimated  $^{60}$ Co  $\gamma$ -ray source is used for the calibrations. This source consists of a  $^{60}$ Co source sandwiched between two Heavimet disks so that  $\gamma$  rays are emitted radially in a plane. The disks are placed concentric with APEX so that e.g. with the source at the center of the array all detectors are illuminated at only the center of the bars. The hardware calibration was performed by placing the source at the center of the bar, adjusting the PMT voltage until the signals from both sides each bar were roughly equal and then finely adjusting with the amplifier.

For the position calibrations, data were collected with the collimated source position positioned at 1.5" increments along the length of the detector. The peaks in the reconstructed spectra were fitted, and a third order polynomial was used to map the fit centroids onto the actual position of the source. The range of the position calibration is limited by the breakdown of the exponential attenuation model at the ends of the bars.

The energy calibration utilized  $^{137}$ Cs and  $^{88}$ Y  $\gamma$ -ray sources, providing calibration points below, near, and above the energy of interest at 1 MeV.  $^{60}$ Co is not used for the energy calibration because the two  $\gamma$ -ray peaks at 1173 and 1332 keV are not well separated in the energy spectrum. Software gates were placed on the uncalibrated position so that fifteen energy calibration slices were created for each bar. For each source  $\gamma$ -ray energy, the centroid of the reconstructed energy was fit with a Gaussian and linear background as shown in Figure 3.8. A linear function was used to map the centroids onto the  $\gamma$ -ray source energies. In this manner, the energy spectrum was calibrated.

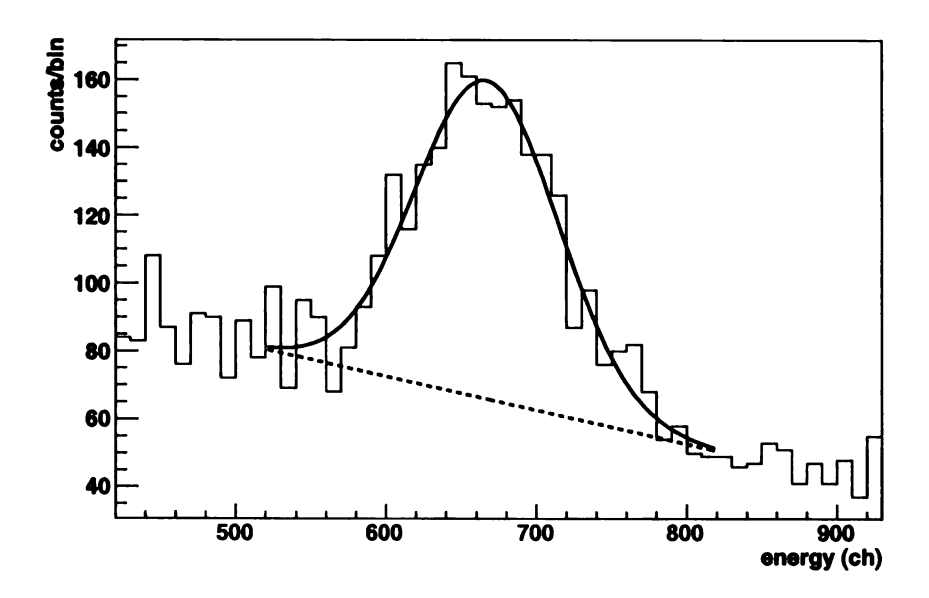


Figure 3.8: The fit of the 898 keV  $\gamma$ -ray energy peak in one slice of detector 2 using a Gaussian with a linear background as the fitting function. The centroid channel, along with those of the 662 and 1836 keV photopeaks of  $\gamma$ -ray calibration sources, was mapped to the source energy to complete an energy calibration.

### 3.3.4 Efficiency

The total efficiency of the array was calculated using calibrated  $\gamma$  sources at the target position and summing the energy spectra from each bar. The  $\gamma$ -ray peak was fit using a Gaussian plus a linear background, and was compared to the number of  $\gamma$  rays produced by the source while accounting for deadtime. Three of the twenty-four detectors were not functioning for this experiment, and are not included in the analysis. The measured efficiency is 11.6% at 898 keV and 7.4% at 1836 keV.

An intriguing effect comes to light upon examining the position spectra of the energy peaks. As shown in Figure 3.9, the 1836 keV  $\gamma$  ray of <sup>88</sup>Y produces an isotropic distribution of a point source; however, the 898 keV  $\gamma$  ray does not. To see how this can happen, consider the ideal case, where the detector response would resemble what is simulated in Figure 3.10. The source, <sup>88</sup>Y in this case, produces an isotropic distribution of  $\gamma$  rays in the position response of the detector.

Recalling that the energy and timing signals are separated by the amplifier, let it be assumed that without altering the energy signal a high-resolution signal is fed into the discriminator, which cuts off energies below a fixed minimum. The output signal from each PMT has a position dependence, which leads to the fixed-value threshold being realized as a position-dependent threshold. The exponential attenuation of the scintillation photons towards the end of the bar coupled with the acceptance of all events that exceed either threshold results in the appearance of an exponential increase in the threshold moving away from the end of the bar. In this idealized case, a 600 keV  $\gamma$  ray that interacts at 150 mm would exceed the threshold on the positive side of the detector but not on the negative, and vice versa if the  $\gamma$  ray had interacted at -150 mm. Had the  $\gamma$  ray fallen on the center of the bar, the threshold would not be exceeded on either side, and the event would not be recorded.

Figure 3.11 illustrates this effect in APEX. The low resolution of the array coupled with the short shaping time of the fast output of the amplifier leads to the discriminator triggering on widely varying signals for  $\gamma$  rays of a single energy. Rather than a high-resolution signal being fed into the discriminator, the discriminator acts on a signal of lower resolution than the energy signal, resulting in an indistinct threshold. This threshold effect distorts the 898 keV position response but not that of the 1836 keV  $\gamma$  ray in Figure 3.9. It is probable that this effect was present in previous work with APEX [57, 41], with the extent of the efficiency loss depending on the amplitude of the threshold. Reducing the position-dependent effect of the threshold can be accomplished by reducing the light attenuation factor  $\mu$ , but doing so would reduce the position resolution of the detector—a vital component of Doppler reconstruction. Alternatively, the threshold may be reduced, increasing deadtime due to the many low-energy events at the extremes of the detector. The position-dependent threshold, an inherent characteristic of the

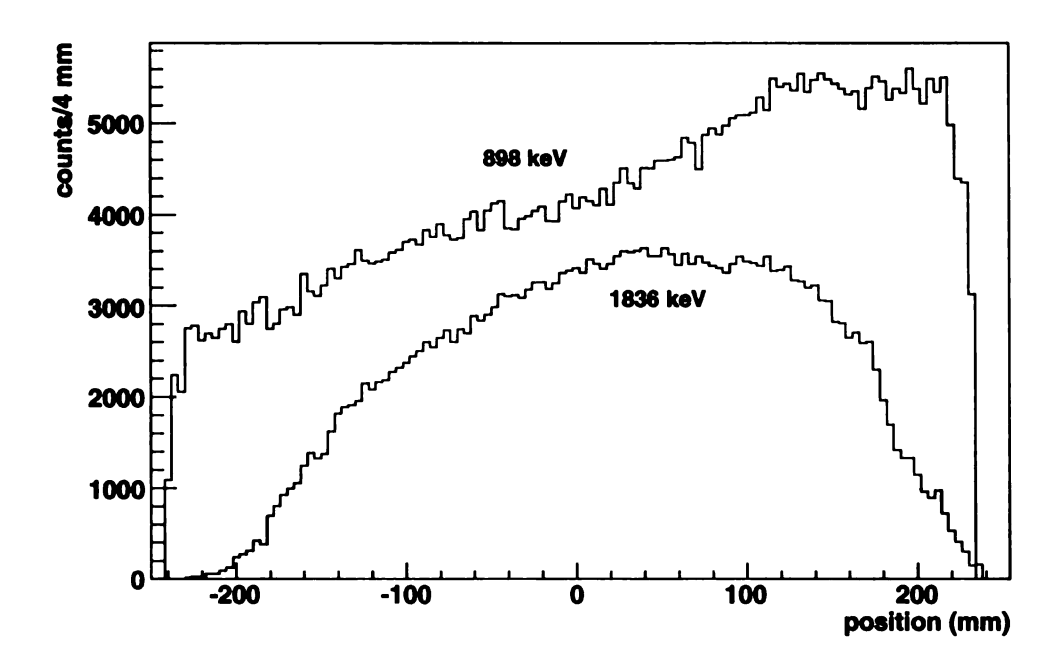


Figure 3.9: The position response of APEX for an  $^{88}$ Y  $\gamma$ -ray source placed at 60 mm. The 1836 keV  $\gamma$  ray produces an isotropic distribution (with a slight effect from the maximum range of the ADC) while the 898 keV  $\gamma$  ray does not.

detector, forces a trade-off between efficiency, position resolution, and deadtime. Fortunately, the experiment is possible with this effect.

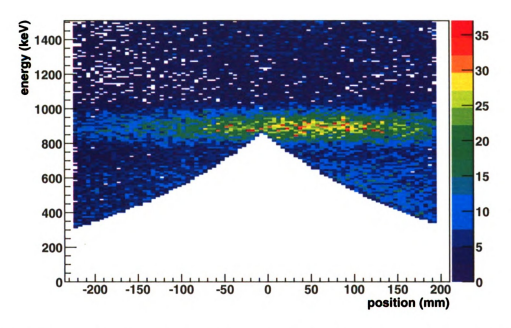


Figure 3.10: A simulated position-energy matrix for a double-sided scintillator bar with a high-resolution signal input into the discriminator. The exponential attenuation of the scintillation photons is realized as exponential increase in the threshold towards the center of the bar.

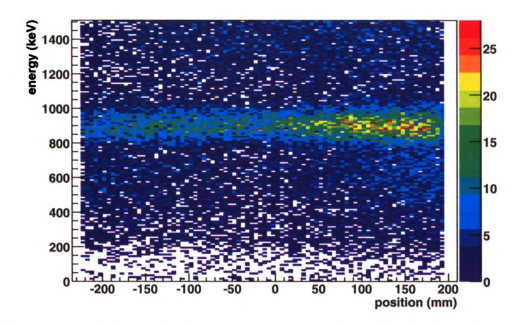


Figure 3.11: A simulated position-energy matrix of a double-sided scintillator bar such as those of APEX with a low-resolution signal input into the discriminator. This figure and the ideal case figure differ only in the threshold. Although the efficiency has decreased, the low resolution leads to an indistinct threshold energy cut off.

# Chapter 4

# **Simulation**

The key quantity in this investigation of nature is a cross section, the ratio of the number of  $\gamma$ -ray emitted to the number of possible Coulomb excitation reactions. In the previous chapter it was explained that measuring the  $\Delta E$  and time of flight of a particle is sufficient to identify the isotope, and the detection of  $\gamma$  rays will now be considered in detail. The difficulty of  $\gamma$ -ray spectroscopy lies in the fact that a monoenergetic  $\gamma$  ray will not produce a monoenergetic response. Instead,  $\gamma$  rays interact with materials via three major processes, the photoelectric effect, the Compton effect, and pair production, to produce a detector response function extending from zero energy to somewhat above the  $\gamma$ -ray energy. Coulomb-excited beam projectiles adds the complexity of  $\gamma$ -ray emission in an electric quadrupole angular distribution folded with a  $\beta \approx 0.3$  Doppler boost. A model of the detector response that includes the angular distribution of  $\gamma$ -ray emission and the kinematics of the projectile can produce response functions for fitting to the data. The response function can translate the shape of the  $\gamma$ -ray energy spectrum into the number of  $\gamma$  rays detected. With a known efficiency the number of  $\gamma$  rays emitted is determined.

In this chapter, the focus is the determination of response functions to extract

the number of  $\gamma$  rays detected from the energy spectrum. A simulation of the detector response of APEX was created using GEANT4 [58, 59], a C++ toolkit developed at CERN for simulating the interactions of radiation with matter. There are four parts to the simulation: the detector geometry, the  $\gamma$ -ray generator, the interaction physics, and the model of the detector and electronics. The model is then compared to the detector response of laboratory-frame  $\gamma$ -ray sources and inbeam Coulomb excitation reactions. Efficiency will be discussed in the following chapter.

## 4.1 Detector Geometry

The basic building block of the APEX Array is a single detector bar. The simulation bar consists of the NaI crystal, steel jacket, and quartz window with the dimensions described in Section 3.3. The 24 bars are arranged in a barrel and surrounded by the lead and steel shields as shown in Figure 4.1. Finally, the 6" Al beam pipe was added, and target foils are inserted when needed for Coulomb excitation simulations. The 66"x22"x0.5" aluminum table on which APEX sits was included to determine if backscattering from large objects outside the array affected the detector response; a negligible difference was noted, and no other objects were included.

## 4.2 $\gamma$ -ray generator

 $\gamma$ -ray calibration sources used in the laboratory emit  $\gamma$  rays of fixed energies isotropically from a point. The sources contain an unstable isotope that  $\beta$  decays into excited states of the daughter isotope, which then transition to the ground state by  $\gamma$ -ray emission. The proportion of  $\beta$  decays that produce a given  $\gamma$  ray is termed



Figure 4.1: The APEX detector geometry constructed in GEANT4. On the left is a view looking down the beam pipe with the target at the center and the array surrounding. On the right is view of APEX from the outside.

the intensity ratio of that  $\gamma$  ray. The characteristics of the source are modeled in the simulation for a single event through the following process: the intensity ratio is used to determine if each of the  $\gamma$  rays emitted by the source will be emitted in that decay. The  $\gamma$  ray that is selected to be emitted has its energy and a direction chosen randomly from an isotropic distribution passed to the primary event generator queue. Once all  $\gamma$  rays are in the queue, the event generator produces all of them at once from a single point. For example, the 898 keV line <sup>88</sup>Y has an intensity of 94.0%, and the 1836 keV line has an intensity of 99.4%. Each primary event has a 94.0% probability of containing an 898 keV  $\gamma$  ray computed by sampling a random number from a flat distribution. On the occasion that the 898 keV  $\gamma$  ray is to be emitted, a random, isotropically-distributed vector is selected, and the  $\gamma$  ray is added in the primary event generator queue. The 1836 keV  $\gamma$  ray is similarly treated, and in this example will also be emitted. A second random direction is chosen, and subsequently the two  $\gamma$  rays in queue are emitted. The simulation then tracks those  $\gamma$  rays until they have deposited all energy or they have left the

simulation's world.

The in-beam  $\gamma$  ray generator includes a number of additional features. In the projectile frame, the  $\gamma$  rays are not distributed isotropically but rather with an electric quadrupole distribution along the beam axis as discussed in Section 2.4.2.

$$P(\theta_{proj}) = \left\{ a_0 L_0(\sin \theta_{proj}) + a_2 L_2(\sin \theta_{proj}) + a_4 L_4(\sin \theta_{proj}) \right\} \sin \theta_{proj} \quad (4.1)$$

and an equiprobable distribution in  $\phi_{proj}$ . While the  $\phi_{proj}$  component, lying perpendicular to the beam direction, is not altered in the transition from the projectile frame to the laboratory frame; the  $\gamma$ -ray energy and the E2-distributed  $\theta$  component are relativistically boosted. The relation between the projectile and laboratory frame is given by

$$E_{\gamma lab} = E_{\gamma proj} \gamma (1 + \beta \cos \theta_{proj}) \tag{4.2}$$

$$E_{\gamma lab} = E_{\gamma proj} \gamma (1 + \beta \cos \theta_{proj})$$

$$\theta_{lab} = \frac{\cos \theta_{proj} + \beta}{1 + \beta \cos \theta_{proj}},$$

$$(4.2)$$

where  $\beta \sim 0.3$ . In Figure 4.2 the isotropic angular distribution is compared to the E2 angular distribution emitted by <sup>52</sup>Ti after Coulomb excitation on a <sup>nat</sup>Au target with a midtarget velocity  $\beta = 0.363$ . In the experiment, the  $\beta$  of emission forms a distribution according to the beam momentum width  $\delta p$  with

$$\frac{\delta p}{p} = \gamma^2 \frac{\delta \beta}{\beta} \tag{4.4}$$

Experimentally, the incoming beam has a momentum selected by the magnetic rigidity of beam-line magnets and a width chosen by the slits in the A1900. Passing through the target broadens the momentum, which is then measured in the S800. Ultimately, the position resolution of APEX is insufficient for the array to be sensitive to momentum widths of a few percent typical at the NSCL.

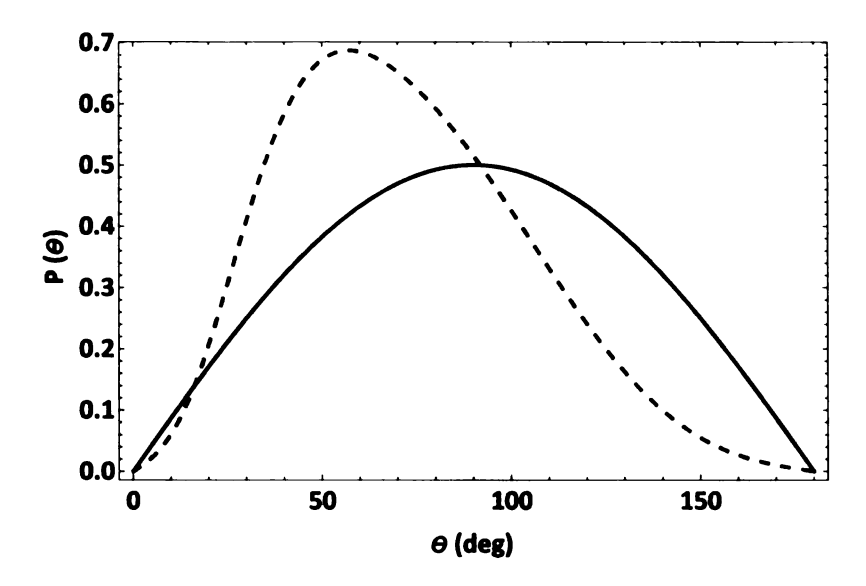


Figure 4.2: An isotropic angular distribution (solid line) is compared to the E2 distribution produced by the Coulomb excitation of  $^{52}$ Ti on a  $^{nat}$ Au target at  $\beta = 0.363$ .

In the laboratory frame, the projectile source emission position is spread over a large volume relative to the point-like calibration source. The beam impinges on the target with a normal distribution of approximately 1 cm FWHM in both the vertical and horizontal directions. The position of the emission in the beam direction depends on the lifetime of the excited state. The B(E2) is related to the lifetime  $\tau$  by the relation given in Equation 2.12. Since the de-excitation transition is subject to exponential decay, the position of  $\gamma$  ray emission is exponentially distributed. Thus, with the excitation occurring on average in the middle of the target, the probability of emission at a distance d from the target center is governed by

$$P_{emission}(d) = e^{-\frac{d}{\beta c\tau}}. (4.5)$$

A plot of this distribution is given for  $^{52}{\rm Ti}$  in Figure 4.3. The majority of the  $\gamma$  are emitted outside of the target.

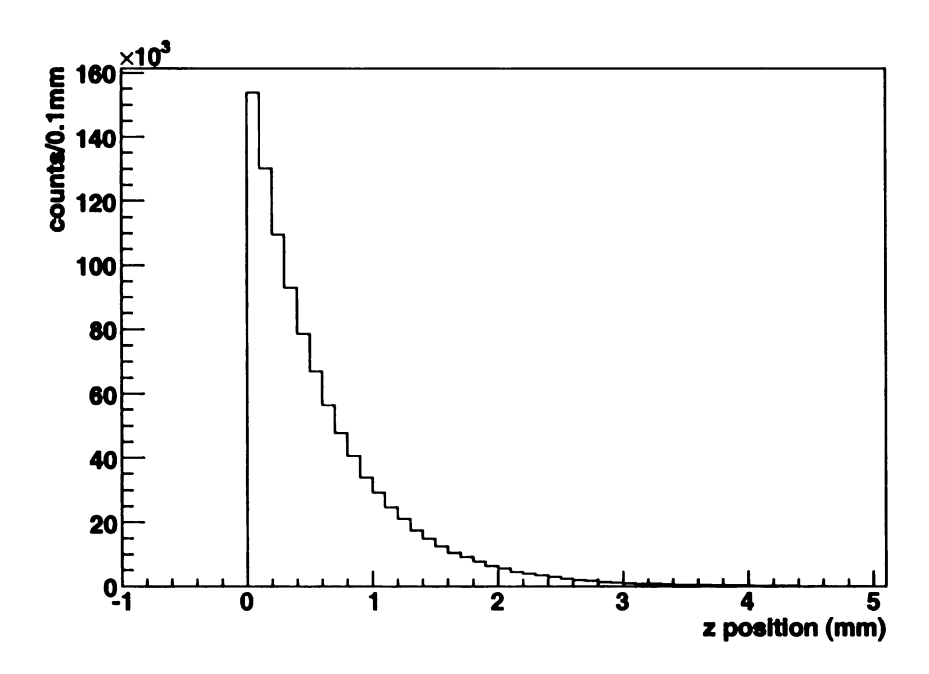


Figure 4.3: The simulated  $\gamma$ -ray emission position along the beam line with z=0 at midtarget. The exponential decay in time of the excited states leads to an exponential decay in position of  $\gamma$ -ray emission. The target is approximately 0.1 mm thick (one bin), and most  $\gamma$  rays are emitted outside of the target.

## 4.3 Interaction physics

 $\gamma$  rays deposit energy in materials via three major processes, the photoelectric effect, pair production, and Compton scattering [60]. All three processes involve an abrupt transfer of photon energy to electron energy with the photon either vanishing or scattering. The photoelectric effect is dominant at lower energies, Compton scattering predominates at the 1 MeV energies discussed here, and pair production grows more important at higher energies. These three interactions produce the characteristic form of the detector response, a Gaussian photopeak atop a Compton continuum extending toward low energies.

In the photoelectric effect, the photon interacts with an atom and vanishes. An electron is ejected from the atom, mostly probably from the most tightly bound, or K, shell if the photon energy  $h\nu$  is sufficient. The photoelectron carries with it

a kinetic energy

$$E_{e-} = h\nu - E_b \tag{4.6}$$

where  $E_b$  is the original binding energy of the ejected electron. The ionized atom quickly absorbs a free electron or rearranges its shells, either releasing x rays or an Auger electron. The energy of the x rays and Auger electrons is re-absorbed after traveling typically less than 1 mm. The result of the photoelectric effect is then a photoelectron that carries most of the  $\gamma$ -ray energy and local effects of lower energy. If nothing escapes from the detector, the full energy of the  $\gamma$  is deposited in the detector, and the result of many monoenergetic  $\gamma$  rays undergoing photoelectric effect interactions is a delta function in the energy spectrum at the incident  $\gamma$ -ray energy,  $E_{\gamma}$ .

The absorption of the full photon energy means that the photoelectric effect is the ideal interaction for determining the energy of the incident  $\gamma$  ray. The probability of photoelectric absorption per atom  $\tau$  is approximately

$$\tau \propto \frac{Z^{4.5}}{E_{\gamma}^3}.\tag{4.7}$$

The strong dependence on Z is the reason lead is used for APEX's shield and part of the reason NaI (Z(I) = 53) is an excellent scintillator.

Compton scattering is the most likely interaction at energies around 1 MeV that are of interest for this experiment. The process occurs when a  $\gamma$ -ray photon interacts with an electron and is deflected by an angle  $\theta$  with respect to the original trajectory as shown in Figure 4.4. In doing so, the photon transfers some energy to the recoiling electron. The conservation of energy and momentum leads to an

expression for the energy  $h\nu'$  of the deflected photon,

$$h\nu' = \frac{h\nu}{1 + \frac{h\nu}{m_0 c^2} (1 - \cos\theta)}$$
 (4.8)

where  $m_0c^2$  is the energy of an electron at rest. To illustrate the results of Compton scattering on the energy response of the detector, consider two extreme cases. For a very small scattering angle  $\theta\approx 0$  the recoil electron absorbs very little energy. In the case of a very large scattering angle where  $\theta\approx \pi$  the kinetic energy  $E_{e^-}$  of the recoil electron is

$$h\nu'|_{\theta=\pi} = \frac{h\nu}{1+2h\nu/m_0c^2}$$
 (4.9)

$$E_{e^{-}}|_{\theta=\pi} = h\nu - h\nu' = h\nu \left(\frac{2h\nu/m_0c^2}{1 + 2h\nu/m_0c^2}\right)$$
 (4.10)

Thus, Compton scattering deposits anywhere from zero to  $\Delta E_C = h\nu - E_{e^-} \mid_{\theta=\pi}$  energy in the interaction material. For monoenergetic  $\gamma$  rays the result is a peak beginning  $\Delta E_C$  below the incident photon energy with a continuum extending to zero.

The third significant process by which  $\gamma$  rays interact with materials is pair production. Pair production occurs when a  $\gamma$  ray of at least 1.02 MeV vanishes in the presence of an atom to produce an electron-positron pair. The energy of the photon above the rest mass of the electron-positron pair is carried away as kinetic energy.

$$E_{e^{-}} + E_{e^{+}} = h\nu - 2m_0c^2 \tag{4.11}$$

The kinetic energy of the electron and positron is lost within a few millimeters of the interaction point. The thermalized positron will annihilate with another electron and produce two photons of energy  $m_0c^2$ . If the detector is large enough,

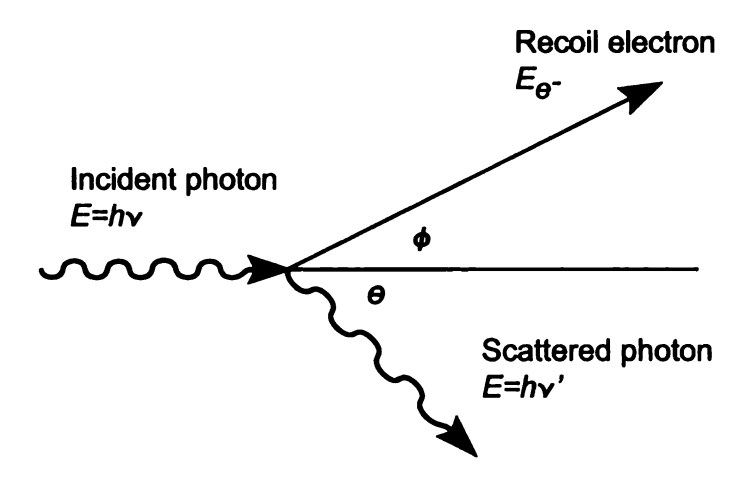


Figure 4.4: A kinematic diagram of a  $\gamma$  ray of energy  $h\nu$  Compton scattering on an electron at an angle  $\theta$  with energy  $h\nu'$ .

these photons will be re-absorbed. For a monoenergetic  $\gamma$  ray the result is a delta function at  $E=h\nu-m_oc^2$ .

Altogether, pair production, Compton scattering, and the photoelectric effect produce the characteristic form of the detector response to  $\gamma$  rays. As shown in the idealized detector response to a 2 MeV  $\gamma$  ray in Figure 4.5, there is a photopeak at 2 MeV consisting of the  $\gamma$  rays that deposit all of their energy into the detector through any of these interactions with the rest of the spectrum formed by  $\gamma$  rays that deposit only a portion of their energy. The most likely process of partial energy deposition is for a  $\gamma$  to Compton scatter out of the detector. Therefore, on the low-energy side of the photopeak is a gap of width  $\Delta E_C$  produced by a lack of Compton-scattered  $\gamma$  rays followed by the Compton edge. The gap contains some events due to single photons undergoing multiple Compton-scattering interactions. The Compton continuum continues from the Compton edge down to low energies where the backscatter peak is formed. The backscatter peak is created by  $\gamma$  rays that have undergone a head-on collision in another material and scattered back into the detector, producing a peak at  $E \approx E_C$ . Finally, there is the possibility of

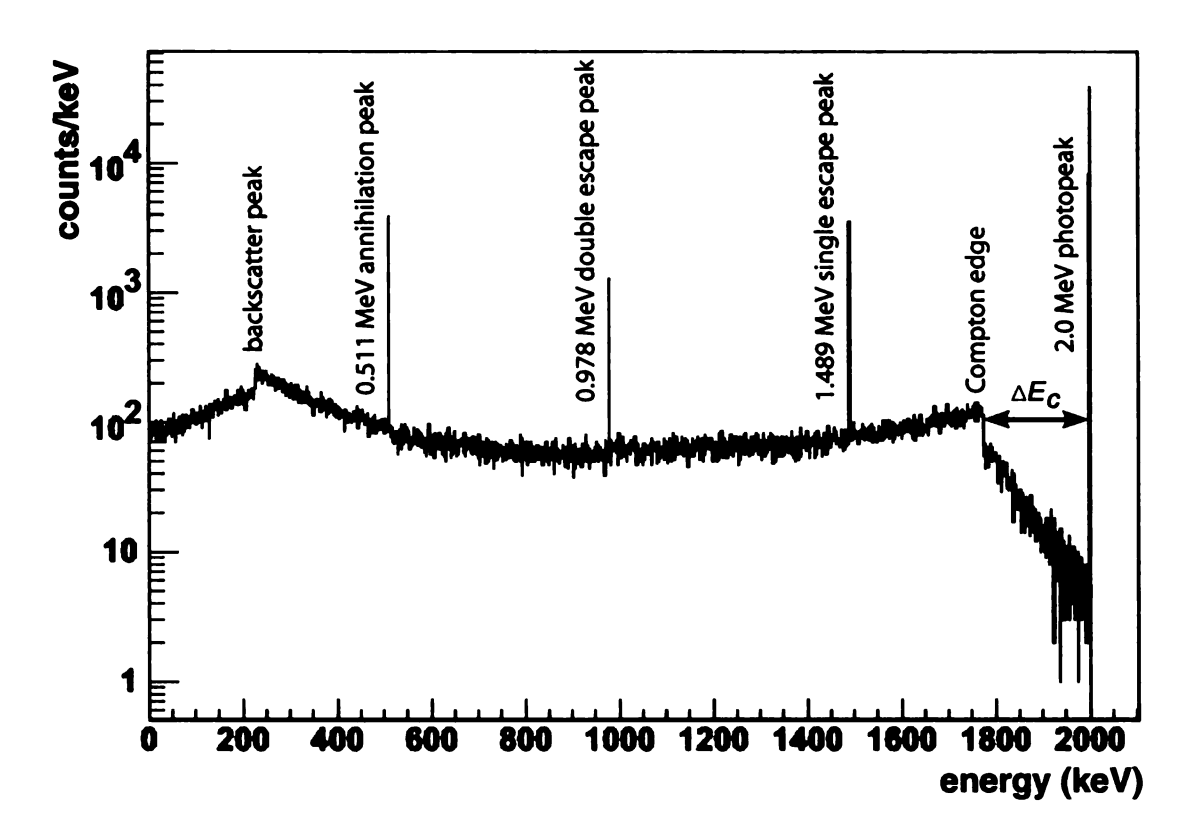


Figure 4.5: The idealized detector response to 2 MeV  $\gamma$  rays showing the photopeak, Compton edge, single- and double-escape peaks, annihilation peak, and the backscatter peak. In the idealized case, all interactions except Compton scattering result in delta functions.

pair production. Pair production that occurs inside the detector most likely leads to annihilation and absorption of the energy by the detector. However, a portion of the annihilation photons escape the detector, causing a single-escape peak to form at  $E = h\nu' - m_0c^2$  and double-escape peak at  $E = h\nu' - 2m_0c^2$ . Finally, pair production may occur in surrounding materials, and annihilation photons will produce a delta function at  $E = m_0c^2$ . While the principles discussed here for the ideal case form the basis of the actual output of the detector, there are significant differences as described in the following section.

## 4.4 Detector and electronics modeling

Once energy has been deposited, the simulation treats the detectors as described in Section 3.3. The  $\gamma$  ray deposits energy in a few locations, which are individually converted into scintillation photons that are attenuated towards the ends of the bar. The number of scintillation photons  $N_{ph}$  produced depends on the energy deposited  $E_{dep}$ , the efficiency of the scintillation process ( $\epsilon_{scint} = 12\%$  for NaI), and the energy of the scintillation photons (the average is  $\overline{h\nu}_{ph} = 3$  eV).

$$N_{ph} = \frac{E_{dep} \epsilon_{scint}}{\overline{h \nu}_{ph}} \tag{4.12}$$

While the attenuation accounts for the gross process moving away from the location of the interaction, there is a local effect that must be included: some of the photons will never move along the length of the bar. Due to the complexity of determining what portion of light would be transmitted for every location in the bar, a simplified model is implemented. The angle of incidence  $\psi_{crit}$  for total internal reflection for NaI(Tl) is

$$\psi_{crit} = \arcsin\left(\frac{n_{vac}}{n_{NaI}}\right) = 32.7^{\circ} \tag{4.13}$$

where  $n_{vac} = 1$  and  $n_{NaI} = 1.85$  are the indices of refraction. By examining Figure 4.6, one notices that the range of total internal reflection,  $\psi = (\psi_{crit}, 90^{\circ})$ , is equivalent to the emission angle range  $\theta = (0^{\circ}, 90^{\circ} - \psi_{crit})$ . Thus, the portion of scintillation photons traveling in each direction that survive the first interaction with the scintillator wall is approximately

$$f = 1 - \sin \psi_{crit} \approx 46\%. \tag{4.14}$$

Finally, the scintillation photons are attenuated to the ends of the bar. Due to the geometry of the detector, only T=27% of the photons pass through the

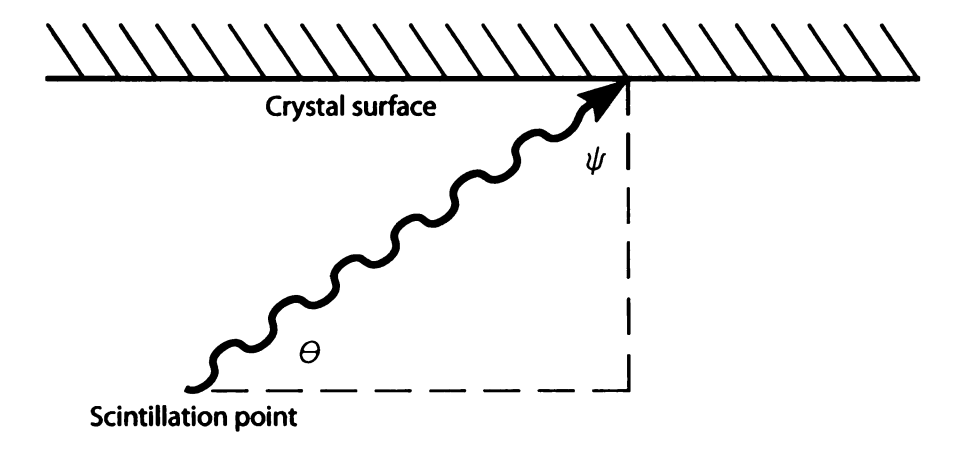




Figure 4.6: The relationship between the angle of incidence  $\psi$  to the crystal surface and the angle of emission  $\theta$  from the scintillation point.

quartz window and into the PMT, which has a quantum efficiency of 20% at the wavelength emitted by NaI(Tl). At this point, an additional factor of k = 0.88is applied to the number of photoelectrons to account for the simplicity of the model, e.g. the angular range cutoff and the transmission through the window, and the use of fixed values for integrated quantities, e.g the quantum efficiency. The method of determining the value of k is described below.

As an example, a 1 MeV  $\gamma$  ray may deposit 700 keV at z=10 cm and 300 keV at z = 8 cm. The numbers of scintillation photons  $N_i$  that reach the end of each bar are

$$N_{1} = \frac{E_{dep,j} \epsilon_{scint} f}{2h\nu_{ph}} e^{-\mu(L/2+z_{j})} = 1668$$

$$N_{2} = \frac{E_{dep,j} \epsilon_{scint} f}{2h\nu_{ph}} e^{-\mu(L/2-z_{j})} = 4036,$$
(4.15)

$$N_2 = \frac{E_{dep,j} \epsilon_{scint} f}{2\overline{h\nu}_{ph}} e^{-\mu(L/2 - z_j)} = 4036,$$
 (4.16)

where the index j has been summed over the two interactions. After passing through the windows and into the PMTs, the numbers of photoelectrons produced in the PMTs are

$$N_{PE,1} = T\epsilon_{quant}kN_1 = 79 (4.17)$$

$$N_{PE,2} = T\epsilon_{quant}kN_2 = 192. \tag{4.18}$$

The number of photoelectrons in the first stage of the PMT is the point of minimum statistics for the system. Statistical fluctuations are factored in by sampling Poisson distributions with mean  $N_{PE,i}$ . For this example, let  $N_{PE,1} = 90$  and  $N_{PE,2} = 171$ .

The  $N_{PE,i}$  are now used to reconstruct the position and energy of the  $\gamma$  ray. The reconstructed position is given by

$$z_{rec} = \frac{1}{2\mu} \ln \frac{N_{PE,1}}{N_{PE,1}} = 9.4 \text{ cm.}$$
 (4.19)

with the coefficient of linear attenuation  $\mu = 0.047/\text{cm}$ . The energy is

$$E_{rec} = g\sqrt{N_{PE,1}N_{PE,2}} = 976 \text{ keV}.$$
 (4.20)

The scaling factor g is determined by fitting the centroid of the simulated photopeak and mapping it to the  $\gamma$  ray energy. The reduction factor k given above was determined by matching the photopeak width of the simulation to that of the data. In this manner, the energy and position spectra of the 1836 keV  $\gamma$  ray in  $^{88}$ Y are reproduced.

The energy threshold has an effect on the detector response at lower energies as discussed in Section 3.3.4. The threshold is modeled by reconstructing the discriminator voltages for each PMT signal. These voltages are scaled by a gain factor  $g_{th}$  that converts the physical voltage to the proper value when applied to the simulation's PMT output. Because the amplifier's fast timing output has a short shaping

time, the signal entering the discriminator has a large variation in amplitude. This variation in the amplitude of the input to the discriminator is represented in the simulation by a variation in the amplitude of the threshold. Each detector has a fixed mean threshold; each simulated event samples a normal distribution about the mean to determine if an effective threshold has been exceeded and the event accepted. The gain factor and threshold width were determined by the process of  $\chi^2$  minimization of the simulated response function to the position spectrum of the 898 keV  $\gamma$  ray. Because the spectrum is an energy-gated position spectrum, both the energy and position response of APEX are reproduced by the  $\chi^2$  minimization.

Continuing the example from above, the simulated mean thresholds in this bar may be  $E_{th,1} = 159$  and  $E_{th,2} = 123$ . Although  $N_{PE,2} > E_{th,2}$ , the discriminator may or may not trigger due to the statistical nature of the process. Following the configuration of the APEX electronics, if either threshold on a bar is exceeded, the data are recorded from both PMT channels. The final result of the APEX simulation is shown in Figure 4.7. The isotropic position response of the 1836 keV  $\gamma$  ray is reproduced, as well as the threshold-influenced response of the 898 keV  $\gamma$  ray. The energy response is shown in Figure 4.8. The disparity in the position response between the simulation and the data is due to the breakdown of the exponential attenuation at the ends of the detector. By rejecting the ends of the bars, the difference in the 898 keV peak area in the simulation and data are reduced to 1% compared to the 7% difference shown here. However, the  $\gamma$ -rays from excited beam projectiles are forward focused, and the efficiency in the center of the array is reduced due to the threshold. The significance of this discrepancy may be gauged by plotting the positions of those events that fall within a gate on the <sup>76</sup>Ge photopeak shown in Figure 4.9 and those events within an equalwidth gate on the high-energy side of the photopeak. The difference between the two histograms is representative of the interaction position of photopeak  $\gamma$  rays.

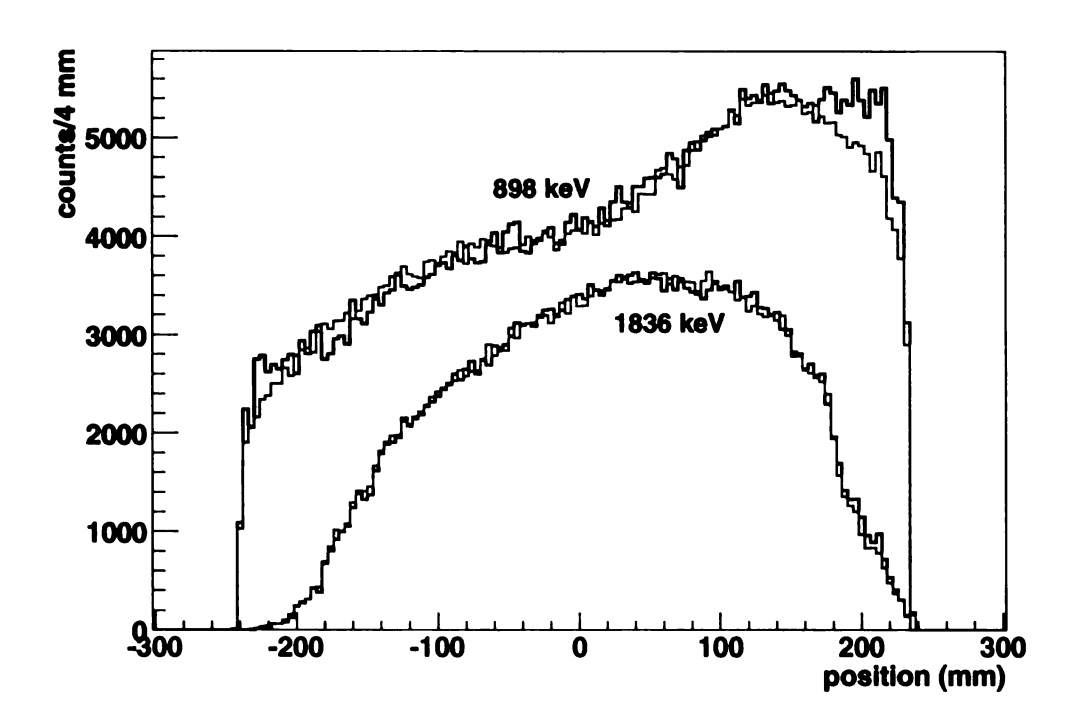


Figure 4.7: The position response of APEX for an  $^{88}$ Y  $\gamma$ -ray source placed at 6 cm. The 1836 keV  $\gamma$  ray (lower) and 898 keV  $\gamma$  ray (upper) data are shown in black and the simulation in grey.

Figure 4.10 indicates that the photopeak events mostly lie in the region where the simulation and data diverge. It is for this reason that the simulation is used to determine a peak shape and the efficiency is established relative to the previously measured transition rate of <sup>52</sup>Ti.

The maximum laboratory-frame scattering angle encountered in this experiment is  $3.06^{\circ}$  for  $^{52}$ Ti. The acceptance of the S800 is 20 msr formed in an approximately ellipsoid shape of  $7^{\circ}$  in the dispersive direction and  $10^{\circ}$  in the nondispersive direction. Moving the target upstream from the position of optimal acceptance to the S800 would increase the proportion of  $\gamma$ -rays emitted within the angular range subtended by APEX. However, the beamline magnets were known to be misaligned during this experiment, resulting in a reduction of the nondispersive acceptance. A measurement of the acceptance of the S800 is prerequisite to determining an upstream target position, and the measurement in turn requires that a scattering

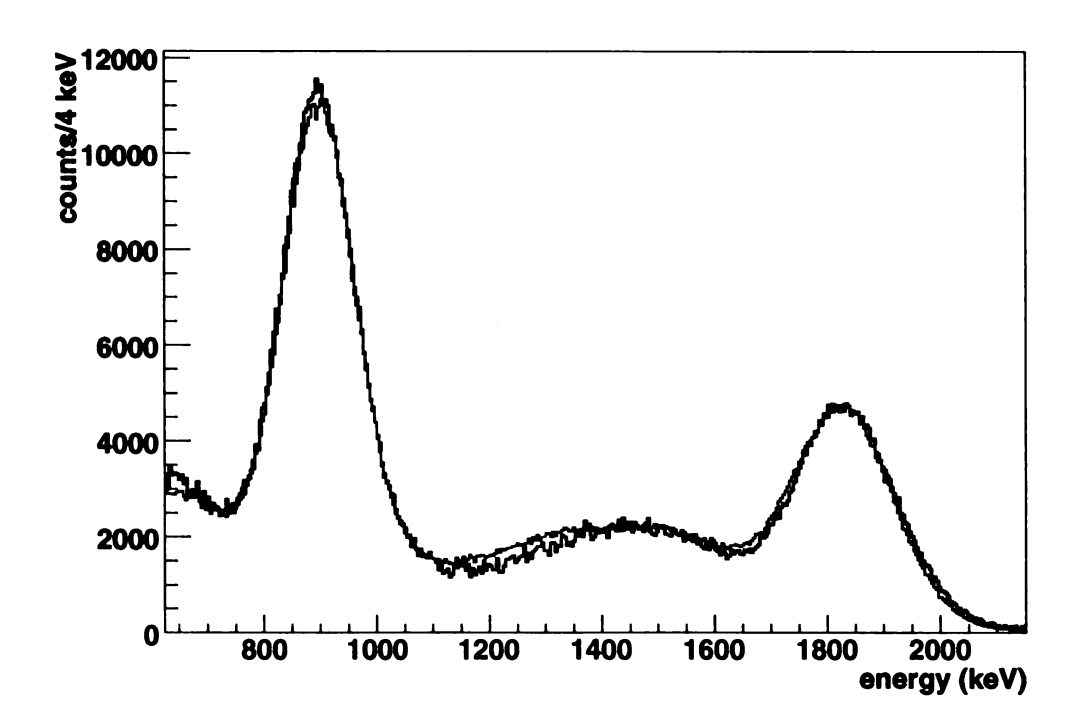


Figure 4.8: The energy response of APEX for an  $^{88}$ Y  $\gamma$ -ray source placed at 6 cm. The data is shown in black and the simulation in grey.

chamber be installed at the target position rather than APEX. Ultimately, the misalignment was not quantified but merely fixed soon after the experiment. It is possible to have positioned the target with trial and error, a time-consuming process subject to the limitation of determining an acceptance cutoff in the low statistics of the affected larger scattering angles.

The goal of the simulation is to produce response functions for fitting to a  $\gamma$ -ray spectrum from a Coulomb excitation reaction. The primary beam of an experiment can be directed into the experimental area with high intensity and little cost in time. The primary beam for this experiment, <sup>76</sup>Ge, was Coulomb excited on a <sup>209</sup>Bi target with a speed of  $\beta = 0.396$  at midtarget to furnish a test of the simulated  $\gamma$ -ray energy peak shape of projectile Coulomb excitation. This test measurement was made in six hours in contrast with the two days required for the <sup>50</sup>Ca measurement. The results of this response function fit to the data with

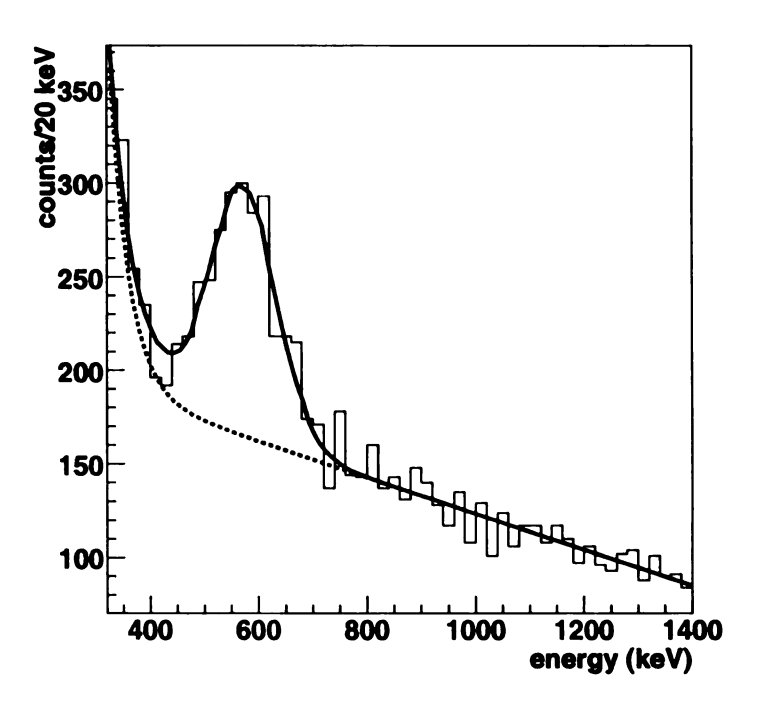


Figure 4.9: The Coulomb excitation energy spectrum of  $^{76}$ Ge traveling at  $\beta = 0.396$  with a fit of the response function (thick, solid line) with a continuum background (thick, dashed line).

an exponential plus a constant background is shown in Figure 4.9. Fitting the same data with a Gaussian function rather than the response function produces a width 6% larger and an area 10% larger; the minimization, however, results in a  $\chi^2$  two orders of magnitude larger. Apparently, the constrained width and Compton continuum of the response function are necessary facets of the fitting function.

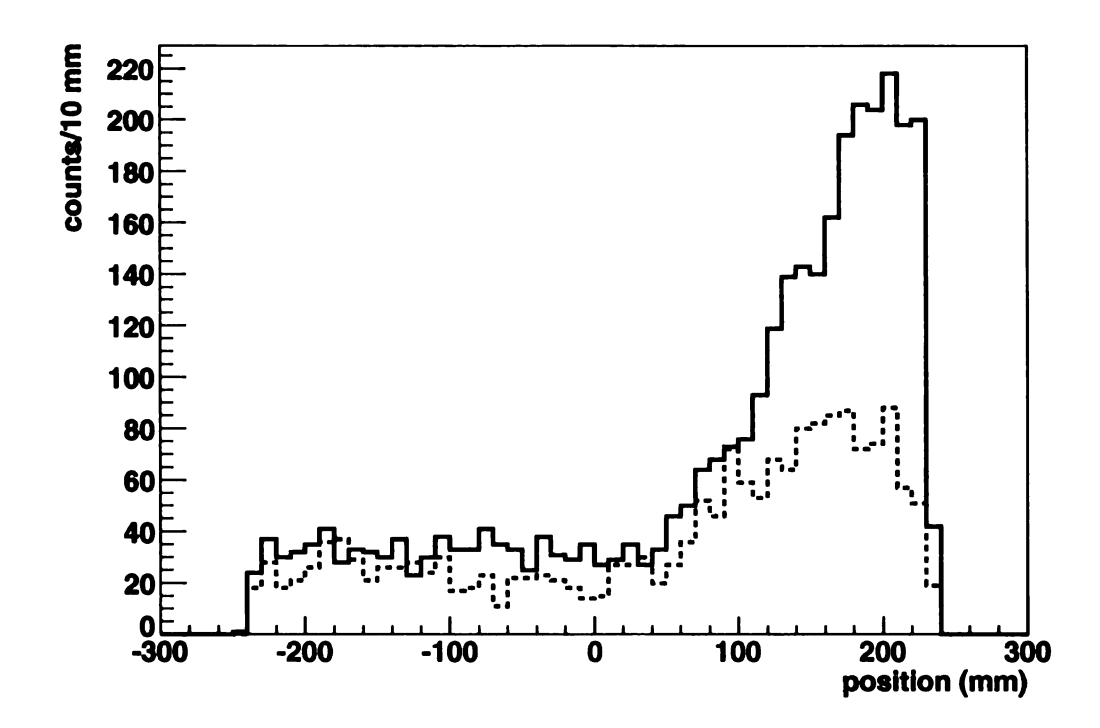


Figure 4.10: The position response of the events contained in a gate on the <sup>76</sup>Ge photopeak of Figure 4.9 (solid) compared to those of an equal-width gate placed on the high energy side of the photopeak (dashed). The difference in the two histograms is representative of the position response of photopeak events, which lie mostly in the region where the simulation diverges from the data.

## Chapter 5

# Data analysis and experimental results

With the experimental apparatus described and the response of APEX simulated, the process of extracting the neutron effective charge is now demonstrated. Due to the divergence between the simulated position response of APEX and the data near the ends of the bars, the  $B(E2;0_1^+ \rightarrow 2_1^+)$  of  $^{52}$ Ti is used to determine the efficiency of APEX. The  $B(E2;0_1^+ \rightarrow 2_1^+)$  of  $^{50}$ Ca is then found, and a neutron effective charge is calculated. First, the  $^{52}$ Ti nuclei are distinguished from the beam contaminants in the focal plane of the S800 Spectrograph. The particle identification includes corrections for measurement effects such as variations in the flight paths of the beam nuclei to better separate the isotopes. By selecting the  $\gamma$  rays that are time-correlated with the scattered  $^{52}$ Ti nuclei, the random  $\gamma$ -ray background is minimized. To avoid the possibility of nuclear excitations, only  $\gamma$  rays emitted by nuclei that are scattered by less than a maximum angle related to a minimum impact parameter will be accepted, and, to reduce the beam-correlated background, the  $\gamma$  rays from nuclei that are scattered at very small angles, i.e. the interactions with large impact parameters, will be rejected. With this selection

of events, the  $\gamma$  rays are used to tag the Coulomb excited nuclei and thereby measure the Coulomb excitation cross section of  $^{52}\mathrm{Ti}$ . Using the intermediate-energy Coulomb excitation theory of Alder and Winther[34], the  $B(E2;0_1^+\to 2_1^+)$  of  $^{52}\mathrm{Ti}$  is deduced from the angle-integrated Coulomb excitation cross section. The transition rate is compared to a previous measurement to find the efficiency of APEX. Next, using the same method described for  $^{52}\mathrm{Ti}$ , the  $\gamma$ -ray cross section of  $^{50}\mathrm{Ca}$  is extracted from the data. Feeding of the  $2_1^+$  state from excitations to higher-lying states is inferred to be small from shell-model considerations. The  $B(E2;0_1^+\to 2_1^+)$  is deduced, and the similarity in the reaction kinematics and  $\gamma$ -ray distribution and energy of  $^{52}\mathrm{Ti}$  and  $^{50}\mathrm{Ca}$  permit the efficiency determined from the  $^{52}\mathrm{Ti}$  reaction to be applied to the  $^{50}\mathrm{Ca}$  case. Comparing the transition rate of  $^{50}\mathrm{Ca}$  to that predicted by the GXPF1A effective interaction leads to a value of the neutron effective charge.

## 5.1 ${}^{52}\text{Ti }B(E2;0_1^+\to 2_1^+)$ measurement

The efficiency for the  $^{50}$ Ca cross section measurement will be determined in this section through the measurement of the  $B(E2;0_1^+ \to 2_1^+)$  of  $^{52}$ Ti. The particle identification procedure will be examined, and corrections to the particle identification spectrum will be detailed. The software gates on the APEX times and the projectile scattering angle will be demonstrated to produce a reduced-background  $\gamma$ -ray energy spectrum of  $^{52}$ Ti. A simulated response function will be fit to the energy spectrum, and a cross section determined. The observed  $B(E2;0_1^+ \to 2_1^+)$  of  $^{52}$ Ti will be deduced. From comparison to a previous measurement, the efficiency will be found.

#### 5.1.1 Particle identification

The procedure for identifying isotopes in the A1900 is described in Section 3.1. From the A1900, the beam is directed onto the secondary target at the target position of the S800. From the magnetic rigidity of the S800 Analysis Line and a calculation of the energy loss of the beam in the target using the program LISE[61]. the magnetic rigidity of the S800 Spectrograph magnets is selected to guide the elastically-scattered and Coulomb-excited nuclei to the focal plane. In this experiment, the <sup>52</sup>Ti arrived on target as a member of a beam cocktail and was identified in the focal plane of the S800 Spectrograph. The  $\Delta E$ -tof spectrum of the <sup>52</sup>Ti beam is shown in Figure 5.1. On the horizontal axis is the time of flight between the S800 Object scintillator and the S800 Focal Plane scintillator, and on the vertical axis is the energy loss in the focal plane ion chamber. The relative intensities and positions of the loci are compared to the particle identification histogram from the focal plane of the A1900 to identify the nuclei. The <sup>52</sup>Ti locus is indicated in the figure along with the primary contaminant, <sup>53</sup>V. The <sup>52</sup>Ti beam reached the focal plane with 66% purity, and 5.5 hours of data were collected at an average total beam rate of  $3.6 \times 10^3$  pps.

In this experiment, the limited beam rate requires that the focus mode of the S800 be used. The momentum spread at the focal plane causes a broadening of the loci in the particle identification spectrum, which can be reduced by the introduction of corrections for beam-parameter correlations. For example, by sweeping out a larger arc in the S800 dipoles, a high-momentum particle will enter the focal plane at a different position than a low-momentum particle of the same species. Since the time of flight between the S800 Object and Focal Plane depends on the path taken by the projectile, a correlation is formed between the time of flight and the dispersive position in the focal plane. Similarly, a particle entering the

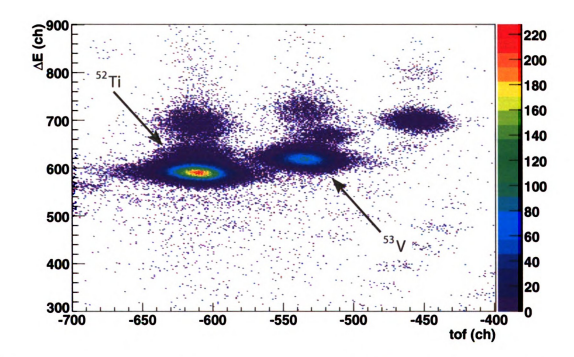


Figure 5.1: The particle identification spectrum with  $^{52}$ Ti and the other primary constituent  $^{53}$ V indicated. Corrections for beam parameter dependencies have not been implemented. Compare with Figure 5.5, which does have the dependencies removed.

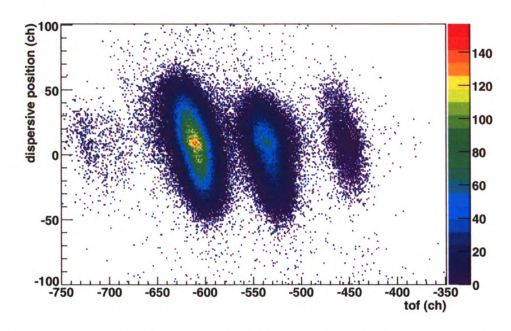


Figure 5.2: The correlation between the position at CRDC1 in the S800 focal plane and the time of flight. A linear correction is applied to the time of flight to improve the particle-identification spectrum.

S800 at a larger angle from the beam direction will travel further than a particle entering at a smaller angle, also leading to a correlation between the time of flight and the angle in the focal plane. The correlation between the time of flight and the dispersive position in the first CRDC is illustrated in Figure 5.2, and the correlation between the time of flight and the angle in the focal plane can be seen in Figure 5.3. The dependency of time of flight on the dispersive position and angle in the focal place is removed by introducing linear corrections. The corrected time of flight is

$$t_{corr} = t_{fp-obj} - a_x x_{CRDC1} - a_\theta \theta_{fp}$$
 (5.1)

where  $x_{\text{CRDC1}}$  is the dispersive position on CRDC1 and  $t_{fp-obj}$  is the time of flight between the S800 Object and Focal Plane. The factors  $a_x$  and  $a_\theta$  are their respective corrections.

In these data and in data collected during previous experiments using the S800.

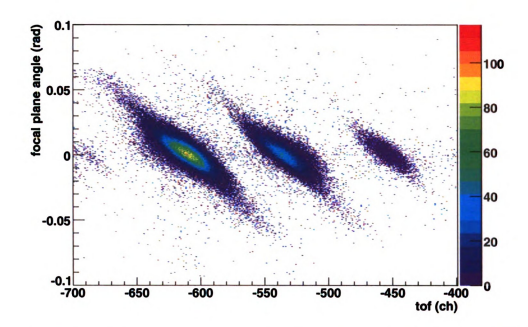


Figure 5.3: The correlation between the angle in the S800 focal plane and the time of flight. A linear correction is applied to the time of flight to improve the particle-identification spectrum.

the energy loss in the focal place ion chamber is dependent on the dispersive position as shown in Figure 5.4. The origin of this dependency is not known, and a phenomenological correction is applied to remove the dependency. The correction takes the form

$$\Delta E_{corr} = \begin{cases} \Delta E e^{b(x_0 - x)} & x < x_0 \\ \Delta E & x > x_0 \end{cases}$$
 (5.2)

with  $\Delta E$  the measured energy loss in the ion chamber and  $x_0$  and b chosen to make  $\Delta E_{corr}$  constant in the dispersive direction x at CRDC1.

The  $\Delta E$ -tof spectrum of the  $^{52}\mathrm{Ti}$  beam with beam parameter corrections is shown in Figure 5.5. The reduced width of the loci relative to the uncorrected particle identification is noticeable for this  $\Delta p/p=0.5\%$  beam and will be much more significant in the case of  $^{50}\mathrm{Ca}$  due to the larger 3% momentum width. A software gate is placed on the  $^{52}\mathrm{Ti}$  locus in the corrected spectrum to select the

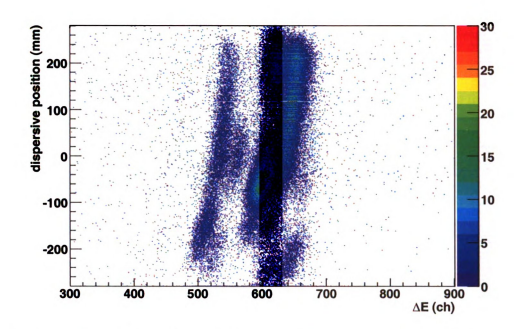


Figure 5.4: A histogram showing the dependence of the ion chamber,  $\Delta E$ , on the dispersive position, x. A phenomenological correction is applied to make  $\Delta E$  constant in x. The data shown here is from the  $^{50}\mathrm{Ca}$  beam, where the effect is more pronounced.

particle-correlated  $\gamma$ -ray events.

#### 5.1.2 $\gamma$ -ray spectrum

The immediate goal is to extract the spectrum of the  $^{52}$ Ti  $^{+}_{1} \rightarrow 0^{+}_{1}$  transition at 1050 keV from the background radiation. Due to the equiprobable emission of  $\gamma$  rays axially from the beam direction, the  $\gamma$ -ray energy spectra of the individual APEX bars can be summed into one histogram, and all APEX energy histograms shown in this work are summed. Three detectors were not functioning during the course of this experiment and are not included in the analysis. The photopeak is expected to contain a few hundred counts spread over approximately 180 keV FWHM. Since APEX counts at over 4 kHz on room background, the background radiation must be minimized so as not to overwhelm the photopeak.

With the  $^{52}\mathrm{Ti}$  particle identification gate applied, the  $\gamma\text{-ray}$  energy spectrum

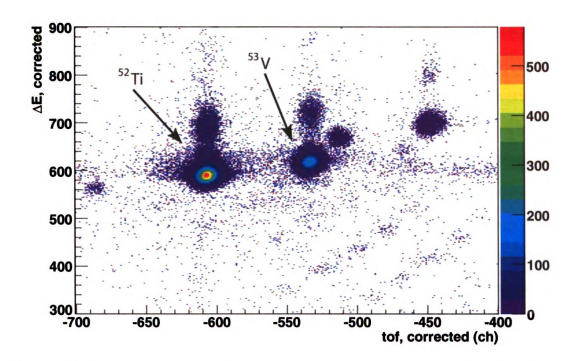


Figure 5.5: The corrected particle identification spectrum with  $^{52}{\rm Ti}$  and the other primary constituent  $^{53}{\rm V}$  indicated.

contains only those event that included a  $\gamma$ -ray trigger within the 200 ns width of the particle- $\gamma$  coincidence gate (see Section 3.3 for timing details). With  $4.4\times10^7$  52Ti nuclei in 5.5 hours, the coincidence gate was open for 8.8 s, or 0.044% of the total data collection time. Further, a  $\gamma$  ray was not detected in coincidence with all projectiles, and multiple  $\gamma$  rays up to the number of active detector bars can be recorded for each particle event during the longer ADC gate; however, the  $4.5\times10^5$  particle- $\gamma$  coincidence triggers with a 1.7  $\mu$ s ADC gate leads to an open gate on each of the 21 ADCs  $3.8\times10^{-3}\%$  of the total collection time. Random background is significant only to this small factor.

In addition to the room background, the energy spectrum contains beamcorrelated background that can be distinguished from the promptly emitted  $\gamma$ rays in the time spectrum of each PMT channel. This time spectrum is the difference between the detection of a projectile in the S800 and the detection of a  $\gamma$  ray in APEX. Since the rise time of NaI(Tl) is less than 5 ns, the  $\gamma$  rays emitted promptly upon the occasion of a  $^{52}$ Ti nucleus passing through the target will produce a timing peak within the 200 ns coincidence gate. The time spectrum for a single PMT channel is shown in Figure 5.6. On the left side of the spectrum are the random background events, and in the center is a Gaussian peak of prompt  $\gamma$  rays. Extending to the right are beam-correlated background events, such as from target breakup and the creation of short-lived isotopes in the beam pipe. A software gate is placed on the prompt  $\gamma$ -ray events so that off-prompt  $\gamma$  rays are omitted from the energy spectrum. Since the thresholds effect discussed in Section 3.3 prevent a large portion of  $\gamma$ -rays from simultaneously surpassing the threshold in both channels of a detector bar, the gates on the two time spectra are combined with a logic OR to form the time gate of the detector. The detector time gate is applied to each detector bar individually.

The final gate is placed on the scattering angle of the projectile with two purposes, to minimize background like the previous gates and to avoid nuclear contributions to the excitation. The Rutherford-like cross section of the laboratory scattering angle of  $^{52}$ Ti is histogrammed in Figure 5.7. A gate is placed to reject nuclei scattering at large angles to avoid those reactions with small impact parameters where nuclear excitations are possible. The maximum scattering angle shown in Figure 5.7 corresponds to the minimum impact parameter  $b_{min} = 13.5$  fm as related by Equation 2.14. The rejection of small angles is due to the fact that Coulomb excitation is more probable for smaller impact parameters (larger scattering angles) while elastic scattering favors small scattering angles; therefore, removing the very forward scattered nuclei reduces the background by a large amount while removing a smaller proportion of the angle-integrated Coulomb excitation cross section. The effect of this minimum angle gate is demonstrated in Figure 5.8. The shaded histogram is the energy spectrum of  $^{52}$ Ti with time gates

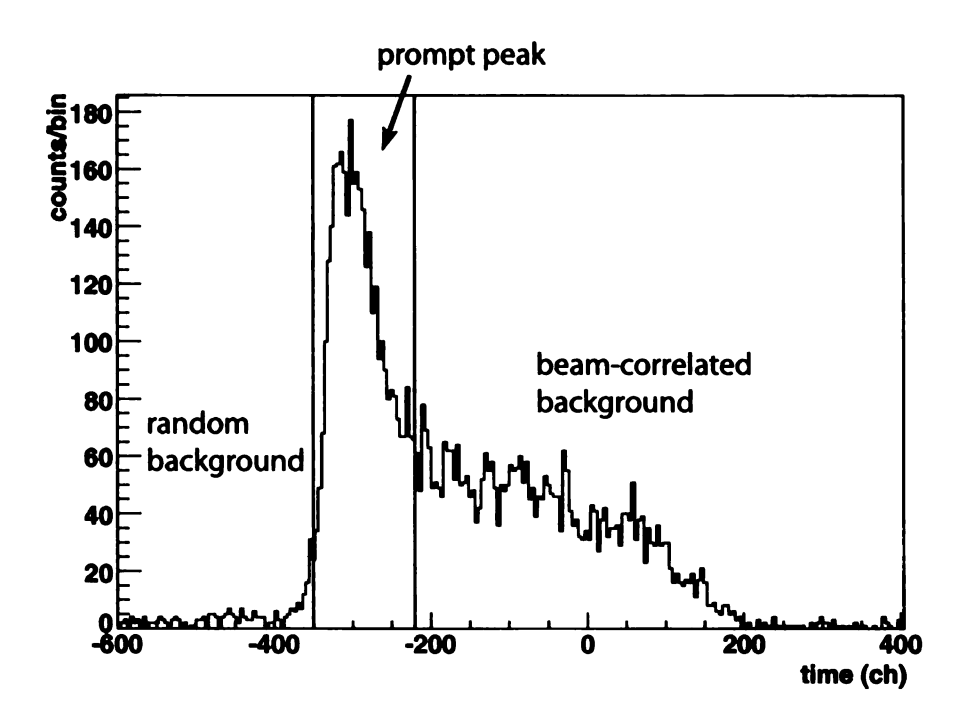


Figure 5.6: The time spectrum of a single APEX PMT. This spectrum shows the difference in time between the detection of a beam projectile within the  $^{52}$ Ti gate by the S800 and the detection of a  $\gamma$  ray by APEX. The low random background can seen on the left side of the spectrum. The  $\gamma$  rays promptly emitted after the nuclei pass through the target form a Gaussian peak in the center of the spectrum, and the beam-correlated background continues to the right. One channel is 227 ps.

and a scattering angle range of  $[0, \theta_{min})$ , and the solid line histogram is the energy spectrum of  $^{52}$ Ti with time gates and an angle range of  $[\theta_{min}, \theta_{max})$  as shown in Figure 5.7. The  $2_1^+ \to 0_1^+ \gamma$ -ray photopeak at 1050 keV is visible in the latter case and is not in the former. The analysis of the  $^{50}$ Ca data shares a selection of this same impact parameter range; therefore, the minimum impact parameter is selected to not exceed the nuclear interaction radius of both nuclei, and the maximum,  $b_{max} = 40.0$  fm, is chosen to optimize the peak-to-background ratio of the two  $\gamma$ -ray energy spectra.

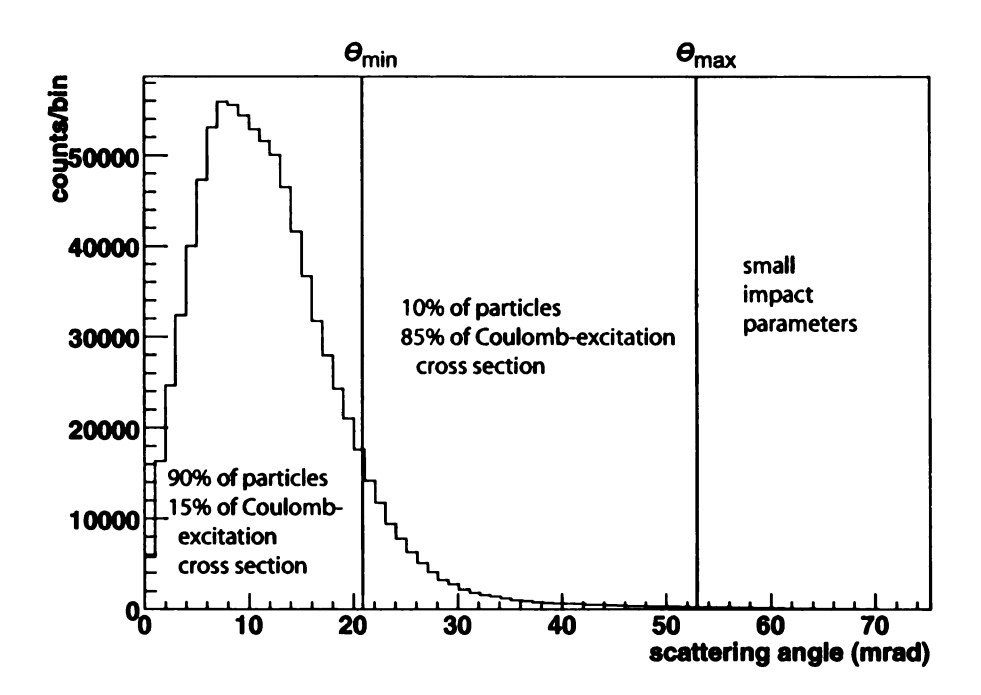


Figure 5.7: The scattering angle of  $^{52}$ Ti nuclei with the maximum and minimum scattering angles indicated. The relative cross section for each section demonstrates that the signal-to-noise ratio is improved within the angle range  $[\theta_{min}, \theta_{max})$ .

#### 5.1.3 Cross section

The  $\gamma$  rays tag the Coulomb excited nuclei to determine the excitation cross section. The number of  $\gamma$  rays observed is determined by fitting the energy spectrum generated by the gates discussed in the previous section with a simulated response function. Lacking the knowledge of the efficiency of APEX due to the divergence between the simulated position response and the data, the observed cross section and the associated uncertainty will be calculated.

The simulated response function is created as described in Chapter 4. The threshold parameters are determined though the  $\chi^2$  minimization to an <sup>88</sup>Y source measurement taken just after the in-beam measurement. The decay lifetime is known from a previous intermediate-energy Coulomb excitation measurement by Dinca *et al.* (see the next section for details). The position of emission along the beamline is shown in Figure 4.3. The midtarget velocity  $\beta_{mid}$  and the after-target

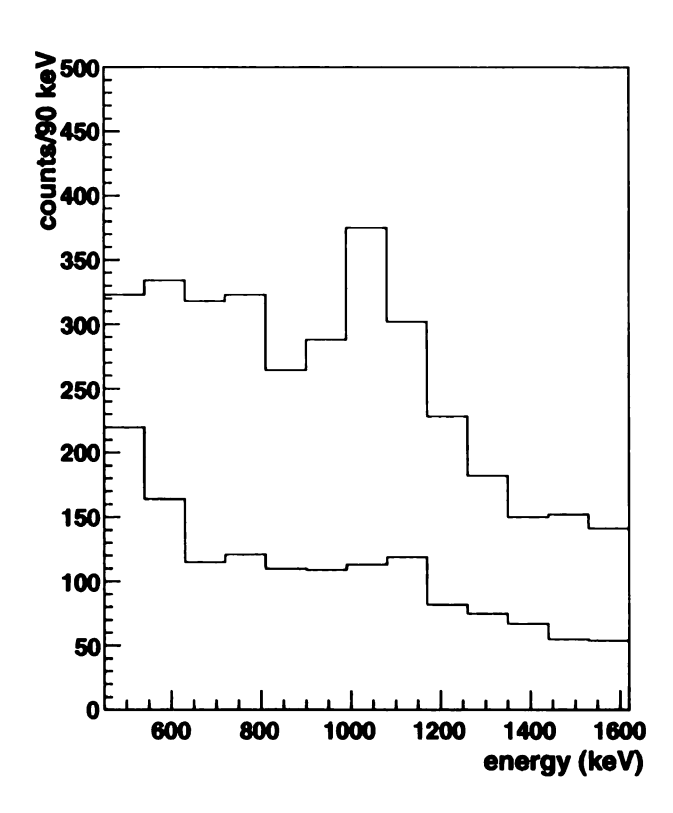


Figure 5.8: The  $\gamma$ -ray energy spectrum for  $^{52}$ Ti with time gates applied. The shaded histogram includes the scattering angle range  $[0, \theta_{min})$ , and the black line histogram includes the range  $[\theta_{min}, \theta_{max})$ . Although the shaded histogram included 90% of the scattered  $^{52}$ Ti nuclei, no photopeak presents itself clearly above the background. The peak-to-background ratio can be improved by removing these very forward scattered nuclei, leaving the unshaded histogram.

velocity  $\beta_{post}$  are calculated from the magnetic rigidity of the beamline magnets and the thickness of the target, 184 mg/cm<sup>2</sup> nat Au. The majority of the  $\gamma$  rays are emitted outside of the target, and  $\beta_{post}$  is used for Doppler reconstruction.

The response function generated by the GEANT4 simulation for the  $2_1^+ \rightarrow 0_1^+$  transition and a continuum background is fit to the  $\gamma$ -ray energy spectrum of  $^{52}$ Ti. The continuum is an exponential plus a constant and is allowed to vary with the fit. Figure 5.9 displays the  $\gamma$ -ray spectrum with the continuum as a thick, dashed line and the fit drawn as a thick, black line. The number of  $\gamma$  rays observed is

$$N_{\gamma_{obs}} = \frac{A_{fit}}{l_{coinc}} \tag{5.3}$$

with  $A_{fit}$  as the amplitude of the fit and  $l_{coinc}$  as the livetime for the coincidence trigger. The number of  $^{52}$ Ti nuclei  $N_B$  is similarly scaled by the livetime of the particle trigger. With the number density  $N_T$  of the target known, the efficiency of APEX is the remaining factor required to calculate the cross section from Equation 2.13. Instead, the observed cross section will be defined as

$$\sigma_{i \to f_{obs}} = \frac{N_{\gamma, f \to i}}{N_T N_R} \tag{5.4}$$

and the efficiency will be addressed in the following section. Since the  $2_1^+$  state decays through  $\gamma$  emission, the number of emitted  $\gamma$  rays is equivalent to the number of excitations. No feeding was observed in Dinca's measurement of the  $B(E2;0_1^+ \rightarrow 2_1^+)$  of  $^{52}$ Ti, and none is assumed here. The resulting cross section is 98(17) mb. Poisson statistics for  $N_B$  and livetimes provide a small uncertainty contribution. The major contributions to the uncertainty are the fit (13%) and the simulated response function (10%). The fit uncertainty is taken from the covariance matrix for the fit parameters and the data. The uncertainty in the

response function originates in the simulation parameters. The placement of the target was varied by 0.5 cm, a sufficiently large distance to be just noticeable in the position response of APEX, to find an uncertainty of 3%. The simulated threshold parameters are estimated to contribute 8% to the uncertainty. The threshold settings for the <sup>50</sup>Ca beam are different from those of the <sup>52</sup>Ti beam to reduce deadtime, and the uncertainty is the difference in efficiency between the two threshold settings coupled with the difference between the the optimal simulated energy response and the amplitude of the 898 keV peak in <sup>88</sup>Y. The simulated threshold amplitude strongly affects the response function, with the diffusiveness contributing to a lesser degree.

#### 5.1.4 In-beam efficiency

The observed transition rate is calculated using the theory of Alder and Winther[34], and the efficiency of APEX is determined by comparing the observed transition rate of  $^{52}$ Ti to a previously measured value[20]. The Alder and Winther formulation of the theory of intermediate-energy Coulomb excitation is introduced in Section 2.4.2. The observed transition rate of  $^{52}$ Ti is deduced to be  $B(E2; 0_1^+ \rightarrow 2_1^+) = 382.6(65.9) \text{ e}^2\text{fm}^4$ . The conversion of the angle-integrated cross section to the transition rate depends on the the angular range over which the integration occurs, and the uncertainty in the scattering angle ( $\delta\theta = 0.5^{\circ}$ ) is added in quadrature to the cross-section uncertainty to form the total transition rate uncertainty.

The  $B(E2;0_1^+\to 2_1^+)$  of  $^{52}$ Ti has previously been measured by Dinca *et al.* using intermediate-energy Coulomb excitation with the Segmented Germanium Array at the NSCL[20]. SeGA has been used many times for transition rate studies with success as demonstrated not only by Dinca's measurement of the  $B(E2;0_1^+\to 2_1^+)$  of the high-intensity, stable  $^{76}$ Ge beam shown in Figure 2.9a but

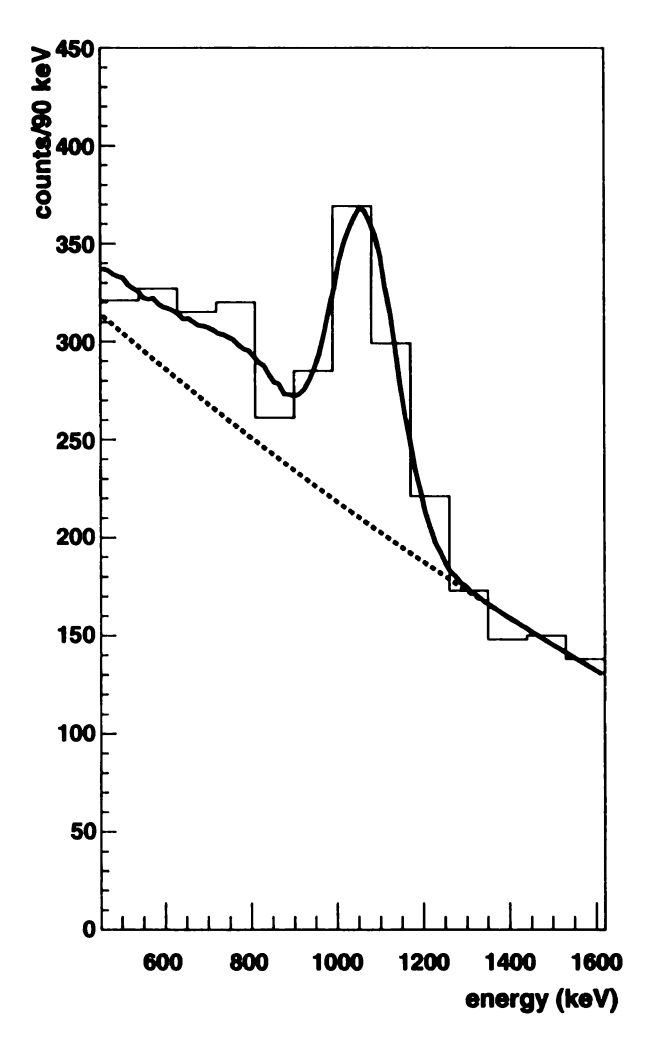


Figure 5.9: Fit of the response function plus continuum background to the  $^{52}$ Ti  $\gamma$ -ray spectrum. The fit is the thick, black line and the continuum is dashed.

nat Au target	184	$mg/cm^2$
$oldsymbol{eta}$	0.364	_,
$N_{m{\gamma}}$	2279 (303)	
$E(2_1^+)$	1033 (78)	keV
$\sigma_{obs}$	98 (17)	mb
$B(E2; 0_1^+ \rightarrow 2_1^+)_{obs}$	383 (69)	${ m e^2 fm^4}$
$\sigma_{obs} \ B(E2; 0_1^+ \to 2_1^+)_{obs} \ B(E2; 0_1^+ \to 2_1^+)_{Dinca}$	567 (51)	$\mathrm{e^2fm^4}$
$\epsilon$	0.67 (14)	

Table 5.1: The cross section and  $B(E2; 0_1^+ \to 2_1^+)$  of <sup>52</sup>Ti is compared to to the  $B(E2; 0_1^+ \to 2_1^+)$  measured by Dinca *et al.*[20] to derive the efficiency.

also by the other published test cases shown in the figure. Additionally, the measurement of  $^{52}$ Ti utilized  $^{nat}$ Au targets of two different thicknesses, permitting a further verification of the method by measuring the  $B(E2; 0_1^+ \rightarrow 2_1^+)$  of the targets. Finally, the transition rate of  $^{52}$ Ti was found to be in agreement with an earlier measurement by Brown *et al.*[62].

Dinca determined  $B(E2; 0_1^+ \to 2_1^+) = 567(51) \text{ e}^2\text{fm}^4$ , and the observed transition rate is scaled to the Dinca value by the factor

$$\epsilon = \frac{B(E2; 0_1^+ \to 2_1^+)_{obs}}{B(E2; 0_1^+ \to 2_1^+)_{Dince}} = 0.67(13). \tag{5.5}$$

This efficiency coupled with the efficiency of the simulation is the true efficiency of the APEX Array for this reaction. The photopeak efficiency is approximately 8.5%. The results are summarized in Table 5.1.

## 5.2 ${}^{50}$ Ca $B(E2; 0_1^+ \rightarrow 2_1^+)$ measurement

#### 5.2.1 Particle identification

The gating and calculation for the  $^{50}$ Ca transition rate follows the same method that was demonstrated for the  $^{52}$ Ti transition rate. The particle-identification

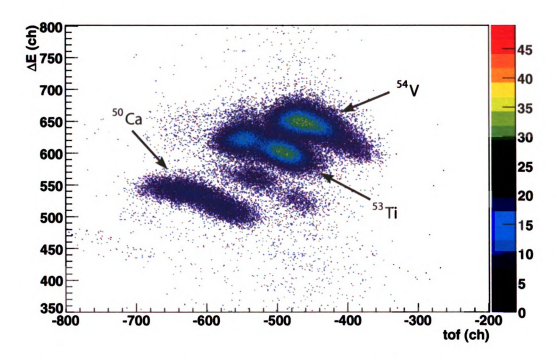


Figure 5.10: The particle identification spectrum with  $^{50}$ Ca and the other primary constituents  $^{53}$ Ti and  $^{53}$ V indicated. Corrections for beam correlations have not been implemented.

spectrum without corrections for the  $^{50}$ Ca cocktail beam is shown in Figure 5.10. The loci widths are significantly decreased by the application of corrections to the time of flight and energy loss in the ion chamber, the results of which are shown in Figure 5.11.  $^{50}$ Ca was delivered with 7% purity, with  $^{53}$ Ti and  $^{54}$ V as additional beam components, and two days of data were recorded.

#### **5.2.2** Cross section and $B(E2; 0_1^+ \rightarrow 2_1^+)$

The  $\gamma$ -ray spectrum background is reduced for the  $^{50}\mathrm{Ca}$  measurement following the method prescribed for  $^{52}\mathrm{Ti}$ , timing gates on the prompt  $\gamma$ -ray time peak of each PMT channel and a selection on the scattering angle. The contribution from feeding is found to be small from shell-model considerations, and the observed de-excitation cross section is calculated. The  $^{50}\mathrm{Ca}$  Coulomb excitation reaction is

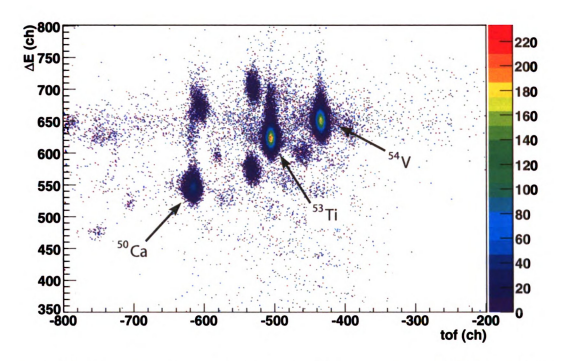


Figure 5.11: The corrected particle identification spectrum with  $^{50}$ Ca and the other primary constituents  $^{53}$ Ti and  $^{54}$ V indicated.

shown to be similar to that of  $^{52}$ Ti, demonstrating the propriety of applying the previously determined efficiency.

The scattering angle of  $^{50}$ Ca is restricted to avoid nuclear excitation and to minimize background. The minimum and maximum impact parameters are those used for  $^{52}$ Ti although the corresponding scattering angles are slightly shifted according to the A and Z of  $^{50}$ Ca (Equation 2.14). The simulated threshold parameters were determined through the  $\chi^2$  minimization to an  $^{88}$ Y source spectrum before the  $^{50}$ Ca data were collected. The response function with an exponential plus constant continuum fitted to the  $\gamma$ -ray energy spectrum is displayed in Figure 5.14. The fit is the thick, black line, and the continuum is dashed. The resulting observed cross section is 18.4(4.9) mb with the error largely due to uncertainty in the fit (24%). The other sources of uncertainty are the same as those given for the  $^{52}$ Ti case, with uncertainty of the simulated response function dominating (10%) after

the fit. Additions to the cross section due to feeding from excitation to higher-lying states will be examined with nuclear structure considerations.

A level diagram of the lower-lying states of <sup>50</sup>Ca is shown in Figure 5.12. The  $2_1^+$  state lies at 1027 keV, and feeding is possible from the  $2_2^+$  level at 2999 keV, the  $1_1^+$  level at 3519 keV, and the  $3_1^-$  level at 3993 keV. The 3519 keV level has been identified as a  $\mathbf{1}_{1}^{+}$  configuration in a recent deep inelastic transfer reaction measurement [63]. Table 2.2 shows that  $0_1^+ \rightarrow 1_1^+$  is an M1 transition, which is suppressed at intermediate beam energies [64]. In Reference [7], the  $\mathbf{3}_{1}^{-}$  state in  $^{52}$ Ca is found to be due to cross-shell excitations of protons, a situation unlikely to change significantly with a small reduction in the number of valence neutrons. The excitation to the  $\mathbf{3}_{1}^{-}$  in  $^{50}\mathrm{Ca}$  may therefore be estimated from the  $B(E3;0_1^+ \rightarrow 3_1^-) = 6.5 \times 10^3 \; \mathrm{e}^2 \mathrm{fm}^6$  transition rate in  $^{48}\mathrm{Ca[22]}. \; \mathrm{A} \; \beta$  -decay study [65] determined a 38(5)% branch to the  $2_1^+$  state, resulting in a contribution of 0.49 mb to the  $\gamma$ -ray cross section. The feeding contribution from the  $2^+_2$  state may be estimated from the GXFP1A predicted excitation rate,  $B(E2;0_1^+ \rightarrow 2_2^+) = 41.3 \text{ e}^2 \text{fm}^4$  $(e_n = 0.8)$ . The  $\beta$ -decay measurement and a deep inelastic transfer reaction study did not reveal feeding from the  $2^+_2$  to the  $0^+_1$ . Assuming a branching ratio of at most 1% leads to an estimated contribution of 0.10 mb to the cross section. Together, feeding from the  $2^+_2$  and  $3^-_1$  may contribute up to  $\approx 0.59$  mb to the cross section. However, this value is the feeding contribution to the cross section, not the observed cross section. Since the feeding contribution is small, the transition rate will initially be calculated assuming no feeding. A similar treatment of feeding can be found in Reference [66].

The efficiency determined with the  $^{52}$ Ti measurement can be used for the  $^{50}$ Ca measurement due to the similar kinematics of the two reactions and the nearly equivalent  $\gamma$ -ray angular distribution. Both reactions occur on  $^{\rm nat}$ Au targets, and the  $\beta$  at midtarget, the average location of the Coulomb excitation, differs by

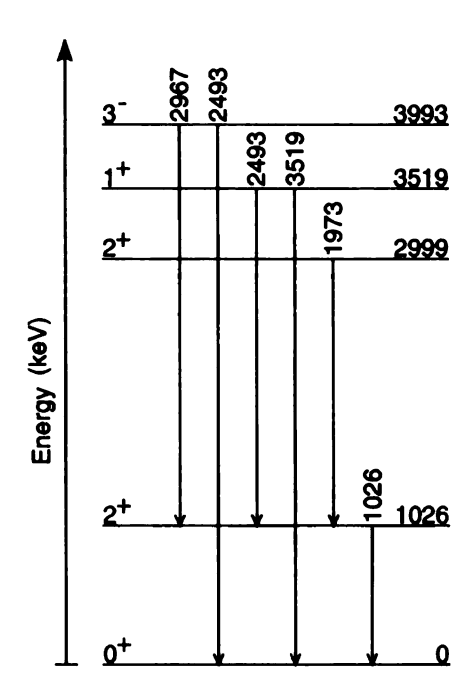


Figure 5.12: The lower-lying states of  $^{50}$ Ca from the NNDC[22] with  $J^{\pi}$  determined through  $\beta$  decay[65] and deep inelastic transfer reactions[63].

nat Au target	245	$mg/cm^2$
$oldsymbol{eta}$	0.363	
$N_{\gamma}$	973 (238)	
$E(2_1^+)$	1085 (80)	keV
$\sigma$	27.3(9.1)	mb
$B(E2; 0_1^+ \rightarrow 2_1^+)$	120 (41)	${ m e^2 fm^4}$
$A_n$	14.14	$ m efm^2$
$e_n$	0.77 (13)	

Table 5.2: The measured  $^{50}$ Ca cross section leading to the final transition rate value,  $B(E2;0_1^+\to 2_1^+)=120(41)~{\rm e}^2{\rm fm}^4$ .

0.1%. The energy of the  $^{50}$ Ca  $2_1^+$  state lies 34 keV lower in energy, less than the FWHM of the photopeak. The calculated angular distributions of  $\gamma$ -ray emission are shown in Figure 5.13; the  $^{50}$ Ca and  $^{52}$ Ti distributions very nearly overlap. Using the theory of Alder and Winther, the  $^{50}$ Ca transition rate is found to be  $B(E2; 0_1^+ \rightarrow 2_1^+) = 120(41) \ {\rm e}^2{\rm fm}^4$ . The results are summarized in Table 5.2. Returning to the feeding contribution, the 0.59 mb contribution to the cross section is  $\approx 2\%$  of the cross section, an insignificant amount relative to the 33% uncertainty.

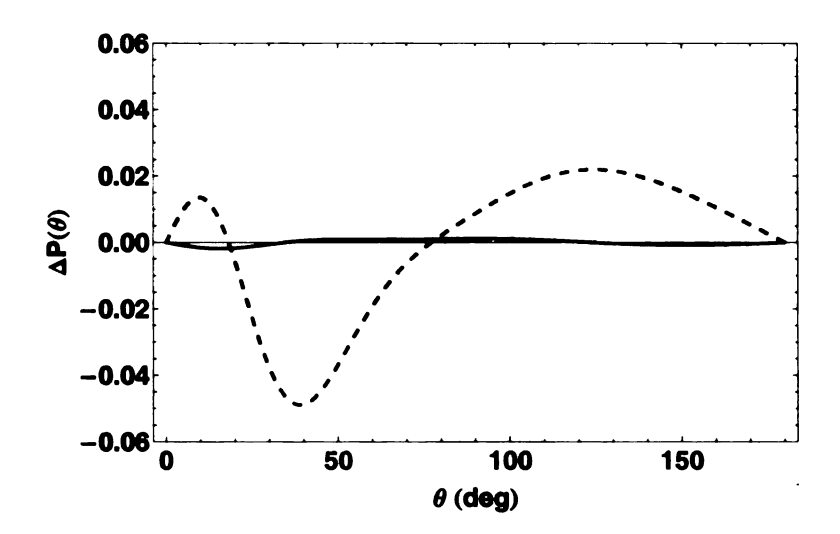


Figure 5.13: The difference in the angular distribution of  $^{50}$ Ca from that of  $^{52}$ Ti (solid line) is small. The difference in the angular distributions of  $^{76}$ Ge and  $^{52}$ Ti (dashed) is shown for comparison.

## 5.3 Effective charge in the pf shell

In Section 2.3.4 the question of effective charge in the pf shell is proposed. The neutron transition amplitude of  $^{50}$ Ca is predicted by the GXFP1A to be 14.14 efm<sup>2</sup>[24]. Following from Equation 2.5, the neutron effective charge is then

$$e_n = \sqrt{\frac{B(E2; 0_1^+ \to 2_1^+)}{A_n^2}} = 0.77(13)$$
 (5.6)

The larger effective charge suggested by du Reitz's study of  $^{51}$ Fe and  $^{51}$ Mn mirror nuclei,  $e_n \approx 0.8$ , is indicated by the value derived in this work. According to empirical results[16], the difference in effective charge ranges from the Coulomb value,  $e_p - e_n = 1.0$ , to 0.35. The proton effective charge is then expected to lie between 1.01 and 1.55, a range that includes the du Rietz value  $e_p \approx 1.15$ .

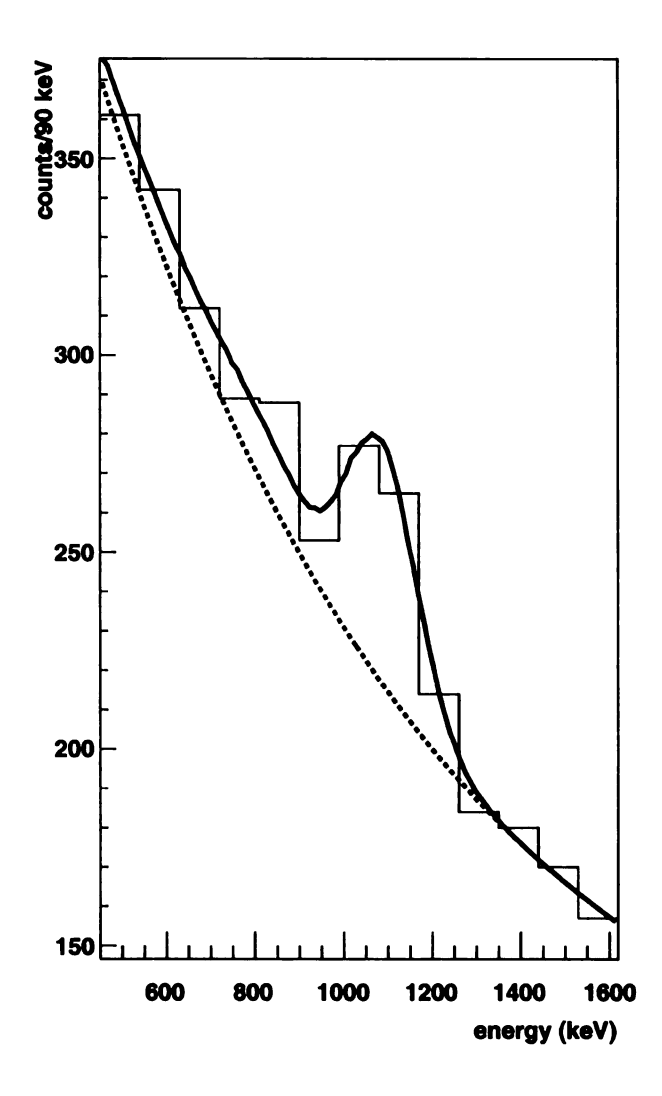


Figure 5.14: The fit of the response function plus continuum to the  $^{50}$ Ca  $\gamma$ -ray energy spectrum. The fit is drawn as a thick, black line, and the continuum is dashed.

#### 5.4 Conclusion

In Section 2.3.3, the core polarization was shown to arise from  $E=2\hbar\omega$  excitation of the core protons. The operator derived in a microscopic model that included 2p-2h excitations in the shell-model space resulted in a neutron effective charge  $e_n=0.57(03)$ . The operator in the macroscopic model, where the polarization charge is the result of excitations to  $\Delta n=2$  harmonic oscillator vibrations in the nuclear core, produced a neutron effective charge  $e_n=0.90$ . Because the matrix element calculated with the GXPF1A effective interaction agrees with two older interactions, the GXPF1[1] and the KB3[19], the derived effective charge suggests that the operator derived with the macroscopic, vibrational model better reproduces the true operator in this shell-model subspace than the microscopic shell model operator. The enhanced neutron effective charge additionally indicates a strengthened isovector quadrupole resonance.

The effective charge of  $^{50}$ Ca inferred in this thesis confirms the use of an enhanced neutron effective charge to reproduce the trend of the neutron-rich Ti transition strengths measured by Dinca et al.[20] (Figure 2.5). The  $E(2_1^+)$  2562 keV of  $^{52}$ Ca measured by Gade et al. [7] suggests an N=32 subshell closure, in line with the conclusion drawn from the investigation of the Ti isotopes. However, there remains no evidence for a shell closure at N=34; a definitive statement is prevented by the large uncertainty in the  $B(E2;0_1^+\to 2_1^+)$  of  $^{56}$ Ti. The measurement of the  $E(2_1^+)$  of  $^{54}$ Ca and the  $B(E2;0_1^+\to 2_1^+)$  of  $^{52,54}$ Ca would decisively resolve the question of the N=34 shell closure. The measurement of the transition strength of these two nuclei awaits increased beam production rates and improved experimental equipment.

In the coming months the new CAESAR (CAEsium Iodide ARray)  $\gamma$ -ray detector will be deployed at the NSCL. To avoid the loss in resolution inherent in

the double-sided PMT configuration of APEX, CAESAR will use segmentation for position sensitivity. The 192 square cylinders of CsI(Na) will have one face of each crystal nearly entirely covered by a PMT rather than a small fraction. Additionally, the threshold cutoff will occur at a fixed energy for each detector segment, leading to an array efficiency that will not vary significantly with position. Magnetic shielding will permit high-resolution PMTs to be used near the beamline magnets. The expected in-beam resolution of CAESAR is < 10% FWHM at 1 MeV with an efficiency of 40%, a great improvement over the 17% FWHM resolution and < 10% efficiency of APEX. The high efficiency of CAESAR will make possible the study of nuclei with currently impractically low production rates, leading to an exciting expansion in our knowledge of nuclear structure.

# Appendix A

# Simulated response functions of

## **APEX**

#### A.1 GEANT4

The GEANT4 model of the APEX Array played an essential role in the measurement described in this paper. Understanding the effect of the thresholds on the efficiency would have been a considerably more difficult task without the ability to test the hypothesis with a Monte Carlo model. In consideration of the important role of the simulation, abbreviated portions of key classes are reproduced to permit the replication of the results.

### A.1.1 Input files

The input files contain the following information:

#Mult: multiplicity of primary gamma rays

#Energy: comma separated list of gamma-ray energies (keV) of

# length MULT

#Intensity: comma separated list of gamma-ray intensities (%) of

# length MULT

#DecayDist: comma separated list of gamma-ray transition decay

# constants in distance (mm) traveled during the

# excited states' lifetimes of length MULT

#BetaMid: midtarget beta

#BeatPre: pretarget beta

#BetaPost: posttarget beta

#BeamWidthFWHM: horizontal, vertical spacial beam FWHM in mm

#BeamMomWidth: beam momentum width (%); must be defined after

# BetaPre

#AngDist: "uni" unidirectional, "iso" isotropic, or "E2" E2

# angular distribution

#E2Coeff: comma-separated list of E2 angular distribution

# coefficients

#TargetPos: x,y,z target position in centimeters

#Target: 0 for no target, "Au" or "Bi" to insert target

#ReconDist: assumed distance in mm of decay after center of

# target for Doppler reconstruction in mm; state

# after TargetPos

#Collimator: 0 for no collimator, anything else to insert

# the collimator

#Visualization: O for no visualization, anything else for

visualization

#Verbosity: 0 for none, 1 for some, 2 for all

#Alpha: energy scaling value in keV per channel

#Mu: linear attenuation coefficient in inverse centimeters

```
# Amplitude_\{up/dn\} = Alpha * exp(-Mu*(L/2+-X))
```

# where L is the crystal length and X is interaction point

The <sup>76</sup>Ge input file:

Mult: 1

Energy: 562.93

Intensity: 100.0

DecayDist: 3.1

BetaMid: 0.3960

BetaPre: 0.4092

BetaPost: 0.3814

BeamWidthFWHM: 10.0,10.0

BeamMomWidth: 3.0

AngDist: E2

E2Coeff: 1.0,-0.665148,-0.241809

TargetPos: 0,0,6.2

Target: Bi

ReconDist: 3.1

Collimator: 0

Visualization: 0

Verbosity: 0

Alpha: 7.87160

Mu: 0.047

The <sup>52</sup>Ti input file:

Mult: 1

Energy: 1049.73

Intensity: 100.0

DecayDist: 0.6

BetaPre: 0.3726

BetaMid: 0.3633

BetaPost: 0.3533

BeamWidthFWHM: 10.0,10.0

BeamMomWidth: 3.0

AngDist: E2

E2Coeff: 1.0,-0.593296.-0.188789

TargetPos: 0,0,6.2

Target: AuThin

ReconDist: 0.6

Collimator: 0

Visualization: 0

Verbosity: 0

Alpha: 7.87160

Mu: 0.047

The <sup>50</sup>Ca input file:

Mult: 1

Energy: 1026

Intensity: 100.0

DecayDist: 3.1

BetaPre: 0.3850

BetaMid: 0.3637

BetaPost: 0.3378

BeamWidthFWHM: 10.0,10.0

BeamMomWidth: 3.0

AngDist: E2

E2Coeff: 1.0,-0.587135,-0.184617

TargetPos: 0,0,6.2

Target: Au

ReconDist: 3.0

Collimator: 0

Visualization: 0

Verbosity: 0

Alpha: 7.87160

Mu: 0.047

Compilation constants are defined in Constants.h, and data structures are defined in Data.h.

/\*

--Compilation Constants--

General:

G4int NUM\_PRIMARY: maximum number of primary gammas possible

G4int NUM\_DETECTOR: number of detectors

ApexDetectorConstruction:

G4bool REMOVE\_NON\_DETECTORS: remove all objects except the detectors

(note: does not affect the heavimet collimator)

G4bool CHECK\_OVERLAPS: Check for geometric overlaps

```
#ifndef CONSTANTS_H
#define CONSTANTS_H
#define NUM_PRIMARY 2
#define NUM_DETECTOR 24
#define NUM_ANGDISTCOEFF 3
#define REMOVE_NON_DETECTORS false
#define CHECK_OVERLAPS false
#endif
#ifndef DATA_H
#define DATA_H 1
#include <globals.hh>
#include <G4ThreeVector.hh>
typedef struct PrimaryShot_t {
  // Laboratory frame data
  G4double Beta;
  G4ThreeVector EmisPos; // location of gamma emission
  G4double Energy;
  G4double Theta;
  G4double Phi;
  // Particle frame data
```

\*/

```
G4double PFEnergy;
  G4double PFTheta;
  G4double PFPhi;
};
typedef struct DetectorOutput_t {
  G4int
           NumHits;
  /* position of first hit on detector */
  G4ThreeVector FirstHitPos:
  /* total energy deposited in the crystal */
  G4double EnergyDep;
  G4double EnergyUp; /* energy out of up PMT */
  G4double EnergyDn; /* energy out of dn PMT */
  G4double EnergyRec; /* reconstructed energy */
  /* reconstructed energy, Doppler corrected */
  G4double EnergyRecDop;
  G4double PositionRec; /* reconstructed position */
};
```

## #endif

## A.1.2 Detector construction

The 24-bar NaI(Tl)  $\gamma$ -ray detector APEX is constructed in the class ApexDetectorConstruction along with the lead background shielding and the aluminum table.

```
#ifndef ApexDetectorConstruction_h
#define ApexDetectorConstruction_h 1
#include <globals.hh>
#include <G4LogicalVolume.hh>
#include <G4VUserDetectorConstruction.hh>
#include <G4Region.hh>
#include <sstream>
using std::stringstream;
#include "CApexInitialization.hh"
class ApexDetectorConstruction : public G4VUserDetectorConstruction {
public:
  ApexDetectorConstruction();
  ~ApexDetectorConstruction();
  G4VPhysicalVolume* Construct();
private:
  G4LogicalVolume* vault_log; // world volume
  G4LogicalVolume* beampipe_log;
  G4LogicalVolume* shieldLead_log; // Pb cylindrical shield
  G4LogicalVolume* shieldSteel_log; // steel cylindrical shield
  G4LogicalVolume* table_log;
  G4LogicalVolume* heavimet_log;
  G4LogicalVolume* target_log;
```

```
G4LogicalVolume* apexBar_log; // Mother; creates steel for jacket
G4LogicalVolume* apexBarVac_log;
                                   // Vacuum placed inside mother
G4LogicalVolume* apexBarCrystal_log;// Crystal placed inside
                                    // vacuum
G4LogicalVolume* window_log;
                                   // quartz windows place in vac
G4VPhysicalVolume* vault_phys;
G4VPhysicalVolume* beampipe_phys;
G4VPhysicalVolume* shieldLead_phys;
G4VPhysicalVolume* shieldSteel_phys;
G4VPhysicalVolume* table_phys;
G4VPhysicalVolume* heavimetUp_phys;
G4VPhysicalVolume* heavimetDn_phys;
G4VPhysicalVolume* target_phys;
G4VPhysicalVolume* apexBar_phys[23];
G4VPhysicalVolume* apexBarVac_phys;
G4VPhysicalVolume* apexBarCrystal_phys;
G4VPhysicalVolume* windowUp_phys;
G4VPhysicalVolume* windowDn_phys;
G4Region* aCrystalRegion; // crystal cut region
//Measurements
static const G4double m_HeavimetRadius;
static const G4double m_HeavimetCylHeight;
```

```
static const G4double m_HeavimetGap;
  G4ThreeVector m_HeavimetUpPos;
 G4ThreeVector m_HeavimetDnPos;
  G4bool
          m_Target;
  G4String m_TargetMaterial;
 CApexInitialization* m_pApexInit;
  stringstream
                     m_InfoSS; // log to store with output file
  G4int
                     m_NumberOfDetectors; // number of detectors
  static const G4bool m_RemoveNonDetectors;
  static const G4bool m_CheckOverlaps;
  void CheckOverlaps(G4VPhysicalVolume* volume) const;
};
#endif
#include "ApexDetectorConstruction.hh"
#include "ApexCrystalSD.hh"
#include "Constants.h"
#include <G4Material.hh>
#include <G4MaterialTable.hh>
#include <G4Element.hh>
#include <G4ProductionCuts.hh>
```

```
#include <G4ElementTable.hh>
#include <G4Box.hh>
#include <G4Tubs.hh>
#include <G4Trd.hh>
#include <G4LogicalVolume.hh>
#include <G4ThreeVector.hh>
#include <G4PVPlacement.hh>
#include <G4SDManager.hh>
#include <G4VisAttributes.hh>
#include <G4Color.hh>
#include <G4NistManager.hh>
//measured
const G4double ApexDetectorConstruction::m_HeavimetRadius =7.0*cm;
const G4double ApexDetectorConstruction::m_HeavimetCylHeight=7.6*cm;
const G4double ApexDetectorConstruction::m_HeavimetGap
                                                            =4.7*mm;
// Remove all objects except the detectors?
// (note: does not remove the heavimet collimator)
const G4bool
ApexDetectorConstruction::m_RemoveNonDetectors=REMOVE_NON_DETECTORS;
// Debug for overlapping volumes?
const G4bool
ApexDetectorConstruction::m_CheckOverlaps = CHECK_OVERLAPS;
```

```
ApexDetectorConstruction::ApexDetectorConstruction()
  :aCrystalRegion(0)
{
  m_InfoSS<<"ApexDetectorConstruction Info:"<<G4endl;</pre>
  // Get pointer to data initialization object
  m_pApexInit = CApexInitialization::Instance();
  m_NumberOfDetectors = m_pApexInit->NumOfDetectors();
  // Check if valid target entered.
  m_TargetMaterial = m_pApexInit->Target();
  if (m_TargetMaterial=="Au"||
      m_TargetMaterial=="Bi"||
      m_TargetMaterial=="AuThin")
    m_Target=true;
  else if (m_TargetMaterial=="0")
    m_Target=false;
  else {
    m_Target=false;
    G4cerr<<"ERROR> Invalid target material. "
  <<"No target included."<<G4endl;</pre>
  }
  m_HeavimetUpPos = m_HeavimetDnPos = m_pApexInit->TargetPosition();
  m_HeavimetUpPos +=
    G4ThreeVector(0.0,0.0,(m_HeavimetCylHeight+m_HeavimetGap)/2);
```

```
m_HeavimetDnPos +=
    G4ThreeVector(0.0,0.0,-(m_HeavimetCylHeight+m_HeavimetGap)/2);
}
G4VPhysicalVolume* ApexDetectorConstruction::Construct() {
  G4cout<<"Constructing Detectors....";
  if (m_Target||m_CheckOverlaps||m_RemoveNonDetectors)
    G4cout < < G4end1;
  if (m_RemoveNonDetectors) {
    G4cout<<" Only detector bars created.\n";
    m_InfoSS<<"Only detector bars created."<<G4endl;</pre>
  }
  //---- Material Definitions -----
  //
  G4NistManager* man = G4NistManager::Instance();
  G4Material* Al = man->FindOrBuildMaterial("G4_Al");
  G4Material* Pb = man->FindOrBuildMaterial("G4_Pb");
  G4Material* W = man->FindOrBuildMaterial("G4_W");
  G4Material* Fe = man->FindOrBuildMaterial("G4_Fe");
  G4Material* Au = man->FindOrBuildMaterial("G4_Au");
  G4Material* Bi = man->FindOrBuildMaterial("G4_Bi");
```

```
G4Material* air = man->FindOrBuildMaterial("G4_AIR");
G4Material* vacuum = man->FindOrBuildMaterial("G4_Galactic");
G4Material* NaI = man->FindOrBuildMaterial("G4_SODIUM_IODIDE");
G4Material* quartz = man->FindOrBuildMaterial("G4_SILICON_DIOXIDE");
//---- Volumes -----
// From Kaloskomis, et al.
const G4double kalInnerDetectorRadius = 42.8*cm/2;
//--- Vault (world volume) ----
// Arbitrarily chosen world half size
// 4*m x 4*m x 4*m
     //x axis: up
     //y axis: south
     //z axis: east, downstream along beam line
const G4double vault_x = 2*m;
const G4double vault_y = 2*m;
const G4double vault_z = 2*m;
G4Box *vault_box =
  new G4Box("vault_box",vault_x,vault_y,vault_z);
vault_log = new G4LogicalVolume(vault_box, air,
"vault_log",0,0,0);
// GEANT doesn't allow world volume to rotate.
// You'll have to convert to SeGA/S800 coordinates
```

```
// by yourself. Z is the beam axis.
vault_phys = new G4PVPlacement(0,G4ThreeVector(0,0,0),
  vault_log, "vault", 0, false, 0);
//--- Beampipe ----
//
const G4double innerRadiusOfPipe = 15.24*cm/2; // 6" pipe
const G4double outerRadiusOfPipe = innerRadiusOfPipe + 2.*mm;
const G4double halfLengthOfPipe = 1.5*m;
const G4double startingAngleOfPipe = 0.*deg;
const G4double spanningAngleOfPipe = 360.*deg;
if (!m_RemoveNonDetectors) {
  G4Tubs* beampipe_tub =
    new G4Tubs("beampipe_tub", innerRadiusOfPipe,
outerRadiusOfPipe, halfLengthOfPipe,
startingAngleOfPipe, spanningAngleOfPipe);
  beampipe_log =
     new G4LogicalVolume(beampipe_tub,A1,"beampipe_log",0,0,0);
  // centered in world concentric with z axis
  const G4double beampipePos_x = 0*m;
   const G4double beampipePos_y = 0*m;
   const G4double beampipePos_z = 0*m;
  beampipe_phys =
    new G4PVPlacement(0,
```

```
G4ThreeVector(beampipePos_x,
      beampipePos_y,
      beampipePos_z),
beampipe_log, "beampipe",
vault_log, false, 0);
   CheckOverlaps(beampipe_phys);
 }
 //--- Heavimet Collimator ----
 //
  if (m_pApexInit->Collimator()) {
    const G4double innerRadiusOfHeavimet = 0.0*cm;
    const G4double startingAngleOfHeavimet = 0.0*deg;
    const G4double spanningAngleOfHeavimet = 360.0*deg;
    G4Tubs* heavimet_tub =
      new G4Tubs("heavimet_tub",
 innerRadiusOfHeavimet, m_HeavimetRadius,
 m_HeavimetCylHeight/2,
 startingAngleOfHeavimet,spanningAngleOfHeavimet);
   heavimet_log =
      new G4LogicalVolume(heavimet_tub,W,"heavimet_log",0,0,0);
    heavimetUp_phys =
      new G4PVPlacement(0,m_HeavimetUpPos,
```

```
heavimet_log, "HeavimetUp",
vault_log, false, 0);
    heavimetDn_phys =
      new G4PVPlacement(0,m_HeavimetDnPos,
heavimet_log,"HeavimetDn",
vault_log, false, 0);
    CheckOverlaps(heavimetUp_phys);
    CheckOverlaps(heavimetDn_phys);
  };
  //--- Target ----
  //
  if (m_Target) {
    /*
     * The targets were measured to be the following thicknesses:
         Au: 0.100 mm
         Bi: 0.258 mm
     * Both of the measurements are a about 0.005 mm larger than
     * the values computed below. I assume that my micrometer
     * skills are only as good as good as this difference.
     * Jon Cook - 20060315
     */
```

```
G4double massThicknessOfTarget;
G4Material* targetMaterial;
if (m_TargetMaterial == "Au") {
  G4cout<<" Target: 519 mg/cm2 Au"<<G4endl;
  m_InfoSS<<"Target: 519 mg/cm2 Au"<<G4endl;</pre>
  massThicknessOfTarget = 518.84*mg/cm2;
  targetMaterial = Au;
} else if (m_TargetMaterial == "AuThin") {
  G4cout<<" Target: 184 mg/cm2 Au"<<G4endl;
  m_InfoSS<<"Target: 184 mg/cm2 Au"<<G4endl;</pre>
  massThicknessOfTarget = 184*mg/cm2;
  targetMaterial = Au;
} else if (m_TargetMaterial == "Bi") {
  G4cout<<" Target: 245 mg/cm2 Bi"<<G4endl;
  m_InfoSS<<"Target: 245 mg/cm2 Bi"<<G4endl;</pre>
  massThicknessOfTarget = 245*mg/cm2;
  targetMaterial = Bi;
} else {
  G4cerr<<"ERROR> Unknown target specified"<<G4endl;
  m_InfoSS<<"ERROR> Unknown target specified"<<G4endl;</pre>
  massThicknessOfTarget = 0.0000001*mg/cm2;
  targetMaterial = vacuum;
}
const G4double halfSideLengthOfTarget = 5.0*cm/2;
```

```
const G4double halfThicknessOfTarget =
      (massThicknessOfTarget/targetMaterial->GetDensity())/2;
   G4cout<<" Thickness of target: "<<halfThicknessOfTarget/mm*2
  <<" mm"<<G4endl;
   G4Box* target_box =
      new G4Box("target_box", halfSideLengthOfTarget,
halfSideLengthOfTarget, halfThicknessOfTarget);
   target_log =
      new G4LogicalVolume(target_box,targetMaterial,
  "target_log",0,0,0);
   target_phys =
      new G4PVPlacement(0,m_pApexInit->TargetPosition(),
target_log,"target_phys",
vault_log, false, 0);
    CheckOverlaps(target_phys);
  } else {
    G4cout<<" No target included."<<G4endl;
  }
  //--- Detector Bar ----
  //
  // 55.0 \times 6.0 \times 5.5(7.0) cm (L x H x W) according to Kaloskamus
  const G4double halfInnerWidthBar = 5.5*cm/2;
  const G4double halfOuterWidthBar = 7.0*cm/2;
  const G4double halfHeightBar
                                   = 6.0*cm/2;
```

```
const G4double jacketThickness = 0.4*mm; // Kaloskamis
const G4double halfInnerWidthBarVac =
 halfInnerWidthBar - jacketThickness;
const G4double halfOuterWidthBarVac =
  halfOuterWidthBar - jacketThickness:
const G4double halfHeightBarVac
 halfHeightBar - jacketThickness;
const G4double halfLengthBarVac
 halfLengthBar;
// No jacket on the ends of the bar due to difficulties with window
// extending beyond mother volume (apexBarVac).
//-- Steel Jacket --
G4Trd* apexBarJacketSolid_trd =
 new G4Trd("apexBarJacketSolid_trd",
    halfOuterWidthBar, halfInnerWidthBar,
    halfLengthBar, halfLengthBar,
    halfHeightBar);
apexBar_log = new G4LogicalVolume(apexBarJacketSolid_trd, Fe,
  "apexBar_log", 0, 0, 0);
//-- Vacuum inside Jacket --
G4Trd* apexBarVac_trd =
 new G4Trd("apexBarVac_trd",
```

const G4double halfLengthBar = 55.0\*cm/2;

```
halfOuterWidthBarVac, halfInnerWidthBarVac,
     halfLengthBarVac, halfLengthBarVac,
     halfHeightBarVac);
 apexBarVac_log =
   new G4LogicalVolume(apexBarVac_trd, vacuum,
"apexBarVac_log",0,0,0);
 apexBarVac_phys =
   new G4PVPlacement(0, G4ThreeVector(0,0,0), //unrotated, centered
     apexBarVac_log,
     "apexBarVac_phys",
     apexBar_log, // in an individual detector
     false,0);
 CheckOverlaps(apexBarVac_phys);
 //-- NaI Crystal and PMT windows --
 const G4double halfThicknessWindow = 1.1*cm/2;
 const G4double innerRadiusWindow = 0.0*cm;
 const G4double outerRadiusWindow = 4.4*cm/2;
 const G4double startingAngleWindow = 0.0*deg;
 const G4double spanningAngleWindow = 360.0*deg;
 const G4double crystalWidthReduction = 1.22*mm;
 const G4double crystalHeightReduction = 1.22*mm;
 const G4double halfInnerWidthBarCrystal =
   halfInnerWidthBarVac - crystalWidthReduction;
 const G4double halfOuterWidthBarCrystal =
   halfOuterWidthBarVac - crystalWidthReduction;
 const G4double halfHeightBarCrystal
```

```
halfHeightBarVac - crystalHeightReduction;
 const G4double halfLengthBarCrystal
   halfLengthBarVac - (2*halfThicknessWindow);
 m_pApexInit->SetHalfLengthOfCrystal(halfLengthBarCrystal);
 G4cout<<"\n APEX crystals reduced by "
<<2*crystalHeightReduction/mm<<" mm (height) and "
<<2*crystalWidthReduction/mm<<" mm (width)."<<G4endl;
 m_InfoSS<<"APEX crystals reduced by "
  <<2*crystalHeightReduction/mm<<" mm (height) and "
  <<2*crystalWidthReduction/mm<<" mm (width)."<<G4endl;
  G4Trd* apexBarCrystal_trd =
   new G4Trd("apexBarCrystal_trd",
      halfOuterWidthBarCrystal, halfInnerWidthBarCrystal,
      halfLengthBarCrystal, halfLengthBarCrystal,
      halfHeightBarCrystal);
  apexBarCrystal_log =
    new G4LogicalVolume(apexBarCrystal_trd, NaI,
"apexCrystalBar_log",0,0,0);
  apexBarCrystal_phys =
    new G4PVPlacement(0, G4ThreeVector(0,0,0),
      apexBarCrystal_log,
      "apexBarCrystal_phys",
      apexBarVac_log,
      false,0);
  CheckOverlaps(apexBarCrystal_phys);
```

```
G4Tubs* window_tub = new G4Tubs("window_tub",
innerRadiusWindow, outerRadiusWindow,
halfThicknessWindow,
startingAngleWindow,
spanningAngleWindow);
window_log =
 new G4LogicalVolume(window_tub,quartz,"window_log",0,0,0);
const G4double windowUpPos =
 halfLengthBarCrystal+halfThicknessWindow;
const G4double windowDnPos = -windowUpPos;
G4RotationMatrix windowRM;
G4double theta = 90*deg;
windowRM.rotateX(theta);
windowUp_phys =
 new G4PVPlacement(G4Transform3D(windowRM,
 G4ThreeVector(0, windowUpPos, 0)),
    window_log,"WindowUp", apexBarVac_log, false, 0);
windowDn_phys =
 new G4PVPlacement(G4Transform3D(windowRM,
 G4ThreeVector(0, windowDnPos,0)),
    window_log,"WindowDn", apexBarVac_log, false, 0);
CheckOverlaps(windowUp_phys);
CheckOverlaps(windowDn_phys);
// physical implementation of APEX bars
```

```
//
const G4double detRadius = kalInnerDetectorRadius + halfHeightBar;
const G4double startingAngle = 0.*deg;
const G4double incrementAngle = 360.*deg / m_NumberOfDetectors;
for (G4int detectorNumber=0;
    detectorNumber<=(m_NumberOfDetectors-1); detectorNumber++){</pre>
 G4double phi = startingAngle + incrementAngle*detectorNumber;
 G4double detPos_x = detRadius*cos(phi);
 G4double detPos_y = detRadius*sin(phi);
 G4double detPos_z = 0; // position along beamline fixed
 G4RotationMatrix rm;
 G4double theta = 90*deg;
 rm.rotateX(theta);
  rm.rotateZ(phi-90*deg);
 // Store rotation so that internal position can
  // be reconstructed later.
  m_pApexInit->SetDetRotMatrix(detectorNumber,rm);
  char physName[1024];
  sprintf(physName, "apexBar_phys: %d", detectorNumber);
  apexBar_phys[detectorNumber] =
    new G4PVPlacement(G4Transform3D(rm,G4ThreeVector(detPos_x,
     detPos_y,
     detPos_z)),
```

```
apexBar_log, physName,
vault_log, false, detectorNumber);
    CheckOverlaps(apexBar_phys[detectorNumber]);
  }
  //--- Array Shielding ----
  //
  // Lead part
  //
  G4double innerRadiusOfTube =
    kalInnerDetectorRadius + 2*halfHeightBar + 0.75*cm;
  G4double outerRadiusOfTube = innerRadiusOfTube + 2.1*cm;
  const G4double halfLengthOfTube = 65*cm/2;
  const G4double startingAngleOfTube = 0.*deg;
  const G4double spanningAngleOfTube = 360.*deg;
  // centered in world concentric with z axis
  const G4double ShieldPos_x = 0*m;
  const G4double ShieldPos_y = 0*m;
  const G4double ShieldPos_z = 0*m;
  if (!m_RemoveNonDetectors) {
    G4Tubs* shieldLead_tub =
      new G4Tubs("shieldLead_tub", innerRadiusOfTube,
 outerRadiusOfTube, halfLengthOfTube,
 startingAngleOfTube, spanningAngleOfTube);
```

```
shieldLead_log = new G4LogicalVolume(shieldLead_tub, Pb,
 "shieldLead_log", 0, 0, 0);
    shieldLead_phys =
      new G4PVPlacement(0,
G4ThreeVector(ShieldPos_x,
      ShieldPos_y,
      ShieldPos_z),
shieldLead_log, "shieldLead",
vault_log, false, 0);
    CheckOverlaps(shieldLead_phys);
  }
  // Steel part
  //
  // uses dimensions given in Lead section above
  //
  innerRadiusOfTube = outerRadiusOfTube;
  outerRadiusOfTube = innerRadiusOfTube + 1.*cm;
  if (!m_RemoveNonDetectors) {
    G4Tubs* shieldSteel_tub =
      new G4Tubs("shieldSteel_tub", innerRadiusOfTube,
 outerRadiusOfTube, halfLengthOfTube,
 startingAngleOfTube, spanningAngleOfTube);
    shieldSteel_log = new G4LogicalVolume(shieldSteel_tub, Fe,
  "shieldSteel_log", 0, 0, 0);
    shieldSteel_phys =
```

```
new G4PVPlacement(0,
G4ThreeVector(ShieldPos_x,
     ShieldPos_y, ShieldPos_z),
shieldSteel_log, "shieldSteel",
vault_log, false, 0);
   CheckOverlaps(shieldSteel_phys);
 }
 //---- Table ----
 //
  const G4double halfLength_x = 1.27*cm/2; // equivalent to 1/2 inch
  const G4double halfLength_y = 56.3*cm/2;
  const G4double halfLength_z = 167.5*cm/2;
   // approximate value!!!
  const G4double tablePos_x = -1.*(innerRadiusOfTube + 7.*cm);
  const G4double tablePos_y = 0.;
                                           // centered on beamline
   // Table edge aligned with end of PMT
  const G4double tablePos_z = -(halfLength_z - halfLengthOfTube)
                              + 10*cm;
  if (!m_RemoveNonDetectors) {
    G4Box* table_box =
      new G4Box("table_box", halfLength_x,
halfLength_y, halfLength_z);
    table_log =
      new G4LogicalVolume(table_box, A1, "table_log", 0,0,0);
```

```
table_phys =
     new G4PVPlacement(0,
G4ThreeVector(tablePos_x,
     tablePos_y, tablePos_z),
table_log, "table", vault_log, false, 0);
   CheckOverlaps(table_phys);
  }
  // ----- Make Sensitive Detectors -----
  // Make the crystals the active volumes
  G4SDManager* SDman = G4SDManager::GetSDMpointer();
  G4String CrystalSDname = "Apex/Crystal";
  ApexCrystalSD* CrystalSD =
    new ApexCrystalSD( CrystalSDname, "CrystalCollection" );
  SDman->AddNewDetector(CrystalSD);
  apexBarCrystal_log->SetSensitiveDetector(CrystalSD);
  // ----- Visualization Options -----
  //
  vault_log->SetVisAttributes(G4VisAttributes::Invisible);
  apexBarVac_log->SetVisAttributes(G4VisAttributes::Invisible);
                        (0.0, 0.75, 1.0, 0.75);
  G4Color windowBlue
  G4Color targetMetallic (0.537, 0.439, 0.302);
                        (0.5, 0.5, 0.5);
  G4Color lead
```

```
G4int shieldLineSegments = 50;
G4VisAttributes* windowVisAtt = new G4VisAttributes(windowBlue);
window_log->SetVisAttributes(windowVisAtt);
if (m_Target) {
 G4VisAttributes* targetVisAtt =
   new G4VisAttributes(targetMetallic);
 targetVisAtt->SetForceSolid(true);
 target_log->SetVisAttributes(targetVisAtt);
}
G4VisAttributes* leadVisAtt = new G4VisAttributes(lead);
leadVisAtt->SetForceLineSegmentsPerCircle(shieldLineSegments);
shieldLead_log->SetVisAttributes(leadVisAtt);
G4VisAttributes* steelShieldVisAtt = new G4VisAttributes();
steelShieldVisAtt->
         SetForceLineSegmentsPerCircle(shieldLineSegments);
shieldSteel_log->SetVisAttributes(steelShieldVisAtt);
m_pApexInit->SetInfoDetConstruct(m_InfoSS.str());
G4cout<<" done.\n\n";
// Returns the pointer to the physical world:
return vault_phys;
```

}

```
void
ApexDetectorConstruction::
   CheckOverlaps(G4VPhysicalVolume* volume) const
{
  if (m_CheckOverlaps)
    volume->CheckOverlaps();
}
A.1.3
        \gamma-ray generator
The ApexPrimaryGeneratorAction class manages the emission of \gamma rays.
#ifndef ApexPrimaryGeneratorAction_h
#define ApexPrimaryGeneratorAction_h 1
#include "Data.hh"
#include "CApexInitialization.hh"
#include "CRootManager.hh"
#include "CAngularDistribution.hh"
#include <G4VUserPrimaryGeneratorAction.hh>
class G4ParticleGun;
class G4Event;
class
ApexPrimaryGeneratorAction : public G4VUserPrimaryGeneratorAction {
```

public:

```
ApexPrimaryGeneratorAction();
  ~ApexPrimaryGeneratorAction();
  void GeneratePrimaries(G4Event* anEvent);
private:
  G4ParticleGun*
                       m_pParticleGun; // gamma-ray gun
  CApexInitialization* m_pApexInit; // input manager
  CRootManager*
                       m_pRootManager; // output manager
  CAngularDistribution* m_pAngDist; // angular distribution src
  G4double
                 m_BetaEmission; // beta (v/c) of emitted gamma ray
  G4ThreeVector m_EmissionPos; // position of gamma source
  G4LorentzVector m_GammaVector; // gamma-ray 4 vector
  G4ThreeVector m_ProjMomentum; // unit vector of proj. momentum
  PrimaryShot_t m_Shot;
                                // data about this primary event
  // ptr to function producing a random, unitary G4ThreeVector
  // in a given distribution
  AngDistFn m_AngDistRandomVector;
  void
           DopplerShiftGamma(); // Doppler shift gamma to lab frame
  void
           Print() const;
                               // print contents of m_Shot
};
#endif // #ifndef ApexPrimaryGeneratorAction_h
#include "ApexPrimaryGeneratorAction.hh"
```

```
#include "Constants.h"
#include <globals.hh>
#include <G4Event.hh>
#include <G4ParticleGun.hh>
#include <G4ParticleTable.hh>
#include <G4ParticleDefinition.hh>
#include <Randomize.hh>
#define CALL_PTR_MEMBER_FN(ptrToObject,ptrToMember)
  ((ptrToObject)->*(ptrToMember))
ApexPrimaryGeneratorAction::ApexPrimaryGeneratorAction () {
  G4cout << "Creating primary event generator...";
  // Get places to find and put information
  m_pApexInit = CApexInitialization::Instance();
  m_pRootManager = CRootManager::Instance();
  m_pAngDist = new CAngularDistribution();
  // Number of particles to be shot in one invocation
  const G4int n_particle = 1;
  m_pParticleGun = new G4ParticleGun(n_particle);
  // Tell gun to fire gammas
  G4ParticleTable* particleTable =
    G4ParticleTable::GetParticleTable();
```

```
G4String particleName = "gamma";
G4ParticleDefinition* particle =
 particleTable->FindParticle(particleName);
m_pParticleGun->SetParticleDefinition(particle);
// Projectile moves along z axis
m_ProjMomentum = G4ThreeVector(0.0,0.0,1.0);
// Select angular distribution
G4String angularDistribution = m_pApexInit->AngularDistribution();
if (angularDistribution=="uni") {
  m_AngDistRandomVector =
    &CAngularDistribution::UnidirectionalDirection;
  G4cout<<"\n Unidirectional angular distribution selected.\n";
} else if(angularDistribution=="iso") {
  m_AngDistRandomVector =
    &CAngularDistribution::IsotropicRandomDirection;
  G4cout<<"\n Isotropic angular distribution selected."<<G4endl;
} else if(angularDistribution=="E2") {
  m_AngDistRandomVector = &CAngularDistribution::E2RandomDirection;
  G4cout<<"\n E2 angular distribution selected."<<G4endl;
} else {
  m_AngDistRandomVector =
    &CAngularDistribution::UnidirectionalDirection;
  G4cerr<<"\n No angular distribution selected; "
<<"using unidirectional."<<G4endl;</pre>
```

```
}
 G4cout << " done.\n";
}
ApexPrimaryGeneratorAction::~ApexPrimaryGeneratorAction() {
  delete m_pParticleGun;
 delete m_pAngDist;
}
void ApexPrimaryGeneratorAction::GeneratePrimaries(G4Event* anEvent)
{
  if (m_pApexInit->VerbosityLevel()>0)
   G4cout <<"\n\n\n----\n";
  /*
       Clear all primary and detector info in the event buffer.
   * Clearing the buffer can't be done in
   * ApexEventAction::BeginOfEventAction because GeneratePrimaries
     is called before BeginOfEventAction.
   * Of course.
   */
  m_pRootManager->ClearEvent();
  /*
       For each gamma, check if it's going to be generated this
```

```
* instance, sample an emission position, sample a random
  * direction from the chosen distribution, boost it if
  * necessary, fire away, and record data.
  */
 for(unsigned i=0; i<m_pApexInit->PrimaryMultiplicity(); i++ ) {
    if (CLHEP::RandFlat::shoot()<=m_pApexInit->GammaIntensity(i)){
      // within branching ratio probability, shoot a gamma
      // Determine position of emission
     m EmissionPos =
G4ThreeVector(
 CLHEP::RandGauss::shoot(m_pApexInit->TargetPosition().x(),
 m_pApexInit->BeamSigmaX()),
 CLHEP::RandGauss::shoot(m_pApexInit->TargetPosition().y(),
 m_pApexInit->BeamSigmaY()),
 m_pApexInit->TargetPosition().z() +
 CLHEP::RandExponential::shoot(
      m_pApexInit->GammaLengthDecayConst(i))
  );
      m_pParticleGun->SetParticlePosition(m_EmissionPos);
      // Create Lorentz Vector of gamma ray
      m_GammaVector =
G4LorentzVector(m_pApexInit->GammaEnergy(i) *
```

```
CALL_PTR_MEMBER_FN(m_pAngDist,
   m_AngDistRandomVector)(),
m_pApexInit->GammaEnergy(i));
     // Record what is happening in the particle frame
     m_Shot.PFEnergy = m_GammaVector.getT();
     m_Shot.PFTheta = m_GammaVector.theta();
     m_Shot.PFPhi = m_GammaVector.phi();
     // Boost!
      if (m_pApexInit->BetaMidtarget()!=0.0)
DopplerShiftGamma();
      else
m_BetaEmission=0.0;
      // Record what is happening in the lab frame
      m_Shot.Beta
                     = m_BetaEmission;
      m_Shot.EmisPos = m_EmissionPos;
      m_Shot.Energy = m_GammaVector.getT();
      m_Shot.Theta = m_GammaVector.theta();
      m_Shot.Phi
                     = m_GammaVector.phi();
      m_pRootManager->AddPrimaryData(&m_Shot,i);
      // Fire the gamma ray!
```

```
m_pParticleGun->SetParticleMomentumDirection
(m_GammaVector.getV());
     m_pParticleGun->SetParticleEnergy(m_GammaVector.getT());
     m_pParticleGun->GeneratePrimaryVertex(anEvent);
   } else {
     // not within branching ratio probability; record null event
     m_Shot.PFEnergy = 1.0*keV;
     m_Shot.PFTheta = -5.0*deg;
     m_Shot.PFPhi = -185.0*deg;
     m_Shot.Energy = 1.0*keV;
     m_Shot.Beta = 0.0;
     m_Shot.Theta = -5.0*deg;
     m_Shot.Phi = -185.0*deg;
     m_{EmissionPos} = G4ThreeVector(0.*cm, 0.*cm, -10.*cm);
     m_pRootManager->AddPrimaryData(&m_Shot,i);
   }
   if (m_pApexInit->VerbosityLevel()>0)
     Print();
 } // end loop over gamma list
 if (m_pApexInit->VerbosityLevel()>0)
   G4cout <<"----\n";
```

```
/*
     Takes m_GammaVector, which is already set in the
* particle frame for the i'th gamma ray, and Doppler boosts
 * into the lab frame along the z axis using the betas given
* in the input file and provided here by m_pApexInit.
 * In my case, the momentum width is much greater than the
 * momentum acceptance, and a block function is assumed.
 * The position resolution of APEX is so poor that the
 * momentum distribution doesn't matter.
 * Also, for 76Ge betaPostTarget*c*lifetime = 3 mm
 * while the target is 0.258 mm thick. The gamma is emitted
 * after the target.
 */
void ApexPrimaryGeneratorAction::DopplerShiftGamma() {
  G4double scalingOfBetaDueToBeamWidth =
    1 + m_pApexInit->BeamBetaWidth()*CLHEP::RandFlat::shoot(-0.5,0.5);
  m_BetaEmission =
    m_pApexInit->BetaPosttarget()*scalingOfBetaDueToBeamWidth;
  m_GammaVector.boostZ(m_BetaEmission);
  return:
```

}

}

## A.1.4 Angular distribution

The CAngular Distribution class returns a random vector from a unidirectional, isotropic, or E2 distribution.

```
/*
     Class for creating isotropic, unidirectional, and
 * E2 angular distributions.
 * Written by Jon Cook
 */
#ifndef CANGULARDISTRIBUTION_H
#define CANGULARDISTRIBUTION_H
#include <globals.hh>
#include <Rtypes.h>
#include <TF1.h>
#include "CApexInitialization.hh"
class CAngularDistribution {
public:
```

```
CAngularDistribution();
  ~CAngularDistribution();
  void Coefficients(G4double a0, G4double a2, G4double a4);
  G4ThreeVector UnidirectionalDirection();
  G4ThreeVector IsotropicRandomDirection();
  G4ThreeVector E2RandomDirection();
private:
  static const UInt_t fkNumberOfAngDistCoeff =
  (UInt_t)NUM_ANGDISTCOEFF;
  CApexInitialization* fApexInit;
  // 0,2,4 Legrange coefficients
  Double_t fAngularCoeff[fkNumberOfAngDistCoeff];
  TF1* fAngularDistribution;
};
typedef G4ThreeVector (CAngularDistribution::*AngDistFn)();
#endif // #ifndef CANGULARDISTRIBUTION_H
#include "CAngularDistribution.hh"
#include <G4RandomDirection.hh>
// Function can't be member of the class. See TF1 documentation.
Double_t CAngularDistributionAngularFunction(Double_t* theta,
```

```
Double_t cosThetaSq = cos(*theta);
  cosThetaSq *= cosThetaSq;
 Double_t value = 1/(4*TMath::Pi()) *
    (
    param[0] +
    param[1] * 1./2.*(3.*cosThetaSq-1.) +
    param[2] * 1./8.*(35.*cosThetaSq*cosThetaSq-30.*cosThetaSq+3.)
    ) * sin(*theta);
 return value;
}
CAngularDistribution::CAngularDistribution() {
  for (UInt_t i=0; i<fkNumberOfAngDistCoeff; i++)</pre>
 fAngularCoeff[i]=0.0;
  fApexInit = CApexInitialization::Instance();
  Coefficients(fApexInit->AngDistCoeff(0),
       fApexInit->AngDistCoeff(1),
       fApexInit->AngDistCoeff(2));
  /*
   * Create angular distribution on [0,pi) of E2 transition using
   * even Legendre Polynomials up to order 4.
```

Double\_t\* param) {

```
* Using 180*8 = 1440 binning for 1/8 degree resolution
  * corresponding to approximately 1 mm resolution at APEX.
  * Since the bin is approximated by a parabola and APEX has
  * a position resolution of some centimeters, 1 mm resolution
  * is quite sufficient.
   */
 fAngularDistribution = new TF1("AngDist",
                                 CAngularDistributionAngularFunction,
0.0, TMath::Pi(),
                                 fkNumberOfAngDistCoeff);
  Int_t npx = 1440;
 fAngularDistribution->SetNpx(npx);
 fAngularDistribution->SetParName(0, "a0");
  fAngularDistribution->SetParName(1, "a2");
  fAngularDistribution->SetParName(2, "a4");
  fAngularDistribution->SetParameter(0,fAngularCoeff[0]);
  fAngularDistribution->SetParameter(1,fAngularCoeff[1]);
  fAngularDistribution->SetParameter(2,fAngularCoeff[2]);
}
CAngularDistribution::~CAngularDistribution() {
 delete fAngularDistribution;
}
```

```
void CAngularDistribution::Coefficients(G4double a0, G4double a2,
                                        G4double a4) {
  fAngularCoeff[0] = (Double_t)a0;
  fAngularCoeff[1] = (Double_t)a2;
  fAngularCoeff[2] = (Double_t)a4;
}
G4ThreeVector CAngularDistribution::UnidirectionalDirection() {
  G4ThreeVector randomVector = G4ThreeVector(3.,0.,1.);
 return randomVector.unit();
}
G4ThreeVector CAngularDistribution::IsotropicRandomDirection() {
  return G4RandomDirection();
}
G4ThreeVector CAngularDistribution::E2RandomDirection() {
  G4ThreeVector randomVector = G4RandomDirection();
  randomVector.setTheta((G4double)fAngularDistribution->GetRandom());
  return randomVector;
}
```

## A.1.5 Event action

The processing of the event is handled by the ApexEventAction class.

```
#ifndef ApexEventAction_h
#define ApexEventAction_h 1
#include <G4UserEventAction.hh>
#include <globals.hh>
#include "CApexInitialization.hh"
#include "CRootManager.hh"
#include "CApexCalculator.hh"
class G4Event;
class ApexEventAction : public G4UserEventAction
{
 public:
    ApexEventAction();
    virtual ~ApexEventAction();
    virtual void BeginOfEventAction(const G4Event*);
    virtual void EndOfEventAction(const G4Event*);
    inline void SetDrawFlag(G4bool val) { drawFlag = val; };
private:
  CApexInitialization* m_pApexInit;
```

```
CRootManager*
                      m_pRootManager;
 vCApexCalculator
                      m_vCalculator;
 G4int
                       m_CrystalCollID;
 G4bool drawFlag;
};
#endif
#include "ApexEventAction.hh"
#include "ApexCrystalHit.hh"
#include "ApexCrystalSD.hh"
#include <G4Event.hh>
#include <G4EventManager.hh>
#include <G4HCofThisEvent.hh>
#include <G4VHitsCollection.hh>
#include <G4TrajectoryContainer.hh>
#include <G4Trajectory.hh>
#include <G4VVisManager.hh>
#include <G4SDManager.hh>
#include <G4UImanager.hh>
#include <G4ios.hh>
#include <vector>
using std::vector;
```

```
ApexEventAction::ApexEventAction()
  :drawFlag(false)
{
 m_pApexInit = CApexInitialization::Instance();
 m_pRootManager = CRootManager::Instance();
 m_vCalculator = vCApexCalculator(m_pApexInit->NumOfDetectors());
}
ApexEventAction::~ApexEventAction()
{;}
void ApexEventAction::BeginOfEventAction(const G4Event*) {
  if(drawFlag)
    {
      G4VVisManager* pVVisManager =
G4VVisManager::GetConcreteInstance();
      if(pVVisManager)
{
  G4UImanager::GetUIpointer()->ApplyCommand("/vis~/draw/current");
}
    }
}
```

```
void ApexEventAction::EndOfEventAction(const G4Event* evt ) {
  G4SDManager * SDman = G4SDManager::GetSDMpointer();
  G4String colNam;
  m_CrystalCollID
    SDman->GetCollectionID(colNam="CrystalCollection");
  //G4int eventNum = evt->GetEventID();
  G4HCofThisEvent * HCE = evt->GetHCofThisEvent();
  ApexCrystalHitsCollection* crystalHC = 0;
  if(HCE)
    crystalHC =
      (ApexCrystalHitsCollection*)(HCE->GetHC(m_CrystalCollID));
  if(crystalHC) {
    G4int n_hit = crystalHC->entries();
    /*
      From HC get detector number, energy, and position
      Pass info to CApexCalculator and calculate
      Pass calculated values to CRootWriter
    */
    for(size_t j=0;j<m_pApexInit->NumOfDetectors();j++)
```

```
m_vCalculator[j].Clear();
   // create array of hit detectors
   vector<G4int> vHitDetector;
   G4int detNum = -1;
   for(G4int i=0;i<n_hit;i++) {</pre>
      detNum=(*crystalHC)[i]->DetNum();
      m_vCalculator[detNum].AddHit((*crystalHC)[i]->Edep(),
   (*crystalHC)[i]->Position());
      // If detector is newly hit in this event, add it to the list
     //of hit detectors
      G4bool NewHitDet = true;
      for (size_t i=0; i<vHitDetector.size(); i++) {</pre>
if (vHitDetector[i] == detNum)
 NewHitDet = false;
      };
      if (NewHitDet) {
vHitDetector.push_back(detNum);
      }:
    }
    // Calculate PMT effects for each hit detector and
```

```
// add the results to the event
    for (size_t i=0; i<vHitDetector.size(); i++) {</pre>
      DetectorOutput_t* output =
m_vCalculator[ vHitDetector[i] ].Calculate();
      m_pRootManager->AddDetectorData(output, vHitDetector[i]);
      if (m_pApexInit->VerbosityLevel()>0)
if (output->EnergyRec>0.0)
 m_vCalculator[ vHitDetector[i] ].Print(vHitDetector[i]);
    }
    // Write this event to file
    m_pRootManager->WriteEvent();
 } // endif(crystalHC)
  if(drawFlag)
    {
      G4VVisManager* pVVisManager =
G4VVisManager::GetConcreteInstance();
      if(pVVisManager)
{
  if(crystalHC)
                   crystalHC->DrawAllHits();
  G4UImanager::GetUIpointer()->ApplyCommand("/vis~/show/view");
```

```
}
}
```

## A.1.6 Double-sided scintillator model

The deposited energy is treated according to the model described in Section 3.3 in the class CApexCalculator.

```
#ifndef CApexCalculator_h
#define CApexCalculator_h
#include <vector>
#include <G4Types.hh>
#include <G4ios.hh>
#include <G4String.hh>
#include <G4ThreeVector.hh>
#include <G4RotationMatrix.hh>
#include <Randomize.hh>
#include "CApexInitialization.hh"
#include "Data.hh"
class CApexCalculator {
public:
  CApexCalculator();
  ~CApexCalculator();
```

```
void AddHit(G4double energy, G4ThreeVector pos);
  DetectorOutput_t* Calculate();
  void Clear();
  void Print(G4int detNum) const;
  G4int
           NumHits() const;
  G4double DepositedEnergy() const;
  G4ThreeVector FirstHitPosition() const;
  G4double AmplitudeUp() const;
  G4double AmplitudeDn() const;
  G4double ReconEnergy() const;
  G4double DoppReconEnergy() const;
  G4double ReconPosition() const;
private:
  CApexInitialization *m_pApexInit;
  // fixed values
  // scintillation efficiency
  static const G4double m_ScintEfficiency;
  // average scintillation photon energy
  static const G4double m_AveragePhotonEnergy;
  // cumulative NaI scintillation effect
  static const G4double m_ScintEffects;
  // index of refraction of air
  static const G4double m_IndexRefractAir;
```

```
// index of refraction of NaI
static const G4double m_IndexRefractNaI;
// critical angle of the NaI-air joint
static const G4double m_CriticalAngle;
// proportion of scintillation photons surviving TIR
static const G4double m_ProportionTransmitted;
// cumulative effects at the scintillation point
static const G4double m_ScintPointEffects;
// ratio of window to crystal area
static const G4double m_WindowSizeFactor;
// transmission efficiency through the window
static const G4double m_WindowLossFactor;
// cumulative effect of the window
static const G4double m_WindowTransmission;
// PMT quantum efficiency
static const G4double m_PMTquantEff;
// factor my which the statics are reduced to match data
static const G4double m_StaticsScaleFactor;
// cumulative PMT and window effect
static const G4double m_WindowPMTeffects;
// inner radius of the APEX array
static const G4double m_ApexRadius;
// depth of gamma interaction with the crystal
static const G4double m_InteractionDepth;
// radius of gamma interaction with APEX
static const G4double m_InteractionRadius;
```

```
// raw values
// number of interactions
G4int
        m_NumHits;
// energy deposited by one hit
G4double m_Energy;
// internal point of current interaction
G4ThreeVector m_InternalPosition;
// internal point of first interaction
G4ThreeVector m_FirstHitPosition;
// calculated values
// sum of energies deposited for one primary event
G4double m_RawSumEnergy;
// number of scintillation photons that reach the up
// end of the crystal
G4double m_PhotonsUp;
// number of scintillation photons that reach the dn
// end of the crystal
G4double m_PhotonsDn;
// amplitude of up PMT output
G4double m_AmplitudeUp;
// amplitude of dn PMT output
G4double m_AmplitudeDn;
// reconstructed energy
G4double m_ReconEnergy;
// reconstructed position
```

```
G4double m_ReconPosition;
 // time component is Doppler-corrected reconstructed
 // energy; x and y are fixed values
 G4LorentzVector m_GammaVector;
 // data structure for output of interaction
 DetectorOutput_t m_Output;
 void TransportHitToPMT();
 void CalculatePMT();
 void Reconstruct();
 void DopplerCorrect();
 void CollectConfigInfo();
};
typedef std::vector<CApexCalculator> vCApexCalculator;
#endif // #ifndef CApexCalculator_h
#include "CApexCalculator.hh"
#include <sstream>
//(see Knoll, page 233)
//
// Efficiency of conversion of deposited energy to photons
```

```
const G4double CApexCalculator::m_ScintEfficiency
                                                      = 0.12;
// Average energy of a scintillation photon
const G4double CApexCalculator::m_AveragePhotonEnergy = 3*eV;
//Number used at runtime
const G4double CApexCalculator::m_ScintEffects
               m_ScintEfficiency/m_AveragePhotonEnergy;
//Total Internal Reflection
//
// Hecht page 94
const G4double CApexCalculator::m_IndexRefractAir = 1.00029;
//
     http://www.detectors.saint-gobain.com/Media/Documents/
// S000000000000001004/
// SGC_Scintillation_Properties_Chart_52206.pdf
const G4double CApexCalculator::m_IndexRefractNaI = 1.85;
// Hecht page 121
const G4double CApexCalculator::m_CriticalAngle =
               asin(m_IndexRefractAir/m_IndexRefractNaI);
// 05115 Analysis logbook page 43
const G4double CApexCalculator::m_ProportionTransmitted =
               ( 1 - sin(m_CriticalAngle) );
// Cumulative effects at the scintillation point
// Nph(to be attentuated) = Edep*fScintPointEffects
//
// Division by two is to account for the fact that on average
// half of the photons go to one PMT and half to the other.
```

```
//
const G4double CApexCalculator::m_ScintPointEffects =
              m_ScintEffects*m_ProportionTransmitted/2.0;
/*
     Photon transmission from crystal to PMT
                                                 */
     Ratio of PMT active area to crystal end area.
/*
 * Kaloskamis pg 449 gives 0.27
 * Apmt/Acrystal = pi*(3.6/2)^2 / ((5.5+7.0)/2*6.0) = 0.2714
 */
const G4double CApexCalculator::m_WindowSizeFactor = 0.27;
// Efficiency of transmission from crystal to window. Knoll page 330.
const G4double CApexCalculator::m_WindowLossFactor = 0.75;
// Combined Effects
   Nearly equal to fWindowSizeFactor*fWindowLossFactor, but here
// using Przemek's value from Guide 7.
const G4double CApexCalculator::m_WindowTransmission = 0.27;
// quantum efficiency of PMT
//Knoll page 330, R2490-05 data sheet on page 30 of analysis logbook
const G4double CApexCalculator::m_PMTquantEff
const G4double CApexCalculator::m_StaticsScaleFactor = 0.88;
//Number used at runtime
const G4double CApexCalculator::m_WindowPMTeffects
        m_WindowTransmission*m_PMTquantEff*m_StaticsScaleFactor;
```

```
/*
      Interaction radius for Doppler correction.
* The interaction depth was selected by testing for the ideal
* value according to the simulation. The radius comes from
 * Kaloskamis.
*/
const G4double CApexCalculator::m_ApexRadius
                                                    = 42.8*cm/2;
const G4double CApexCalculator::m_InteractionDepth
                                                    = 2.0*cm;
const G4double CApexCalculator::m_InteractionRadius =
              m_ApexRadius + m_InteractionDepth;
CApexCalculator::CApexCalculator() {
  srand((unsigned)time(0));
  m_pApexInit = CApexInitialization::Instance();
  CollectConfigInfo();
}
void
CApexCalculator::AddHit(G4double energy, G4ThreeVector pos) {
  m_Energy = energy;
  m_RawSumEnergy += energy;
  /*
   * A trapezoid is defined with inconvenient coordinates.
   * I adjust coordinate system here so that z is the world z
```

```
* (i.e. along the length of the bar), x is toward the smaller
  * parallel face, and y is a measure of closeness to the slanted
  * face. I assume a right-handed system to determine the
  * orientation of y. The origin remains at the center of the bar.
  */
 m_InternalPosition = G4ThreeVector(pos.z(),pos.x(),pos.y());
  if (m_NumHits==0)
   m_FirstHitPosition = m_InternalPosition;
 m_NumHits++;
 TransportHitToPMT();
 return;
// Changes to this function may affect the energy calibration.
void CApexCalculator::TransportHitToPMT() {
  // Convert energy to photons (see Knoll, page 233)
  G4double photons = m_Energy * m_ScintPointEffects;
  // Attenuate photons as they travel towards the PMT's
  //photons at PMT = photons*exp[-mu*(DetLength/2 - hitPos)
  // To be correct, the Up has + and Dn has -; the original is
  //the opposite
```

}

```
m_PhotonsUp +=
   photons*exp( -1*m_pApexInit->Mu()*
 (m_pApexInit->HalfLengthOfCrystal()+
 m_InternalPosition.getZ())
);
 m_PhotonsDn +=
   photons*exp( -1*m_pApexInit->Mu()*
 (m_pApexInit->HalfLengthOfCrystal()-
 m_InternalPosition.getZ())
);
 m_Energy = sqrt(-1.0);
 m_InternalPosition = G4ThreeVector();
 return;
}
// To be called after all hits have been transported to the PMT
DetectorOutput_t* CApexCalculator::Calculate() {
 CalculatePMT();
 Reconstruct();
  DopplerCorrect();
  m_Output.NumHits
                     = m_NumHits;
 m_Output.FirstHitPos = m_FirstHitPosition;
  m_Output.EnergyDep = m_RawSumEnergy;
```

```
m_Output.EnergyUp = m_AmplitudeUp;
 m_Output.EnergyDn = m_AmplitudeDn;
 m_Output.EnergyRec
                       = m_ReconEnergy;
 m_Output.EnergyRecDop = m_GammaVector.getT();
 m_Output.PositionRec = m_ReconPosition;
 return &m_Output;
}
/*
      Reduces photon number by window and PMT effects to find
 * the minimum number of photons (first stage of PMT). Smears
 * minimum photon number into Poisson distribution to find
   m_Amplitude{Up,Dn}.
      Changes to this function may affect the energy calibration.
 */
void CApexCalculator::CalculatePMT() {
  // calculate number of photoelectrons produced in PMT's
  G4double photoElectronsUp = m_WindowPMTeffects*m_PhotonsUp;
  G4double photoElectronsDn = m_WindowPMTeffects*m_PhotonsDn;
  // Smear into Poisson distributions
  photoElectronsUp =
    CLHEP::RandPoisson::shoot((double)photoElectronsUp);
  photoElectronsDn =
```

```
CLHEP::RandPoisson::shoot((double)photoElectronsDn);
 // Poisson returns an int. Smear int througout the range of
 // the bin to avoid funny binning properties, e.g., at Up=2*Dn.
 m_AmplitudeUp =
   photoElectronsUp +
    ( (G4double)rand()/((G4double)RAND_MAX + (G4double)1.0) );
 m_AmplitudeDn =
   photoElectronsDn +
    ( (G4double)rand()/((G4double)RAND_MAX + (G4double)1.0) );
 return;
}
// Uses m_Amplitude{Up,Dn} to determine the unscaled reconstructed
//energy and position of the event in this bar.
void CApexCalculator::Reconstruct() {
  if ( (m_AmplitudeDn<=0.0) || (m_AmplitudeUp<=0.0) ) {</pre>
    m_{ReconPosition} = -30.0*cm;
    m_ReconEnergy = 1.0*keV;
  } else {
    m_ReconPosition = (1/(2*m_pApexInit->Mu()))
                      * log(m_AmplitudeDn/m_AmplitudeUp);
    m_ReconEnergy = m_pApexInit->Alpha()
```

```
* sqrt(m_AmplitudeUp*m_AmplitudeDn);
  }:
  return;
}
/*
      Doppler shift reconstructed energy from lab frame to particle
  frame using the midtarget beta and the reconstructed position.
    A massless Lorentz vector for the gamma ray is constructed
   then boosted to the lab frame.
      Since x and y are not changed in a boost, they are given
  incorrect fixed values that don't matter. The important point
 * is that r^2 = sqrt(x^2 + y^2) is the interaction radius so
 * that unit() returns a unit vector with the the correct theta
 * of the reconstructed gamma emission direction.
 */
void CApexCalculator::DopplerCorrect() {
  G4ThreeVector gammaDirection =
    G4ThreeVector(m_InteractionRadius, 0.0,
  m_ReconPosition - m_pApexInit->DoppReconZPos());
  gammaDirection = gammaDirection.unit();
  m_GammaVector =
```

```
G4LorentzVector(m_ReconEnergy*gammaDirection, m_ReconEnergy);
m_GammaVector.boostZ(-1*m_pApexInit->BetaPosttarget());
return;
}
```

## BIBLIOGRAPHY

- [1] M. Honma, T. Otsuka, B. A. Brown, and T. Mizusaki. Effective interaction for pf-shell nuclei. Phys. Rev. C, 65(6):061301, May 2002.
- [2] S. N. Liddick, P. F. Mantica, R. V. F. Janssens, R. Broda, B. A. Brown, M. P. Carpenter, B. Fornal, M. Honma, T. Mizusaki, A. C. Morton, W. F. Mueller, T. Otsuka, J. Pavan, A. Stolz, S. L. Tabor, B. E. Tomlin, and M. Wiedeking. Lowest excitations in <sup>56</sup>Ti and the predicted N = 34 shell closure. *Phys. Rev. Lett.*, 92(7):072502, Feb 2004.
- [3] S. N. Liddick, P. F. Mantica, R. Broda, B. A. Brown, M. P. Carpenter, A. D. Davies, B. Fornal, T. Glasmacher, D. E. Groh, M. Honma, M. Horoi, R. V. F. Janssens, T. Mizusaki, D. J. Morrissey, A. C. Morton, W. F. Mueller, T. Otsuka, J. Pavan, H. Schatz, A. Stolz, S. L. Tabor, B. E. Tomlin, and M. Wiedeking. Development of shell closures at N = 32, 34. I. β decay of neutron-rich Sc isotopes. Phys. Rev. C, 70(6):064303, Dec 2004.
- [4] R. V. F. Janssens, B. Fornal, P. F. Mantica, B. A. Brown, R. Broda, P. Bhattacharyya, M. P. Carpenter, M. Cinausero, P. J. Daly, A. D. Davies, T. Glasmacher, Z. W. Grabowski, D. E. Groh, M. Honma, F. G. Kondev, W. Królas, T. Lauritsen, S. N. Liddick, S. Lunardi, N. Marginean, T. Mizusaki, D. J. Morrissey, A. C. Morton, W. F. Mueller, T. Otsuka, T. Pawlat, D. Seweryniak, H. Schatz, A. Stolz, S. L. Tabor, C. A. Ur, G. Viesti, I. Wiedenhoever, and J. Wrzesiński. Structure of <sup>52,54</sup>Ti and shell closures in neutron-rich nuclei above <sup>48</sup>Ca. Physics Letters B, 546(1-2):55 62, 2002.
- [5] B. Fornal, S. Zhu, R. V. F. Janssens, M. Honma, R. Broda, P. F. Mantica, B. A. Brown, M. P. Carpenter, P. J. Daly, S. J. Freeman, Z. W. Grabowski, N. J. Hammond, F. G. Kondev, W. Królas, T. Lauritsen, S. N. Liddick, C. J. Lister, E. F. Moore, T. Otsuka, T. Pawłat, D. Seweryniak, B. E. Tomlin, and J. Wrzesiński. Development of shell closures at N = 32, 34. II. lowest yrast excitations in even-even Ti isotopes from deep-inelastic heavy-ion collisions. Phys. Rev. C, 70(6):064304, Dec 2004.
- [6] M. Honma, T. Otsuka, B. A. Brown, and T. Mizusaki. Shell-model description of neutron-rich pf-shell nuclei with a new effective interaction GXPF1. Eur. Phys. J. A, 25(s01):499, October 2005.

- [7] A. Gade, R. V. F. Janssens, D. Bazin, R. Broda, B. A. Brown, C. M. Campbell, M. P. Carpenter, J. M. Cook, A. N. Deacon, D.-C. Dinca, B. Fornal, S. J. Freeman, T. Glasmacher, P. G. Hansen, B. P. Kay, P. F. Mantica, W. F. Mueller, J. R. Terry, J. A. Tostevin, and S. Zhu. Cross-shell excitation in two-proton knockout: Structure of <sup>52</sup>Ca. Physical Review C (Nuclear Physics), 74(2):021302, 2006.
- [8] J. Chadwick. The Existence of a Neutron. Proceedings of the Royal Society of London. Series A, Containing Papers of a Mathematical and Physical Character, 136(830):692-708, 1932.
- [9] M. Goeppert-Mayer and J. H. D. Jensen. Elementary theory of nuclear shell structure. Wiley, New York, 1955.
- [10] J. J. Sakurai. Spin-orbit force and a neutral vector meson. *Phys. Rev.*, 119(5):1784–1785, Sep 1960.
- [11] S. Cohen and D. Kurath. Effective interactions for the 1p shell. Nuclear Physics, 73(1):1 24, 1965.
- [12] B A Brown and B H Wildenthal. Status of the nuclear shell model. Annual Review of Nuclear and Particle Science, 38(1):29-66, 1988.
- [13] D. H. Wilkinson. Comments on Nucl. and Part. Phys., 1:139, 1967.
- [14] Petr Navrátil, Michael Thoresen, and Bruce R. Barrett. Microscopic origins of effective charges in the shell model. *Phys. Rev. C*, 55(2):R573–R576, Feb 1997.
- [15] B. A. Brown, A. Arima, and J. B. McGrory. E2 core-polarization charge for nuclei near <sup>16</sup>O and <sup>40</sup>Ca. Nuclear Physics A, 277(1):77 – 108, 1977.
- [16] H. Sagawa and B. A. Brown. E2 core polarization for sd-shell single-particle states calculated with a skyrme-type interaction. Nuclear Physics A, 430(1):84 – 98, 1984.
- [17] C.M. Campbell, N. Aoi, D. Bazin, M.D. Bowen, B.A. Brown, J.M. Cook, D.-C. Dinca, A. Gade, T. Glasmacher, M. Horoi, S. Kanno, T. Motobayashi, L.A. Riley, H. Sagawa, H. Sakurai, K. Starosta, H. Suzuki, S. Takeuchi, J.R. Terry, K. Yoneda, and H. Zwahlen. Quadrupole collectivity in silicon isotopes approaching neutron number N = 28. Physics Letters B, 652(4):169 173, 2007.
- [18] Takaharu Otsuka, Rintaro Fujimoto, Yutaka Utsuno, B. Alex Brown, Michio Honma, and Takahiro Mizusaki. Magic numbers in exotic nuclei and spinisospin properties of the *nn* interaction. *Phys. Rev. Lett.*, 87(8):082502, Aug 2001.

- [19] T. T. S. Kuo and G. E. Brown. Reaction matrix elements for the 0f-1p shell nuclei. Nuclear Physics A, 114(2):241 279, 1968.
- [20] D.-C. Dinca, R. V. F. Janssens, A. Gade, D. Bazin, R. Broda, B. A. Brown, C. M. Campbell, M. P. Carpenter, P. Chowdhury, J. M. Cook, A. N. Deacon, B. Fornal, S. J. Freeman, T. Glasmacher, M. Honma, F. G. Kondev, J.-L. Lecouey, S. N. Liddick, P. F. Mantica, W. F. Mueller, H. Olliver, T. Otsuka, J. R. Terry, B. A. Tomlin, and K. Yoneda. Reduced transition probabilities to the first 2<sup>+</sup> state in <sup>52,54,56</sup>Ti and development of shell closures at N = 32, 34. Physical Review C (Nuclear Physics), 71(4):041302, 2005.
- [21] R. du Rietz, J. Ekman, D. Rudolph, C. Fahlander, A. Dewald, O. Möller, B. Saha, M. Axiotis, M. A. Bentley, C. Chandler, G. de Angelis, F. Della Vedova, A. Gadea, G. Hammond, S. M. Lenzi, N. Mărginean, D. R. Napoli, M. Nespolo, C. Rusu, and D. Tonev. Effective charges in the fp shell. Phys. Rev. Lett., 93(22):222501, Nov 2004.
- [22] National Nuclear Data Center, Nuclear Science References, version of 1995. Information extracted from the NSR database AR\_220768\_1.ens.
- [23] Table of Isotopes. Wiley-Interscience, 8th edition, 1996.
- [24] B. A. Brown. Private communication.
- [25] J. M. Cook, T. Glasmacher, and A. Gade. Accuracy of  $B(E2; 0_1^+ \rightarrow 2_1^+)$  transition rates from intermediate-energy Coulomb excitation experiments. *Physical Review C (Nuclear Physics)*, 73(2):024315, 2006.
- [26] S. A. Moszkowski. Beta- and gamma-ray spectroscopy, chapter 13, page 373.
  North-Holland Pub. Co., Amsterdam, 1955.
- [27] D. B. Fossan and E. K. Warburton. Nuclear Spectroscopy and Reactions. Academic Press, New York and London, 1974.
- [28] H. Morinaga and T. Yamazaki. *In-beam Gamma-ray Spectroscopy*. North-Holland Pub. Co., Amsterdam, 1976.
- [29] J. R. Terry, B. A. Brown, C. M. Campbell, J. M. Cook, A. D. Davies, D.-C. Dinca, A. Gade, T. Glasmacher, P. G. Hansen, B. M. Sherrill, H. Zwahlen, D. Bazin, K. Yoneda, J. A. Tostevin, T. Otsuka, Y. Utsuno, and B. Pritychenko. Single-neutron knockout from intermediate energy beams of <sup>30,32</sup>Mg: Mapping the transition into the "island of inversion". *Physical Review C (Nuclear Physics)*, 77(1):014316, 2008.
- [30] A. Chester, P. Adrich, A. Becerril, D. Bazin, C.M. Campbell, J.M. Cook, D.-C. Dinca, W.F. Mueller, D. Miller, V. Moeller, R.P. Norris, M. Portillo, K. Starosta, A. Stolz, J.R. Terry, H. Zwahlen, C. Vaman, and A. Dewald.

- Application of the time-of-flight technique for lifetime measurements with relativistic beams of heavy nuclei. Nuclear Instruments and Methods in Physics Research Section A: Accelerators, Spectrometers, Detectors and Associated Equipment, 562(1):230 240, 2006.
- [31] U. Kneissl, H. H. Pitz, and A. Zilges. Investigation of nuclear structure by resonance fluorescence scattering. *Progress in Particle and Nuclear Physics*, 37:349 433, 1996.
- [32] D. G. Ravenhall. Electron scattering and nuclear charge distributions. *Rev. Mod. Phys.*, 30(2):430–438, Apr 1958.
- [33] K. Alder and A. Winther. Electromagnetic excitation: theory of Coulomb excitation with heavy ions. North-Holland Pub. Co., New York, 1975.
- [34] Aage Winther and Kurt Alder. Relativistic Coulomb excitation. *Nuclear Physics A*, 319(3):518 532, 1979.
- [35] T. Motobayashi, Y. Ikeda, K. Ieki, M. Inoue, N. Iwasa, T. Kikuchi, M. Kurokawa, S. Moriya, S. Ogawa, H. Murakami, S. Shimoura, Y. Yanagisawa, T. Nakamura, Y. Watanabe, M. Ishihara, T. Teranishi, H. Okuno, and R. F. Casten. Large deformation of the very neutron-rich nucleus <sup>32</sup>Mg from intermediate-energy Coulomb excitation. *Physics Letters B*, 346(1-2):9 14, 1995.
- [36] T. Glasmacher. Coulomb excitation at intermediate energies. *Annual Review of Nuclear and Particle Science*, 48(1):1–31, 1998.
- [37] W. W. Wilcke, J. R. Birkelund, H. J. Wollersheim, A. D. Hoover, J. R. Huizenga, W. U. Schröder, and L. E. Tubbs. Reaction parameters for heavy-ion collisions. *Atomic Data and Nuclear Data Tables*, 25(5-6):389 619, 1980.
- [38] A. Gade, D. Bazin, C. M. Campbell, J. A. Church, D. C. Dinca, J. Enders, T. Glasmacher, Z. Hu, K. W. Kemper, W. F. Mueller, H. Olliver, B. C. Perry, L. A. Riley, B. T. Roeder, B. M. Sherrill, and J. R. Terry. Detailed experimental study on intermediate-energy Coulomb excitation of <sup>46</sup>Ar. Phys. Rev. C, 68(1):014302, Jul 2003.
- [39] J. A. Church, C. M. Campbell, D.-C. Dinca, J. Enders, A. Gade, T. Glasmacher, Z. Hu, R. V. F. Janssens, W. F. Mueller, H. Olliver, B. C. Perry, L. A. Riley, and K. L. Yurkewicz. Measurement of E2 transition strengths in <sup>32,34</sup>Mg. Physical Review C (Nuclear Physics), 72(5):054320, 2005.
- [40] W. F. Mueller, J. A. Church, T. Glasmacher, D. Gutknecht, G. Hackman, P. G. Hansen, Z. Hu, K. L. Miller, and P. Quirin. Thirty-two-fold segmented germanium detectors to identify γ-rays from intermediate-energy exotic beams. Nuclear Instruments and Methods in Physics Research Section A:

- Accelerators, Spectrometers, Detectors and Associated Equipment, 466(3):492 498, 2001.
- [41] B. C. Perry, C. M. Campbell, J. A. Church, D.-C. Dinca, J. Enders, T. Glasmacher, Z. Hu, K. L. Miller, W. F. Mueller, and H. Olliver. A high-efficiency NaI(Tl) detector array with position sensitivity for experiments with fast exotic beams. Nuclear Instruments and Methods in Physics Research Section A: Accelerators, Spectrometers, Detectors and Associated Equipment, 505(1-2):85-88, 2003. Proceedings of the tenth Symposium on Radiation Measurements and Applications.
- [42] D. Bazin, J. A. Caggiano, B. M. Sherrill, J. Yurkon, and A. Zeller. The S800 spectrograph. Nuclear Instruments and Methods in Physics Research Section B: Beam Interactions with Materials and Atoms, 204:629 633, 2003. 14th International Conference on Electromagnetic Isotope Separators and Techniques Related to their Applications.
- [43] O. Sorlin, S. Leenhardt, C. Donzaud, J. Duprat, F. Azaiez, F. Nowacki, H. Grawe, Zs. Dombrádi, F. Amorini, A. Astier, D. Baiborodin, M. Belleguic, C. Borcea, C. Bourgeois, D. M. Cullen, Z. Dlouhy, E. Dragulescu, M. Górska, S. Grévy, D. Guillemaud-Mueller, G. Hagemann, B. Herskind, J. Kiener, R. Lemmon, M. Lewitowicz, S. M. Lukyanov, and P. Mayet. <sup>68</sup><sub>28</sub>Ni<sub>40</sub>: Magicity versus superfluidity. *Phys. Rev. Lett.*, 88(9):092501, Feb 2002.
- [44] A. Bürger, T. Saito, A. Al-Khatib, A. Banu, T. Beck, F. Becker, P. Bednarczyk, G. Benzoni, A. Bracco, P. Bringel, F. Camera, E. Clement, P. Doornenbal, H. Geissel, J. Gerl, M. Górskaand A. Görgend, H. Grawe, J. Grębosz, G. Hammond, M. Hellström, H. Hübel, M. Kavatsyuk, O. Kavatsyuk, M. Kmiecik, I. Kojouharov, N. Kurz, R. Lozeva, A. Maj, S. Mandal, W. Męczyński, D. Mehta, B. Million, S. Muralithar, A. Neusser, Zs. Podolyák, T.S. Reddy, P. Reiter, N. Saito, H. Schaffner, A.K. Singh, H. Weick, O. Wieland, C. Wheldon, M. Winkler, and H.J. Wollersheim. Relativistic Coulomb excitation of 54,56,58 Cr. Acta Phys. Pol. B, 36:1249, 2005.
- [45] Heather Olliver, Thomas Glasmacher, and Andrew E. Stuchbery. Angular distributions of  $\gamma$ -rays with intermediate-energy beams. *Phys. Rev. C*, 68(4):044312, Oct 2003.
- [46] H. Scheit, O. Niedermaier, V. Bildstein, H. Boie, J. Fitting, R. von Hahn, F. Köck, M. Lauer, U. K. Pal, H. Podlech, R. Repnow, D. Schwalm, C. Alvarez, F. Ames, G. Bollen, S. Emhofer, D. Habs, O. Kester, R. Lutter, K. Rudolph, M. Pasini, P. G. Thirolf, B. H. Wolf, J. Eberth, G. Gersch, H. Hess, P. Reiter, O. Thelen, N. Warr, D. Weisshaar, F. Aksouh, P. Van den Bergh, P. Van Duppen, M. Huyse, O. Ivanov, P. Mayet, J. Van de Walle, J. Äystö, P. A. Butler, J. Cederkäll, P. Delahaye, H. O. U. Fynbo, L. M. Fraile,

- O. Forstner, S. Franchoo, U. Köster, T. Nilsson, M. Oinonen, T. Sieber, F. Wenander, M. Pantea, A. Richter, G. Schrieder, H. Simon, T. Behrens, R. Gernhäuser, T. Kröll, R. Krücken, M. Münch, T. Davinson, J. Gerl, G. Huber, A. Hurst, J. Iwanicki, B. Jonson, P. Lieb, L. Liljeby, A. Schempp, A. Scherillo, P. Schmidt, and G. Walter. Coulomb excitation of neutron-rich beams at REX-ISOLDE. *Eur. Phys. J. A*, 25, s01:397, 2005.
- [47] O. Niedermaier, H. Scheit, V. Bildstein, H. Boie, J. Fitting, R. von Hahn, F. Köck, M. Lauer, U. K. Pal, H. Podlech, R. Repnow, D. Schwalm, C. Alvarez, F. Ames, G. Bollen, S. Emhofer, D. Habs, O. Kester, R. Lutter, K. Rudolph, M. Pasini, P. G. Thirolf, B. H. Wolf, J. Eberth, G. Gersch, H. Hess, P. Reiter, O. Thelen, N. Warr, D. Weisshaar, F. Aksouh, P. Van den Bergh, P. Van Duppen, M. Huyse, O. Ivanov, P. Mayet, J. Van de Walle, J. Äystö, P. A. Butler, J. Cederkäll, P. Delahaye, H. O. U. Fynbo, L. M. Fraile, O. Forstner, S. Franchoo, U. Köster, T. Nilsson, M. Oinonen, T. Sieber, F. Wenander, M. Pantea, A. Richter, G. Schrieder, H. Simon, T. Behrens, R. Gernhäuser, T. Kröll, R. Krücken, M. Münch, T. Davinson, J. Gerl, G. Huber, A. Hurst, J. Iwanicki, B. Jonson, P. Lieb, L. Liljeby, A. Schempp, A. Scherillo, P. Schmidt, and G. Walter. "Safe" Coulomb excitation of 30 Mg. Physical Review Letters, 94(17):172501, 2005.
- [48] O. Niedermaier, H. Scheit, V. Bildstein, H. Boie, J. Fitting, R. von Hahn, F. Köck, M. Lauer, U.K. Pal, H. Podlech, R. Repnow, D. Schwalm, C. Alvarez, F. Ames, G. Bollen, S. Emhofer, D. Habs, O. Kester, R. Lutter, K. Rudolph, M. Pasini, P.G. Thirolf, B.H. Wolf, J. Eberth, G. Gersch, H. Hess, P. Reiter, O. Thelen, N. Warr, D. Weisshaar, F. Aksouh, P. Van den Bergh, P. Van Duppen, M. Huyse, O. Ivanov, P. Mayet, J. Van de Walle, J. Äystö, P.A. Butler, J. Cederkäll, P. Delahaye, H.O.U. Fynbo, L.M. Fraile, O. Forstner, S. Franchoo, U. Köster, T. Nilsson, M. Oinonen, T. Sieber, F. Wenander, M. Pantea, A. Richter, G. Schrieder, H. Simon, T. Behrens, R. Gernhäuser, T. Kröll, R. Krücken, M. Münch, T. Davinson, J. Gerl, G. Huber, A. Hurst, J. Iwanicki, B. Jonson, P. Lieb, L. Liljeby, A. Schempp, A. Scherillo, P. Schmidt, and G. Walter. The neutron-rich Mg isotopes: First results from MINIBALL at REX-ISOLDE. Nuclear Physics A, 752:273 278, 2005. Proceedings of the 22nd International Nuclear Physics Conference (Part 2).
- [49] J. Äystö. Concluding remarks of the ENAM'04 conference. Eur. Phys. J. A, 25, s01:767, 2005.
- [50] B. V. Pritychenko, T. Glasmacher, P. D. Cottle, M. Fauerbach, R. W. Ibbotson, K. W. Kemper, V. Maddalena, A. Navin, R. Ronningen, A. Sakharuk, H. Scheit, and V. G. Zelevinsky. Role of intruder configurations in <sup>26,28</sup>Ne and <sup>30,32</sup>Mg. *Physics Letters B*, 461(4):322 328, 1999.
- [51] V. Chisté, A. Gillibert, A. Lépine-Szily, N. Alamanos, F. Auger, J. Barrette, F. Braga, M. D. Cortina-Gil, Z. Dlouhy, V. Lapoux, M. Lewitowicz, R. Licht-

- enthäler, R. Liguori Neto, S. M. Lukyanov, M. MacCormick, F. Marie, W. Mittig, F. de Oliveira Santos, N. A. Orr, A. N. Ostrowski, S. Ottini, A. Pakou, Yu. E. Penionzhkevich, P. Roussel-Chomaz, and J. L. Sida. Electric and nuclear transition strength in <sup>30,32</sup>Mg. *Physics Letters B*, 514(3-4):233 239, 2001.
- [52] S. Raman, C. W. Nestor, and P. Tikkanen. Transition probability from the ground to the first-excited 2<sup>+</sup> state of even-even nuclides. *Atomic Data and Nuclear Data Tables*, 78(1):1 128, 2001.
- [53] R. Pfaff, D. J. Morrissey, W. Benenson, M. Fauerbach, M. Hellström, C. F. Powell, B. M. Sherrill, M. Steiner, and J. A. Winger. Fragmentation of <sup>78</sup>Kr projectiles. *Phys. Rev. C*, 53(4):1753–1758, Apr 1996.
- [54] D. J. Morrissey, B. M. Sherrill, M. Steiner, A. Stolz, and I. Wiedenhoever. Commissioning the A1900 projectile fragment separator. *NIMB*, 204:90–96, 2003.
- [55] I. Ahmad, S. M. Austin, B. B. Back, R. R. Betts, F. P. Calaprice, K. C. Chan, A. Chishti, P. Chowdhury, C. Conner, R. W. Dunford, J. D. Fox, S. J. Freedman, M. Freer, S. B. Gazes, A. L. Hallin, T. Happ, D. Henderson, N. I. Kaloskamis, E. Kashy, W. Kutschera, J. Last, C. J. Lister, M. Liu, M. R. Maier, D. J. Mercer, D. Mikolas, and P. A. A. Perera. Search for narrow sum-energy lines in electron-positron pair emission from heavy-ion collisions near the Coulomb barrier. *Phys. Rev. Lett.*, 75(14):2658-2661, Oct 1995.
- [56] N.I. Kaloskamis, K.C. Chan, A.A. Chishti, J.S. Greenberg, C.J. Lister, S.J. Freedman, M. Wolanski, J. Last, and B. Utts. The trigger detector for APEX: An array of position-sensitive NaI(Tl) detectors for the imaging of positrons from heavy-ion collisions. Nuclear Instruments and Methods in Physics Research Section A: Accelerators, Spectrometers, Detectors and Associated Equipment, 330(3):447 457, 1993.
- [57] J. A. Church. Collectivity in light neutron-rich nuclei near N=20: Intermediate-energy Coulomb excitation of  $^{32,34}Mg$ ,  $^{35,36}Al$ , and  $^{37}Si$ . PhD thesis, Michigan State University, 2003.
- [58] S. Agostinelli, J. Allison, K. Amako, J. Apostolakis, H. Araujo, P. Arce, M. Asai, D. Axen, S. Banerjee, G. Barrand, F. Behner, L. Bellagamba, J. Boudreau, L. Broglia, A. Brunengo, H. Burkhardt, S. Chauvie, J. Chuma, R. Chytracek, G. Cooperman, G. Cosmo, P. Degtyarenko, A. Dell'Acqua, G. Depaola, D. Dietrich, R. Enami, A. Feliciello, C. Ferguson, H. Fesefeldt, G. Folger, F. Foppiano, A. Forti, S. Garelli, S. Giani, R. Giannitrapani, D. Gibin, J. J. Gómez Cadenas, I. González, G. Gracia Abril, G. Greeniaus, W. Greiner, V. Grichine, A. Grossheim, S. Guatelli, P. Gumplinger, R. Hamatsu, K. Hashimoto, H. Hasui, A. Heikkinen,

- A. Howard, V. Ivanchenko, A. Johnson, F. W. Jones, J. Kallenbach, N. Kanaya, M. Kawabata, Y. Kawabata, M. Kawaguti, S. Kelner, P. Kent, A. Kimura, T. Kodama, R. Kokoulin, M. Kossov, H. Kurashige, E. Lamanna, T. Lampén, V. Lara, V. Lefebure, F. Lei, M. Liendl, W. Lockman, F. Longo, S. Magni, M. Maire, E. Medernach, K. Minamimoto, P. Mora de Freitas, Y. Morita, K. Murakami, M. Nagamatu, R. Nartallo, P. Nieminen, T. Nishimura, K. Ohtsubo, M. Okamura, S. O'Neale, Y. Oohata, K. Paech, J. Perl, A. Pfeiffer, M. G. Pia, F. Ranjard, A. Rybin, S. Sadilov, E. Di Salvo, G. Santin, T. Sasaki, N. Savvas, Y. Sawada, S. Scherer, S. Sei, V. Sirotenko, D. Smith, N. Starkov, H. Stoecker, J. Sulkimo, M. Takahata, S. Tanaka, E. Tcherniaev, E. Safai Tehrani, M. Tropeano, P. Truscott, H. Uno, L. Urban, P. Urban, M. Verderi, A. Walkden, W. Wander, H. Weber, J. P. Wellisch, T. Wenaus, D. C. Williams, D. Wright, T. Yamada, H. Yoshida, and D. Zschiesche. GEANT4-a simulation toolkit. Nuclear Instruments and Methods in Physics Research Section A: Accelerators, Spectrometers, Detectors and Associated Equipment, 506(3):250 - 303, 2003.
- [59] J. Allison, K. Amako, J. Apostolakis, H. Araujo, P. Arce Dubois, M. Asai, G. Barrand, R. Capra, S. Chauvie, R. Chytracek, G.A.P. Cirrone, G. Cooperman, G. Cosmo, G. Cuttone, G.G. Daquino, M. Donszelmann, M. Dressel, G. Folger, F. Foppiano, J. Generowicz, V. Grichine, S. Guatelli, P. Gumplinger, A. Heikkinen, I. Hrivnacova, A. Howard, S. Incerti, V. Ivanchenko, T. Johnson, F. Jones, T. Koi, R. Kokoulin, M. Kossov, H. Kurashige, V. Lara, S. Larsson, F. Lei, O. Link, F. Longo, M. Maire, A. Mantero, B. Mascialino, I. McLaren, P. Mendez Lorenzo, K. Minamimoto, K. Murakami, P. Nieminen, L. Pandola, S. Parlati, L. Peralta, J. Perl, A. Pfeiffer, M.G. Pia, A. Ribon, P. Rodrigues, G. Russo, S. Sadilov, G. Santin, T. Sasaki, D. Smith, N. Starkov, S. Tanaka, E. Tcherniaev, B. Tome, A. Trindade, P. Truscott, L. Urban, M. Verderi, A. Walkden, J.P. Wellisch, D.C. Williams, D. Wright, and H. Yoshida. GEANT4 developments and applications. Nuclear Science, IEEE Transactions on, 53(1):270-278, Feb. 2006.
- [60] G. F. Knoll. Radiation Detection and Measurement. John Wiley & Sons, Inc., Hoboken, NJ, 2000.
- [61] D. Bazin, O. Tarasov, M. Lewitowicz, and O. Sorlin. The program LISE: a simulation of fragment separators. Nuclear Instruments and Methods in Physics Research Section A: Accelerators, Spectrometers, Detectors and Associated Equipment, 482(1-2):307 327, 2002.
- [62] B. A. Brown, D. B. Fossan, J. M. McDonald, and K. A. Snover. Lifetime measurements and E2 effective charges for nuclei in the  $1f_{7/2}$  shell. *Phys. Rev. C*, 9(3):1033–1053, Mar 1974.
- [63] M. Rejmund, S. Bhattacharyya, A. Navin, W. Mittig, L. Gaudefroy, M. Gelin, G. Mukherjee, F. Rejmund, P. Roussel-Chomaz, and Ch. Theisen. Shell evo-

- lution and the N=34 "magic number". Physical Review C (Nuclear Physics), 76(2):021304, 2007.
- [64] T. Glasmacher. Intermediate-energy Coulomb excitation. *Nuclear Physics A*, 693(1-2):90 104, 2001.
- [65] F. Perrot, F. Maréchal, C. Jollet, Ph. Dessagne, J.-C. Angélique, G. Ban, P. Baumann, F. Benrachi, U. Bergmann, C. Borcea, A. Buţă, J. Cederkall, S. Courtin, J.-M. Daugas, L. M. Fraile, S. Grévy, A. Jokinen, F. R. Lecolley, E. Liénard, G. Le Scornet, V. Méot, Ch. Miehé, F. Negoiţă, N. A. Orr, S. Pietri, E. Poirier, M. Ramdhane, O. Roig, I. Stefan, and W. Wang. β-decay studies of neutron-rich K isotopes. Physical Review C (Nuclear Physics), 74(1):014313, 2006.
- [66] K. L. Yurkewicz, D. Bazin, B. A. Brown, C. M. Campbell, J. A. Church, D.-C. Dinca, A. Gade, T. Glasmacher, M. Honma, T. Mizusaki, W. F. Mueller, H. Olliver, T. Otsuka, L. A. Riley, and J. R. Terry. E2 excitation strength in <sup>55</sup>Ni: coupling of the <sup>56</sup>Ni 2<sub>1</sub><sup>+</sup> collective core vibration to the f<sub>7/2</sub> odd neutron hole. Phys. Rev. C, 70(6):064321, Dec 2004.

